

Axisymmetric flows on the torus geometry

Sergiu Busuioc¹, and H. Kusumaatmaja^{2,†} and Victor E. Ambrus^{3,4,‡}

¹School of Engineering, University of Edinburgh, Edinburgh, EH9 3FB, UK

²Department of Physics, Durham University, Durham, DH1 3LE, UK

³Department of Physics, West University of Timișoara, Timișoara, 300223, Romania

⁴Department of Mathematics and Statistics, Old Dominion University, Norfolk, VA 23529, USA

(Received xx; revised xx; accepted xx)

We present a series of analytically solvable axisymmetric flows on the torus geometry. For the single-component flows, we describe the propagation of sound waves for perfect fluids, as well as the viscous damping of shear and longitudinal waves for isothermal and thermal fluids. Unlike the case of planar geometry, the non-uniform curvature on a torus necessitates a distinct spectrum of eigenfrequencies and their corresponding basis functions. This has several interesting consequences, including breaking the degeneracy between even and odd modes, a lack of periodicity even in the flows of perfect fluids and the loss of Galilean invariance for flows with velocity components in the poloidal direction. For the multi-component flows, we study the equilibrium configurations and relaxation dynamics of axisymmetric fluid stripes, described using the Cahn-Hilliard equation. We find a second-order phase transition in the equilibrium location of the stripe as a function of its area ΔA . This phase transition leads to a complex dependence of the Laplace pressure on ΔA . We also derive the underdamped oscillatory dynamics as the stripes approach equilibrium. Furthermore, relaxing the assumption of axial symmetry, we derive the conditions under which the stripes become unstable. In all cases, the analytical results are confirmed numerically using a finite-difference Navier-Stokes solver.

1. Introduction

In recent years there has been a growing interest in studying and understanding hydrodynamic flows on curved surfaces, supported by increasing evidence for their relevance in a wide range of problems in nature and engineering. Examples include phenomena in materials science, such as the motion of electrons in graphene (Giordanelli *et al.* 2018), interface rheology in foams (Cox *et al.* 2004) and the dynamics of confined active matter (Keber *et al.* 2014; Henkes *et al.* 2018; Janssen *et al.* 2017; Pearce *et al.* 2019); in biophysics, such as flows on curved biomembranes (Henle & Levine 2010; Arroyo & Desimone 2009; Al-Izzi *et al.* 2018; Fonda *et al.* 2018) or fluid deformable surfaces (Torres-Sánchez *et al.* 2019; Voigt 2019); in fusion technology, such as plasma motion under toroidal confinement (Boozer 2005); and in geophysics, such as zonal flows on planets and the Sun (Sasaki *et al.* 2015).

In this work, we consider a series of axisymmetric flows on the torus geometry (i.e. flows which are homogeneous with respect to the azimuthal torus coordinate) for which analytic solutions can be derived. The torus is chosen as it represents one of the simplest geometries with non-uniform curvature. On the one hand, these flows allow us to identify

† Email address for correspondence: halim.kusumaatmaja@durham.ac.uk

‡ Email address for correspondence: victor.ambrus@e-uvt.ro

novel flow phenomena arising from the presence of non-uniform curvature, which are absent on planar geometries. Importantly, our analytical calculations allow us to identify the key ingredients for observing these phenomena. On the other hand, this work can provide several non-trivial benchmark problems suitable for developing computational methods for flows on curved surfaces. To date, a number of numerical approaches have been developed to solve the fluid equations of motion on curved manifolds, including using finite-element (Dziuk & Elliott 2007, 2013), level set (Bertalmio *et al.* 2001), phase-field (Rätz & Voigt 2006), closest point (Macdonald & Ruuth 2010) and lattice Boltzmann (Ambrus *et al.* 2019) methods. Recently, interest has been shown also for fluid systems on evolving curved manifolds both for incompressible (Koba *et al.* 2017; Nitschke *et al.* 2019) and compressible (Koba 2018) fluids. However, despite the availability of these various methods, to date there is still a lack of systematic comparisons to assess and compare their accuracy and robustness. Here, we directly compare all the analytical derivations against numerical simulations obtained using a finite-difference Navier-Stokes solver.

In total we discuss five problems with increasing complexity. First, we start with the propagation of sound waves for a perfect fluid on a torus. Then, we consider viscous damping. We study shear wave damping, where the fluid velocity is in the azimuthal direction of the torus, as well as the damping of longitudinal waves, where the fluid velocity is in the poloidal direction. These three problems have been regularly studied for the planar geometry, and they are popular benchmark case studies for Navier-Stokes solvers (Sofonea & Sekerka 2003; Rembiaz *et al.* 2017; Sofonea *et al.* 2018; Busuioc *et al.* 2020a). Here, for their torus equivalent, we analyse the flows by deriving their distinct discrete spectrum of eigenfrequencies and corresponding basis functions. We carry out these studies for isothermal and thermal single-component fluids, as well as for multicomponent fluids described by the Cahn-Hilliard equation. Interestingly, we find that the degeneracy between odd and even modes is broken, which can be observed both in the oscillation frequencies and decay rates of those modes. Due to the non-uniform curvature, we will also show that Galilean invariance and flow periodicity, as commonly observed in the planar geometry, can be lost.

Next, we focus on an axisymmetric fluid stripe embedded on a torus. Focussing on the static configurations, the spatial symmetry is broken in the poloidal direction and we find a second-order phase transition in the location of the minimum energy configurations depending on the area of the fluid stripes. We further derive the equivalent of a Laplace pressure on a torus geometry, where additional terms are present due to the underlying curved metric. As a consequence of the phase transition, the Laplace pressure of a fluid stripe in equilibrium has a complex dependence on its area. For completeness, we also discuss other configurations, available when the axisymmetry restriction is lifted, which may have lower energy compared to the stripe configuration under certain conditions. Furthermore, we derive the regime of stability of the stripe configurations under small azimuthal perturbations. We then study the relaxation dynamics of the fluid stripes. When the Cahn-Hilliard equation is coupled with hydrodynamics, we find an underdamped oscillatory motion for the stripe dynamics. We derive the oscillation frequency and the exponential decay rate. The case in the absence of hydrodynamics, where the stripes simply relax exponentially to their equilibrium position, is discussed in Sec. SM:2.4 of the supplementary material.

The paper is structured as follows. Sec. 2 describes the hydrodynamic equations for flows on general curved surfaces, which are then specialised to the case of axisymmetric flows on the torus geometry. The five axisymmetric flow problems are introduced and presented in Secs. 3-7. Taken together, our series of axisymmetric flows cover single- and multi-component flows, static and dynamic aspects, instabilities under small per-

turbations, perfect and viscous fluids, isothermal and thermal cases and motion in the azimuthal and poloidal directions of the torus. A summary of the work and concluding remarks are finally presented in Sec. 8. The paper also includes two appendices. Appendix A presents a convergence order analysis of the solver employed in this paper with respect to the first three benchmark tests, discussed in Sections 3, 4 and 5. Appendix B discusses the perturbative procedure that we use to obtain the mode solutions necessary for the spatial part of the linearised hydrodynamic equations, which are employed in the main text.

The supplementary material (SM) (Busuioc *et al.* 2020b) contains three sections. Section SM:1 provides details on the implementation of our numerical scheme. Section SM:2 contains mathematical complements for the analysis of the Cahn-Hilliard model on the torus geometry. Finally, Section SM:3 applies the procedure described in Appendix B to derive expansions of the mode functions and related quantities up to ninth order with respect to the torus aspect ratio, $0 < a = r/R < 1$. These expansions are available for download under as gnuplot files (*funcs-inv.gpl* and *funcs-shear.gpl*) and Mathematica notebooks (*funcs_inv.nb* and *funcs_shear.nb*) in the supplementary material. In addition, two animations of the development of the instability of fluid stripes due to azimuthal perturbations, discussed in Sec. 6.2, also provided in the supplementary material.

2. Hydrodynamics on curved surfaces

Over the past decades, there have been several attempts to formulate the hydrodynamic equations on curved surfaces (Serrin 1959; Marsden & Hughes 1994; Taylor 2011). In this paper, we take the strategy of first writing the fluid equations with respect to curvilinear coordinates in covariant form. Employing the orthonormal vielbein vector field $\{\mathbf{e}_\alpha, \alpha = 1, 2, 3\}$, we then take the first two vectors, \mathbf{e}_i ($i = 1, 2$) to be tangent to the manifold and enforce that no dynamics occurs along the third vector, \mathbf{e}_3 . This approach allows the fundamental conservation equations for mass, momentum and energy for fluids on a curved surface to be written in covariant form as follows:

$$\frac{D\rho}{Dt} + \rho \nabla_i u^i = 0, \quad (2.1a)$$

$$\rho \frac{Du^i}{Dt} + \nabla_j \mathbb{T}^{ij} = \rho f^i, \quad (2.1b)$$

$$\rho \frac{De}{Dt} + \mathbb{T}^{ij} \nabla_i u_j = -\nabla_i q^i, \quad (2.1c)$$

where $1 \leq i, j \leq 2$ cover the tensor components along the directions which are tangent to the surface. In the above, ρ is the fluid mass density, $\mathbf{u} = u^i \mathbf{e}_i$ is the fluid velocity, ∇_i is the covariant derivative, $D/Dt = \partial_t + u^j \nabla_j$ is the material (convective) derivative, \mathbb{T}^{ij} is the pressure tensor, f^i is the external force per unit mass (which we neglect for the remainder of this paper), $e = c_v T$ is the internal energy per unit mass, c_v is the specific heat capacity, T is the fluid temperature and q^i is the heat flux. The set of relations (2.1a)–(2.1c) are compatible with those derived from kinetic theory in curvilinear coordinates (Busuioc & Ambruş 2019) or on curved manifolds (Ambruş *et al.* 2019). Furthermore, the computation of the divergence of the stress tensor in a covariant way ensures the compatibility with the approaches currently taken in the literature (Arroyo & Desimone 2009; Taylor 2011; Nitschke *et al.* 2017; Gross & Atzberger 2018).

The hydrodynamic equations, Eq. (2.1), are not closed unless the pressure tensor \mathbb{T}^{ij} and heat flux q^i are known. The specific models employed in this paper for these quantities are discussed below in Subsec. 2.1 and 2.2, respectively. After briefly introducing the

relevant differential operators in Subsec. 2.3, we explicitly write the equations of motion for axisymmetric flows on the torus geometry in Subsec. 2.4.

2.1. Models for the pressure tensor

We restrict our analysis to the case of Newtonian fluids, for which the pressure tensor can be decomposed as

$$\mathbf{T}^{\hat{i}\hat{j}} = P_b \delta^{\hat{i}\hat{j}} + \mathbf{P}_{\kappa}^{\hat{i}\hat{j}} - \tau^{\hat{i}\hat{j}}. \quad (2.2)$$

The dissipative part $\tau^{\hat{i}\hat{j}} = \tau_{\text{dyn}}^{\hat{i}\hat{j}} + \tau_{\text{bulk}}^{\hat{i}\hat{j}}$ of the pressure tensor for a two-dimensional Newtonian fluid reads

$$\tau_{\text{dyn}}^{\hat{i}\hat{j}} = \eta \left(\nabla^{\hat{i}} u^{\hat{j}} + \nabla^{\hat{j}} u^{\hat{i}} - \delta^{\hat{i}\hat{j}} \nabla_{\hat{k}} u^{\hat{k}} \right), \quad \tau_{\text{bulk}}^{\hat{i}\hat{j}} = \eta_v \delta^{\hat{i}\hat{j}} \nabla_{\hat{k}} u^{\hat{k}}, \quad (2.3)$$

where η and η_v are the dynamic and bulk (volumetric) viscosity coefficients, respectively. For the applications considered in this work, the dependence of the transport coefficients on the flow properties is not important. Hence, we adopt the usual model in which the kinematic viscosities ν and ν_v are constant, such that η and η_v are computed using

$$\eta = \nu \rho, \quad \eta_v = \nu_v \rho. \quad (2.4)$$

For the first two terms in Eq. (2.2), P_b is the isotropic bulk pressure and $P_{\kappa}^{\hat{i}\hat{j}}$ is responsible for the surface tension, which is relevant in the case of multicomponent systems. For ideal single-component fluids, the bulk pressure is the ideal gas pressure and the surface tension part vanishes

$$P_b = P_i = \frac{\rho k_B T}{m}, \quad \mathbf{P}_{\kappa}^{\hat{i}\hat{j}} = 0, \quad (2.5)$$

where m is the average particle mass. In this paper, we always use units such that $m = 1$.

For multicomponent flows, we consider a binary mixture of fluids \mathcal{A} and \mathcal{B} , characterised by an order parameter ϕ , such that $\phi = 1$ corresponds to a bulk \mathcal{A} fluid and $\phi = -1$ to a bulk \mathcal{B} fluid. The coexistence of these two bulk fluids can be realised by using a simple form for the Helmholtz free energy Ψ :

$$\Psi = \int_V dV (\psi_b + \psi_g), \quad (2.6)$$

where the bulk ψ_b and the gradient ψ_g free energy densities are (Briant & Yeomans 2004; Krüger *et al.* 2017):

$$\psi_b = \frac{A}{4} (1 - \phi^2)^2, \quad \psi_g = \frac{\kappa}{2} (\nabla \phi)^2. \quad (2.7)$$

Here, A and κ are free parameters, which are related to the interface width ξ and surface tension σ through

$$\xi = \sqrt{\frac{\kappa}{A}}, \quad \sigma = \sqrt{\frac{8\kappa A}{9}}. \quad (2.8)$$

For simplicity, we consider the case when A and κ have constant values throughout the fluid. The chemical potential can be derived by taking the functional derivative of the free energy with respect to the order parameter, giving

$$\mu = \frac{\delta \Psi}{\delta \phi} = \mu_b + \mu_g, \quad \mu_b = -A\phi(1 - \phi^2), \quad \mu_g = -\kappa \Delta \phi. \quad (2.9)$$

The additional contributions to the pressure tensor arising from this free energy model can be found by imposing

$$\nabla_{\hat{j}} [P_{\text{CH}} \delta^{\hat{i}\hat{j}} + \mathbf{P}_{\text{CH};\kappa}^{\hat{i}\hat{j}}] = \phi \nabla^{\hat{i}} \mu, \quad (2.10)$$

which leads to

$$P_b = P_i + P_{\text{CH}} = \frac{\rho k_B T}{m} - A \left(\frac{\phi^2}{2} - \frac{3\phi^4}{4} \right),$$

$$\mathbf{P}_{\kappa}^{\hat{i}\hat{j}} = \mathbf{P}_{\text{CH};\kappa}^{\hat{i}\hat{j}} = \kappa \nabla^{\hat{i}} \phi \nabla^{\hat{j}} \phi - \kappa \delta^{\hat{i}\hat{j}} \left[\phi \Delta \phi + \frac{1}{2} (\nabla \phi)^2 \right]. \quad (2.11)$$

For multicomponent flows, in addition to the hydrodynamic equations in Eq. (2.1), another equation of motion is needed to capture the evolution of the order parameter ϕ . Here it is governed by the Cahn-Hilliard equation

$$\frac{D\phi}{Dt} + \phi \nabla_i u^i = \nabla_i (M \nabla^i \mu), \quad (2.12)$$

where M is the mobility parameter, $D/Dt = \partial_t + u^i \nabla_i$ is the material derivative and the fluid velocity \mathbf{u} is a solution of the hydrodynamic equations Eq. (2.1). For simplicity, we assume for simplicity that M takes a constant value throughout the fluid.

2.2. Model for the heat flux

We consider fluids for which the heat flux is given via Fourier's law

$$q^i = -k \nabla^i T. \quad (2.13)$$

The heat conductivity k is related to the dynamic viscosity through the Prandtl number Pr :

$$\text{Pr} = c_p \frac{\eta}{k} = c_v \frac{\gamma \eta}{k}, \quad (2.14)$$

where c_p is the specific heat at constant pressure and γ is the adiabatic index. For definiteness, we assume that Pr is a constant number in this work.

When considering isothermal flows, the temperature is assumed to remain constant and the heat flux vanishes

$$T = T_{\text{Iso}} = \text{const}, \quad q_{\text{Iso}}^i = 0. \quad (2.15)$$

In this case, the energy equation is no longer taken into consideration.

2.3. Differential operators on the torus geometry

In this subsection we provide a brief introduction to the differential geometry approach we have used to analyse the fluid flows. For concreteness, we consider the parametrisation of a torus of outer radius R and inner radius r using the coordinates $q^i \in \{\varphi, \theta\}$ (i represents a coordinate index) as follows:

$$\begin{aligned} x &= (R + r \cos \theta) \cos \varphi, \\ y &= (R + r \cos \theta) \sin \varphi, \\ z &= r \sin \theta. \end{aligned} \quad (2.16)$$

Here, φ and θ are the azimuthal and the poloidal angles, respectively, and the system is periodic with respect to both angles with period of 2π . Figure 1 depicts the coordinates and the equidistant spatial discretisation in φ and θ .

The line element on the torus can be written with respect to θ and φ as follows:

$$ds^2 = (R + r \cos \theta)^2 d\varphi^2 + r^2 d\theta^2. \quad (2.17)$$

The metric tensor associated with the above line element has the following non-vanishing

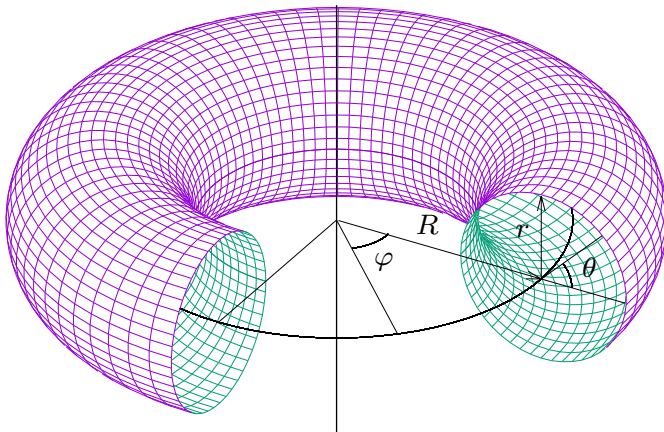


Figure 1. Spatial discretisation of the torus geometry.

components:

$$\mathbf{g}_{\varphi\varphi} = (R + r \cos \theta)^2, \quad \mathbf{g}_{\theta\theta} = r^2. \quad (2.18)$$

Similar to the approach taken by other authors (Nitschke *et al.* 2012; Reuther & Voigt 2018), it is convenient to introduce the vielbein vector frame $\{\mathbf{e}_{\hat{\varphi}}, \mathbf{e}_{\hat{\theta}}\}$, where $\mathbf{e}_i = e_i^{\hat{i}} \hat{\mathbf{d}}_i$ is the notation for a vector tangent to the surface. The components $e_i^{\hat{i}}$ satisfy

$$\mathbf{g}_{ij} e_i^{\hat{i}} e_j^{\hat{j}} = \delta_{\hat{i}\hat{j}}. \quad (2.19)$$

The natural choice for the vielbein on the torus geometry is

$$\mathbf{e}_{\hat{\varphi}} = \frac{\partial_{\varphi}}{R(1 + a \cos \theta)}, \quad \mathbf{e}_{\hat{\theta}} = \frac{\partial_{\theta}}{r}, \quad (2.20)$$

where the following notation was introduced for future convenience:

$$a = \frac{r}{R}. \quad (2.21)$$

The corresponding vielbein co-frame, comprised of the one-forms $\omega^{\hat{i}} = \omega_i^{\hat{i}} \mathbf{d}q^i$, is given by

$$\omega^{\hat{\varphi}} = R(1 + a \cos \theta) \mathbf{d}\varphi, \quad \omega^{\hat{\theta}} = r \mathbf{d}\theta, \quad (2.22)$$

such that

$$\omega_i^{\hat{i}} e_j^{\hat{i}} = \delta^{\hat{i}}_{\hat{j}}, \quad \delta_{\hat{i}\hat{j}} \omega_i^{\hat{i}} \omega_j^{\hat{j}} = g_{ij}. \quad (2.23)$$

The algebraic rules to compute the terms appearing in Eq. (2.1) are described below. The gradient $\nabla_i F = e_i^{\hat{i}} \partial_{\hat{i}} F$ of a scalar function F has the following components:

$$\nabla_{\hat{\varphi}} F = \frac{\partial_{\varphi} F}{R(1 + a \cos \theta)}, \quad \nabla_{\hat{\theta}} F = \frac{1}{r} \partial_{\theta} F. \quad (2.24)$$

For a vector field $A^{\hat{i}}$, the covariant derivative is

$$\nabla_j A^{\hat{i}} = e_j^{\hat{j}} \partial_j A^{\hat{i}} + \Gamma^{\hat{i}}_{\hat{k}j} A^{\hat{k}}, \quad (2.25)$$

and when the vector index is lowered, it becomes

$$\nabla_j A_{\hat{i}} = e_j^{\hat{j}} \partial_j A_{\hat{i}} - \Gamma^{\hat{k}}_{\hat{i}j} A_{\hat{k}}. \quad (2.26)$$

For the computation of the covariant derivatives, the connection coefficients $\Gamma^{\hat{i}}_{\hat{k}j} =$

$\delta^{\hat{i}\hat{\ell}}\Gamma_{\hat{\ell}\hat{k}\hat{j}}$ are defined as

$$\Gamma_{\hat{\ell}\hat{k}\hat{j}} = \frac{1}{2}(c_{\hat{\ell}\hat{k}\hat{j}} + c_{\hat{\ell}\hat{j}\hat{k}} - c_{\hat{k}\hat{j}\hat{\ell}}), \quad (2.27)$$

with the Cartan coefficients $c_{ij}^{\hat{k}} = \delta^{\hat{k}\hat{\ell}}c_{ij\hat{\ell}}$ to be computed from the commutator of the vectors of the vielbein field

$$[e_i, e_j] = c_{ij}^{\hat{k}} e_{\hat{k}}, \quad (2.28)$$

where the components of the commutator are $([e_i, e_j])^d = e_i^k \partial_k e_j^d - e_j^k \partial_k e_i^d$. We can also invert the above relation to get

$$c_{ij}^{\hat{k}} = \langle [e_i, e_j], \omega^{\hat{k}} \rangle = (e_i^d e_j^k - e_j^d e_i^k) \partial_k \omega_d^{\hat{k}}, \quad (2.29)$$

where $\langle \mathbf{u}, \mathbf{w} \rangle = u^i w_i$ is the inner product between a vector field $\mathbf{u} = u^i e_i$ and a one-form $\mathbf{w} = w_i \omega^i$.

Let us now apply these definitions for the case of a torus. The commutator of the vielbein vectors $e_{\hat{\theta}}$ and $e_{\hat{\varphi}}$ is

$$[e_{\hat{\theta}}, e_{\hat{\varphi}}] = -[e_{\hat{\varphi}}, e_{\hat{\theta}}] = \frac{\sin \theta}{R(1 + a \cos \theta)} e_{\hat{\varphi}}. \quad (2.30)$$

Substituting these relations into the definition of the Cartan coefficients, we find that the only non-vanishing Cartan coefficients are

$$c_{\hat{\theta}\hat{\varphi}}^{\hat{\varphi}} = -c_{\hat{\varphi}\hat{\theta}}^{\hat{\varphi}} = \frac{\sin \theta}{R(1 + a \cos \theta)}, \quad (2.31)$$

and the ensuing connection coefficients read

$$\Gamma_{\hat{\theta}\hat{\varphi}\hat{\varphi}} = -\Gamma_{\hat{\varphi}\hat{\theta}\hat{\varphi}} = \frac{\sin \theta}{R(1 + a \cos \theta)}. \quad (2.32)$$

Another important operator is the divergence of a vector field, where the following relation applies:

$$\nabla_i A^i = \frac{1}{\sqrt{g}} \partial_i (\sqrt{g} e_i^j A^j) = \frac{\partial_\varphi A^{\hat{\varphi}}}{R(1 + a \cos \theta)} + \frac{\partial_\theta [A^{\hat{\theta}} (1 + a \cos \theta)]}{r(1 + a \cos \theta)}. \quad (2.33)$$

For the special case where $A^i = \nabla^i F$ is the gradient of a scalar function, the following relation may be employed:

$$\Delta F = \nabla_i \nabla^i F = \frac{1}{\sqrt{g}} \partial_i (\sqrt{g} g^{ij} \partial_j F) = \frac{\partial_\varphi^2 A}{R^2 (1 + a \cos \theta)^2} + \frac{\partial_\theta [(1 + a \cos \theta) \partial_\theta F]}{r^2 (1 + a \cos \theta)}. \quad (2.34)$$

Finally, the action of the covariant derivative on a tensor with two indices can be computed using

$$\nabla_i M^{\hat{j}\hat{k}} = e_i^j \partial_i M^{\hat{j}\hat{k}} + \Gamma_{\hat{i}\hat{i}}^{\hat{j}} M^{\hat{\ell}\hat{k}} + \Gamma_{\hat{i}\hat{i}}^{\hat{k}} M^{\hat{j}\hat{\ell}}. \quad (2.35)$$

2.4. Equations of motion for axisymmetric flows on the torus geometry

In this paper, we focus on axisymmetric flows, for which all fluid quantities are independent of the φ angular coordinate. In this case, the continuity equation [Eq. (2.1a)] becomes

$$\frac{\partial \rho}{\partial t} + \frac{\partial_\theta [\rho u^{\hat{\theta}} (1 + a \cos \theta)]}{r(1 + a \cos \theta)} = 0. \quad (2.36)$$

To derive the Cauchy equation [Eq. (2.1b)], let us first consider the viscous contributions to the pressure tensor. Taking the covariant derivatives in Eq. (2.3), the following expressions are obtained for the components of $\tau_{\text{dyn}}^{\hat{i}\hat{j}}$:

$$\begin{aligned}\tau_{\text{dyn}}^{\hat{\theta}\hat{\theta}} &= -\tau_{\text{dyn}}^{\hat{\varphi}\hat{\varphi}} = \frac{\eta}{r}(1 + a \cos \theta) \frac{\partial}{\partial \theta} \left(\frac{u^{\hat{\theta}}}{1 + a \cos \theta} \right), \\ \tau_{\text{dyn}}^{\hat{\theta}\hat{\varphi}} &= \tau_{\text{dyn}}^{\hat{\varphi}\hat{\theta}} = \frac{\eta}{r}(1 + a \cos \theta) \frac{\partial}{\partial \theta} \left(\frac{u^{\hat{\varphi}}}{1 + a \cos \theta} \right),\end{aligned}\quad (2.37)$$

while the volumetric parts are

$$\tau_{\text{bulk}}^{\hat{\theta}\hat{\theta}} = \tau_{\text{bulk}}^{\hat{\varphi}\hat{\varphi}} = \eta_v \nabla_{\hat{k}} u^{\hat{k}} = \frac{\eta_v}{r(1 + a \cos \theta)} \frac{\partial}{\partial \theta} [u^{\hat{\theta}}(1 + a \cos \theta)], \quad (2.38)$$

with $\tau_{\text{bulk}}^{\hat{\theta}\hat{\varphi}} = \tau_{\text{bulk}}^{\hat{\varphi}\hat{\theta}} = 0$. The divergence of $\tau^{\hat{i}\hat{j}}$ is then

$$\begin{aligned}\nabla_{\hat{j}} \tau^{\hat{\theta}\hat{j}} &= \frac{\partial_{\theta} \{ \eta(1 + a \cos \theta)^3 \partial_{\theta} [u^{\hat{\theta}} / (1 + a \cos \theta)] \}}{r^2(1 + a \cos \theta)^2} + \frac{1}{r^2} \frac{\partial}{\partial \theta} \frac{\eta_v \partial_{\theta} [u^{\hat{\theta}}(1 + a \cos \theta)]}{1 + a \cos \theta}, \\ \nabla_{\hat{j}} \tau^{\hat{\varphi}\hat{j}} &= \frac{\partial_{\theta} \{ \eta(1 + a \cos \theta)^3 \partial_{\theta} [u^{\hat{\varphi}} / (1 + a \cos \theta)] \}}{r^2(1 + a \cos \theta)^2}.\end{aligned}\quad (2.39)$$

For the non-dissipative contributions to the pressure tensor, the divergence $\nabla_{\hat{j}} \mathbf{P}_{\kappa}^{\hat{i}\hat{j}}$ of the term involving surface tension can be evaluated using

$$\nabla_{\hat{j}} \mathbf{P}_{\kappa}^{\hat{i}\hat{j}} = -\phi \kappa \nabla^{\hat{i}} \Delta \phi. \quad (2.40)$$

Thus, the $\hat{\varphi}$ component of the Cauchy equation reads as

$$\rho \left\{ \frac{\partial u^{\hat{\varphi}}}{\partial t} + u^{\hat{\theta}} \frac{\partial_{\theta} [u^{\hat{\varphi}}(1 + a \cos \theta)]}{r(1 + a \cos \theta)} \right\} = \frac{\partial_{\theta} \{ \eta(1 + a \cos \theta)^3 \partial_{\theta} [u^{\hat{\varphi}} / (1 + a \cos \theta)] \}}{r^2(1 + a \cos \theta)^2}, \quad (2.41a)$$

while the $\hat{\theta}$ component can be written as:

$$\begin{aligned}\rho \left[\frac{\partial u^{\hat{\theta}}}{\partial t} + \frac{u^{\hat{\theta}}}{r} \frac{\partial u^{\hat{\theta}}}{\partial \theta} + \frac{(u^{\hat{\varphi}})^2 \sin \theta}{R(1 + a \cos \theta)} \right] + \frac{1}{r} \frac{\partial P_b}{\partial \theta} &= \frac{\phi \kappa}{r^3} \frac{\partial}{\partial \theta} \left\{ \frac{\partial_{\theta} [(1 + a \cos \theta) \partial_{\theta} \phi]}{1 + a \cos \theta} \right\} \\ + \frac{\partial_{\theta} \{ \eta(1 + a \cos \theta)^3 \partial_{\theta} [u^{\hat{\theta}} / (1 + a \cos \theta)] \}}{r^2(1 + a \cos \theta)^2} &+ \frac{1}{r^2} \frac{\partial}{\partial \theta} \left\{ \eta_v \frac{\partial_{\theta} [u^{\hat{\theta}}(1 + a \cos \theta)]}{1 + a \cos \theta} \right\}.\end{aligned}\quad (2.41b)$$

To derive the energy equation [Eq. (2.1c)], the following contraction is useful:

$$\begin{aligned}\tau^{\hat{i}\hat{j}} \nabla_{\hat{i}} u_{\hat{j}} &= \frac{1}{2\eta} \tau_{\text{dyn}}^{\hat{i}\hat{j}} \tau_{\text{dyn}}^{\text{dyn}} + \frac{1}{2\eta_v} \tau_{\text{bulk}}^{\hat{i}\hat{j}} \tau_{\text{bulk}}^{\text{bulk}} \\ &= \frac{1}{\eta} \left[(\tau_{\text{dyn}}^{\hat{\theta}\hat{\theta}})^2 + (\tau_{\text{dyn}}^{\hat{\varphi}\hat{\varphi}})^2 \right] + \frac{1}{\eta_v} (\tau_{\text{bulk}}^{\hat{\theta}\hat{\theta}})^2,\end{aligned}\quad (2.42)$$

where the properties $\tau_{\text{dyn}}^{\hat{\varphi}\hat{\varphi}} = -\tau_{\text{dyn}}^{\hat{\theta}\hat{\theta}}$ and $\tau_{\text{bulk}}^{\hat{\theta}\hat{\theta}} = \tau_{\text{bulk}}^{\hat{\varphi}\hat{\varphi}}$ have been used. Thus, the energy equation can be written as

$$\begin{aligned}\rho \left(\frac{\partial e}{\partial t} + \frac{u^{\hat{\theta}}}{r} \frac{\partial e}{\partial \theta} \right) + \frac{P_b \partial_{\theta} [u^{\hat{\theta}}(1 + a \cos \theta)]}{r(1 + a \cos \theta)} \\ = \frac{1}{r^2} \frac{\partial_{\theta} [(1 + a \cos \theta) \kappa \partial_{\theta} T]}{1 + a \cos \theta} + \frac{1}{\eta} \left[(\tau_{\text{dyn}}^{\hat{\theta}\hat{\theta}})^2 + (\tau_{\text{dyn}}^{\hat{\varphi}\hat{\varphi}})^2 \right] + \frac{1}{\eta_v} (\tau_{\text{bulk}}^{\hat{\theta}\hat{\theta}})^2.\end{aligned}\quad (2.43)$$

Finally, on the torus, the Cahn-Hilliard equation, Eq. (2.12), reduces to

$$\frac{\partial \phi}{\partial t} + \frac{\partial_{\theta}[\phi u^{\hat{\theta}}(1 + a \cos \theta)]}{r(1 + a \cos \theta)} = \frac{M}{r^2} \frac{\partial_{\theta}[(1 + a \cos \theta)\partial_{\theta}\mu]}{1 + a \cos \theta}, \quad (2.44)$$

where the chemical potential is computed using

$$\mu = -A\phi(1 - \phi^2) - \frac{\kappa}{r^2} \frac{\partial_{\theta}[(1 + a \cos \theta)\partial_{\theta}\phi]}{1 + a \cos \theta}. \quad (2.45)$$

3. Sound speed for perfect fluids

The first problem we study in this work is sound wave propagation for perfect fluids on the torus geometry. In fluids, sound waves provide the basic mechanism of information propagation. Many interesting phenomena involving the properties of sound wave propagation form the object of focus in acoustics. In addition, due to their fundamental importance, sound wave propagation should be considered as a first benchmark for any hydrodynamics solver. For perfect fluids, we neglect dissipative effects, such that the dynamic viscosity η and the heat conductivity k can be taken to be zero. For simplicity, we will also set the surface tension parameter κ and the mobility M in the Cahn-Hilliard equation to zero.

Focussing on sound wave propagation along the poloidal (θ) direction of the torus, we will show that the sound waves exhibit a discrete spectrum of harmonics. The eigenfrequencies corresponding to these harmonics can be related to those of the standard Fourier harmonics for periodic domains, but, surprisingly the eigenfrequencies corresponding to odd and even modes have different values, unlike for a planar geometry (Rieutord 2015; Busuioc *et al.* 2020a). The eigenfunctions describing the spatial dependence also generalise from the usual harmonic sine and cosine basis to more complex odd and even functions. We determine the eigenfunctions using a perturbative approach, starting with the harmonic functions at zeroth order.

This section is structured as follows. The general solution for the propagation of longitudinal waves is presented in Subsec. 3.1. Then, two benchmark problems are proposed in Subsecs. 3.2 and 3.3.

3.1. General solution

Let us consider small perturbations around a stationary, background state at density ρ_0 , internal energy e_0 and order parameter ϕ_0 , having bulk pressure $P_0 \equiv P_b(\rho_0, e_0, \phi_0)$:

$$\rho = \rho_0(1 + \delta\rho), \quad e = e_0(1 + \delta e), \quad P_b = P_0(1 + \delta P), \quad \phi = \phi_0 + \delta\phi. \quad (3.1)$$

The perturbations in the pressure δP can be expressed as

$$\delta P = \frac{\rho_0 P_{\rho,0}}{P_0} \delta\rho + \frac{e_0 P_{e,0}}{P_0} \delta e + \frac{P_{\phi,0}}{P_0} \delta\phi, \quad (3.2)$$

where for brevity the following notation is introduced:

$$P_{\rho} = \frac{\partial P_b}{\partial \rho}, \quad P_e = \frac{\partial P_b}{\partial e}, \quad P_{\phi} = \frac{\partial P_b}{\partial \phi}. \quad (3.3)$$

The subscripts 0 in Eq. (3.2) indicate that the derivatives of the pressure are computed for the background state.

Assuming that the velocity components $u^{\hat{\theta}}$ and $u^{\hat{\phi}}$ are small, and neglecting all

second-order terms of the perturbations introduced, the continuity [Eq. (2.36)], Cauchy [Eq. (2.41)], energy [Eq. (2.43)] and Cahn-Hilliard [Eq. (2.44)] equations reduce to

$$\begin{aligned}\frac{\partial \delta \rho}{\partial t} + \frac{\partial_{\theta} \mathcal{U}}{r(1+a \cos \theta)} &= 0, \\ \frac{\partial \mathcal{U}}{\partial t} + \frac{P_0(1+a \cos \theta)}{\rho_0 r} \frac{\partial \delta P}{\partial \theta} &= 0, \\ \frac{\partial \delta e}{\partial t} + \frac{P_0}{\rho_0 e_0} \frac{\partial_{\theta} \mathcal{U}}{r(1+a \cos \theta)} &= 0, \\ \frac{\partial \delta \phi}{\partial t} + \frac{\phi_0 \partial_{\theta} \mathcal{U}}{r(1+a \cos \theta)} &= 0,\end{aligned}\tag{3.4}$$

while $\partial_t u^{\hat{\phi}} = 0$. Note that, in the above, we introduced the following notation

$$\mathcal{U} = u^{\hat{\theta}}(1+a \cos \theta).\tag{3.5}$$

Taking the time derivative of the second relation in Eq. (3.4) and replacing δP with Eq. (3.2) gives

$$\frac{\partial^2 \mathcal{U}}{\partial t^2} - \frac{c_{s,0}^2}{r^2}(1+a \cos \theta) \frac{\partial}{\partial \theta} \left(\frac{1}{1+a \cos \theta} \frac{\partial \mathcal{U}}{\partial \theta} \right) = 0.\tag{3.6}$$

Eq. (3.6) represents the generalisation of the sound wave equation for axisymmetric flows on the torus geometry. We can recognise $c_{s,0}$ as the sound speed corresponding to the background fluid parameters. In general, c_s^2 can be computed using

$$c_s^2 = P_{\rho} + \frac{P_b}{\rho^2} P_e + \frac{\phi}{\rho} P_{\phi}.\tag{3.7}$$

For the ideal gas, $P_b = \rho k_B T/m$ and $c_s = \sqrt{\gamma P_b/\rho}$, where $\gamma = 1 + k_B/mc_v$ is the adiabatic index (e.g. $\gamma = 2$ for a monoatomic ideal gas with 2 translational degrees of freedom). The isothermal regime can be recovered by setting $c_v \rightarrow \infty$ and $\gamma \rightarrow 1$. For the isothermal ideal fluid, we recover $c_s = \sqrt{k_B T/m}$.

Eq. (3.6) can be solved using the method of separation of variables with the following ansatz

$$\mathcal{U}(t, \theta) \rightarrow \mathcal{U}_n(t, \theta) = U_n(t) \Psi_n(\theta).\tag{3.8}$$

The index n reflects the fact that there are more than one possible solutions, corresponding to a discrete set of eigenvalues λ_n . The temporal function corresponds to simple harmonic oscillations of the form

$$\ddot{U}_n = -\lambda_n^2 \frac{c_{s,0}^2}{r^2} U_n.\tag{3.9}$$

The angular functions satisfy the differential equation

$$(1+a \cos \theta) \frac{d}{d\theta} \left(\frac{1}{1+a \cos \theta} \frac{d\Psi_n}{d\theta} \right) + \lambda_n^2 \Psi_n = 0.\tag{3.10}$$

The functions Ψ_n are twice differentiable periodic solutions with a discrete set of eigenvalues λ_n . Eq. (3.10) has even and odd solutions, which we denote by $f_n(\theta)$ and $g_n(\theta)$. It can be shown that these functions are orthogonal with respect to the inner product, which is defined below for two functions $\psi(\theta)$ and $\chi(\theta)$:

$$\langle \psi, \chi \rangle = \int_0^{2\pi} \frac{d\theta}{2\pi} \frac{\psi(\theta) \chi(\theta)}{1+a \cos \theta}.\tag{3.11}$$

We seek solutions of unit norm, such that

$$\langle f_n, f_{n'} \rangle = \delta_{n,n'}, \quad \langle g_n, g_{n'} \rangle = \delta_{n,n'}, \quad \langle f_n, g_{n'} \rangle = 0. \quad (3.12)$$

The zeroth mode solution, corresponding to $n = 0$ and $\lambda_0 = 0$, is straightforward to identify. The solution is a constant. Exploiting the condition of unit norm, we can use the following integral

$$\frac{1}{2\pi} \int_0^{2\pi} \frac{d\theta}{1 + a \cos \theta} = \frac{1}{\sqrt{1 - a^2}} \quad (3.13)$$

to obtain that

$$f_0(\theta) = (1 - a^2)^{1/4}. \quad (3.14)$$

There is no antisymmetric solution corresponding to $n = 0$ and $\lambda_0 = 0$.

We will now discuss the subsequent values of $\lambda_{c;n}$ and $\lambda_{s;n}$, the eigenvalues of the even (f_n) and odd (g_n) solutions. More specifically, the pairs ($f_n, \lambda_{c;n}$) and ($g_n, \lambda_{s;n}$) satisfy Eq. (3.10):

$$\begin{aligned} (1 + a \cos \theta) \frac{d}{d\theta} \left(\frac{1}{1 + a \cos \theta} \frac{df_n}{d\theta} \right) + \lambda_{c;n}^2 f_n &= 0, & f_n(\theta) &= f_n(2\pi - \theta), \\ (1 + a \cos \theta) \frac{d}{d\theta} \left(\frac{1}{1 + a \cos \theta} \frac{dg_n}{d\theta} \right) + \lambda_{s;n}^2 g_n &= 0, & g_n(\theta) &= -g_n(2\pi - \theta). \end{aligned} \quad (3.15)$$

We index the solutions incrementally such that f_{n+1} has an eigenvalue $\lambda_{c;n+1} > \lambda_{c;n}$, and similarly for the odd solutions.

Eq. (3.10) can be solved analytically in the limit case $a = 0$ (corresponding to an infinitely wide torus, $R \rightarrow \infty$). In this case, when $n > 0$, Eq. (3.10) yields the usual (normalised) harmonic basis encountered on a system with periodic coordinate θ :

$$f_n = \sqrt{2} \cos n\theta, \quad g_n = \sqrt{2} \sin n\theta. \quad (3.16)$$

Here, $\lambda_{c;n} = \lambda_{s;n} = n$. For $n = 0$, Eq. (3.14) reduces to $f_0(\theta) = 1$.

Another limit where the analytical solution is available is when $a = 1$. In this case, the eigenfrequency spectrum is derived in Eqs. (SM:3.13) and (SM:3.17) and is reproduced below, for convenience

$$\lambda_{c;n}^2 = n^2 - \frac{1}{4}, \quad \lambda_{s;n}^2 = n(n + 1). \quad (3.17)$$

The derivation and explicit form of the eigenfunctions for $a = 1$ are given in Sec. SM:3.2.1 of the supplementary material.

For intermediate values of a (i.e. for $0 < a < 1$) and $\lambda_n^2 > 0$, there is no known analytic solution of Eq. (3.10). However, given that $a < 1$, it is reasonable to seek for the solutions in a perturbative manner. Starting from the $a = 0$ solution in Eq. (3.16), for a given value of n , we expect that the perturbation procedure will bring in harmonics corresponding to $n \pm 1$, $n \pm 2$, and so forth. The eigenvalues $\lambda_{c;n}$ and $\lambda_{s;n}$ travel along a continuous path from $\lambda_{c;n} = n$ to $\lambda_{c;n} = \sqrt{n^2 - \frac{1}{4}}$, and from $\lambda_{s;n} = n$ to $\lambda_{s;n} = \sqrt{n(n + 1)}$, respectively, as a goes from 0 to 1. The perturbative procedure is discussed in Appendix B and the results for $1 \leq n \leq 4$ are given up to $O(a^9)$ in Eq. (SM:3.3) of the supplementary material.

In general, the eigenvalues $\lambda_{c;n}$ and $\lambda_{s;n}$ for the even and odd modes of the same order n are not equal. As discussed in Appendix B, the difference between $\lambda_{c;n}$ and $\lambda_{s;n}$ appears via terms of order $O(a^{2n})$. table 1 shows the values of $\lambda_{c;n}$ and $\lambda_{s;n}$ obtained using high precision numerical integration for the cases $a = 0.4$ and $a = 0.8$. It can be seen that the difference between $\lambda_{c;n}$ and $\lambda_{s;n}$ decreases as n is increased and a is kept fixed, or

n	$a = 0.4$		$a = 0.8$	
	$\lambda_{c;n}$	$\lambda_{s;n}$	$\lambda_{c;n}$	$\lambda_{s;n}$
1	0.99283837	1.03615819	0.96123389	1.19709137
2	2.00528264	2.00700233	2.01720533	2.07891859
3	3.00388532	3.00395489	3.02259288	3.03709989
4	4.00289664	4.00289952	4.01992604	4.02335307
5	5.00230332	5.00230344	5.01664927	5.01747046
6	6.00191275	6.00191276	6.01401146	6.01421028
7	7.00163605	7.00163605	7.01201841	7.01206689
8	8.00142960	8.00142960	8.01050233	8.01051420
9	9.00126957	9.00126957	9.00932177	9.00932469
10	10.00114185	10.00114185	10.00837943	10.00838015

Table 1. Eigenvalues $\lambda_{c;n}$ and $\lambda_{s;n}$ corresponding to the even (f_n) and odd (g_n) solutions of Eq. (3.10) with $a = 0.4$ (left) and $a = 0.8$ (right), for $0 < n \leq 10$. The eigenvalue $\lambda_{c;0} = 0$, corresponding to (3.14), is not shown here.

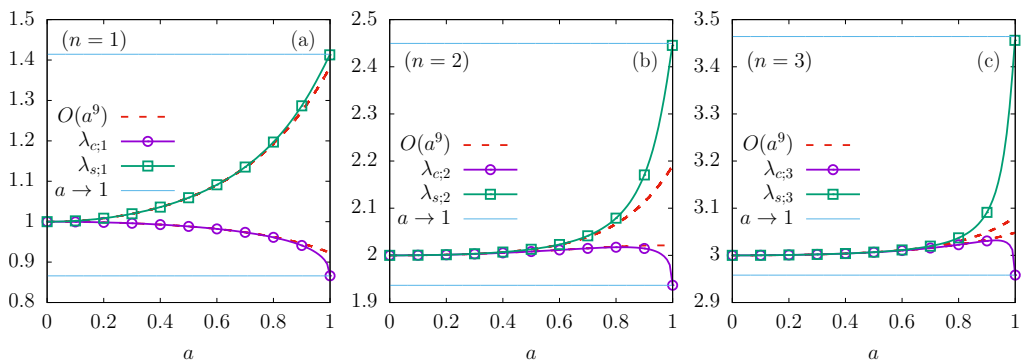


Figure 2. The dependence of $\lambda_{c;n}$ and $\lambda_{s;n}$ on a for $n = 1$ (a), 2 (b) and 3 (c), respectively. The solid lines with symbols represent the numerically evaluated values of the eigenfrequencies, while the dotted lines show the perturbative approximations with terms up to $O(a^9)$. The horizontal lines show the $a = 1$ limits given in Eq. (3.17).

as n is kept fixed and a is decreased. This is in contrast to the flat geometry, where the eigenvalues for the even and odd modes of the same order n are always identical.

The dependence of $\lambda_{c;n}$ and $\lambda_{s;n}$ on a is revealed in figures 2(a)-2(c) for $n = 1, 2$ and 3. It can be seen that, as $a \rightarrow 1$, $\lambda_{c;n}$ also has a strong variation with a . However, overall the variation of $\lambda_{c;n}$ with a is significantly milder than that of $\lambda_{s;n}$. For comparison, the dotted lines corresponding to the perturbative approximations up to $O(a^9)$, and the limits $\lim_{a \rightarrow 1} \lambda_{c;n} = \sqrt{n^2 - \frac{1}{4}}$ and $\lim_{a \rightarrow 1} \lambda_{s;n} = \sqrt{n(n+1)}$ are also shown.

figures 3(a) and 3(b) show the even and odd eigenfunctions f_n and g_n corresponding to $1 \leq n \leq 4$ over the half-domain $0 \leq \theta \leq \pi$ with $a = 0.4$. Similarly, figures 3(c) and 3(d) show f_n and g_n when $a = 0.8$. It can be seen that the amplitudes for the even harmonics f_n become weaker towards $\theta = \pi$ as a is increased, while the amplitudes of the odd harmonics g_n become weaker towards $\theta = 0$.

Assuming that the functions $\{f_n, g_n\}$ form a complete set, the fluid velocity can in

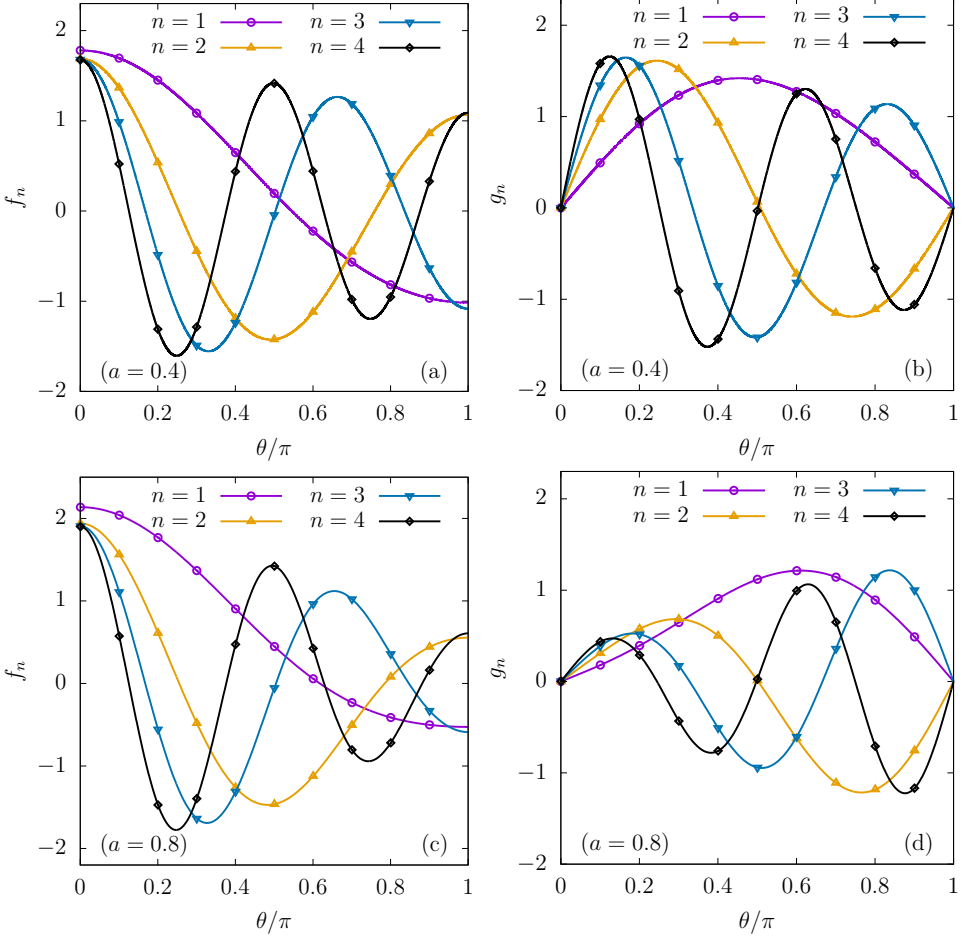


Figure 3. The even and odd eigenfunctions f_n (left) and g_n (right) of Eq. (3.10), with $a = 0.4$ (top) and $a = 0.8$ (bottom), for $n = 1, 2, 3$ and 4 . The eigenvalues are summarised in table 1.

general be written as

$$u^{\hat{\theta}}(t, \theta) = \frac{1}{1 + a \cos \theta} \sum_{n=0}^{\infty} [U_{c;n}(t) f_n(\theta) + U_{s;n}(t) g_n(\theta)]. \quad (3.18)$$

Such an expansion is consistent when the inner product, Eq. (3.11), is dual to the following completeness relation:

$$\sum_{n=0}^{\infty} [f_n(\theta) f_n(\theta') + g_n(\theta) g_n(\theta')] = 2\pi(1 + a \cos \theta) \delta(\theta - \theta'). \quad (3.19)$$

Solving Eq. (3.9), it can be seen that the even and odd solutions for the temporal function (for $n > 0$) correspond to simple harmonic oscillations

$$U_{c;n}(t) = U_{c;n;0} \cos(\omega_{c;n} t + \vartheta_{c;n}), \quad U_{s;n}(t) = U_{s;n;0} \sin(\omega_{s;n} t + \vartheta_{s;n}), \quad (3.20)$$

where $\omega_{c;n} = \lambda_{c;n} c_s / r$ and $\omega_{s;n} = \lambda_{s;n} c_s / r$. The coefficients $U_{c;n;0}$ and $U_{s;n;0}$ and the

phases $\vartheta_{c;n}$ and $\vartheta_{s;n}$ can be determined from the initial conditions

$$u^{\hat{\theta}}(0, \theta) = u_0^{\hat{\theta}}(\theta), \quad \dot{u}^{\hat{\theta}}(0, \theta) = -\frac{P_0}{\rho_0 r} \partial_{\theta} \delta P_0(\theta), \quad (3.21)$$

where $u_0^{\hat{\theta}}(\theta)$ represents the initial velocity profile, while $\delta P_0(\theta) = \delta P(0, \theta) = (P_b(0, \theta) - P_0)/P_0$ represents the initial pressure fluctuations. Projecting the above equations onto f_n and g_n yields

$$\begin{aligned} \begin{pmatrix} U_{c;n;0} \cos \vartheta_{c;n} \\ U_{s;n;0} \sin \vartheta_{s;n} \end{pmatrix} &= \int_0^{2\pi} \frac{d\theta}{2\pi} \begin{pmatrix} f_n \\ g_n \end{pmatrix} u_0^{\hat{\theta}}(\theta), \\ \begin{pmatrix} U_{c;n;0} \sin \vartheta_{c;n} \\ -U_{s;n;0} \cos \vartheta_{s;n} \end{pmatrix} &= \frac{P_0}{\rho_0 c_s} \int_0^{2\pi} \frac{d\theta}{2\pi} \begin{pmatrix} f_n/\lambda_{c;n} \\ g_n/\lambda_{s;n} \end{pmatrix} \frac{\partial \delta P_0}{\partial \theta}, \end{aligned} \quad (3.22)$$

where the last equation applies only for $n > 0$. It is worth noting that the $n = 0$ term, corresponding to the incompressible flow profile

$$\frac{U_{c;0} f_0(\theta)}{1 + a \cos \theta}, \quad (3.23)$$

is time-independent and its amplitude, $U_{c;0}$, is preserved at all times. Thus, numerical methods developed for hydrodynamics on curved surfaces should ensure the preservation of the above profile. In the Cartesian geometry, the incompressible flow profile along a single axis is a constant background velocity, which should be preserved due to the Galilean invariance of the theory.

For the rest of this work, we employ expansions of up to a^9 of the eigenfunctions, eigenvalues and all related quantities. These expansions are given in Eq. (SM:3.3) of the supplementary material. Although some expansions converge faster than the others, for consistency reasons, we choose to employ the same order of expansion for all quantities involved.

3.2. First benchmark: Constant initial flow

We now formulate a simple numerical experiment that can be used to benchmark the capabilities of numerical methods to capture sound wave propagation on curved geometries. The simplest configuration giving rise to sound wave propagation corresponds to

$$u_0^{\hat{\theta}}(\theta) = U_0, \quad \delta P_0(\theta) = 0, \quad (3.24)$$

with U_0 a constant. Since the initial velocity profile is symmetric and the initial pressure is constant, $\vartheta_{c;n} = 0$ and $U_{s;n;0} = 0$. To calculate the coefficients of the even modes, we take advantage of the projections introduced in Eq. (3.22). The fluid velocity can then be written as

$$\begin{aligned} u^{\hat{\theta}}(t, \theta) &= \frac{1}{1 + a \cos \theta} \left[U_0 \sqrt{1 - a^2} + \sum_{n=1}^{\infty} U_{c;n}(t) f_n(\theta) \right], \\ U_{c;n}(t) &= U_0 I_{c;0;n} \cos \left(\frac{c_{s,0} \lambda_{c;n}}{r} t \right), \end{aligned} \quad (3.25)$$

where the eigenvalues $\lambda_{c;n}$ are given up to 9th order with respect to a in Eq. (SM:3.3), and the integrals $I_{*,m;n}$ are defined as

$$I_{c;m;n} = \int_0^{2\pi} \frac{d\theta}{2\pi} \frac{f_n(\theta)}{(1 + a \cos \theta)^m}, \quad I_{s;m;n} = \int_0^{2\pi} \frac{d\theta}{2\pi} \frac{g_n(\theta) \sin \theta}{(1 + a \cos \theta)^m}. \quad (3.26)$$

Fluid type	Regime	$c_{s,0}$	ω_1	ω_2	ω_3
Ideal gas	Iso	1	1.24104796	2.50660330	3.75485665
	Th	$\sqrt{2}$	1.75510686	3.54487238	5.31016920
Cahn-Hilliard multicomponent	$\phi_0 = 0.8$	1.26047610	1.56431130	3.15951355	4.73290707
	$\phi_0 = 1.0$	1.73205081	2.14955813	4.34156426	6.50360249

Table 2. Sound speed and angular frequencies $\omega_n = c_{s,0}\lambda_{c;n}/r$ for the first three harmonics of the oscillatory motion on the torus with $a = 0.4$, considered in figure 4.

In this section, we only need the case with $m = 0$, for which $I_{c;0;0} = (1 - a^2)^{1/4}$, while the first integrals ($1 \leq n \leq 4$) are given up to 9th order with respect to a in Eq. (SM:3.3) of the supplementary material. The integrals $I_{s;0;n}$ of the odd functions will be employed later, in Subsec. 3.3.

In order to perform numerical simulations, we consider a non-dimensionalisation of physical quantities with respect to the background fluid parameters, such that $\rho_0 = T_0 = P_0 = 1$. Focussing on the torus with $a = r/R = 0.4$, we take the reference length scale such that $R = 2$. Setting the reference velocity naturally to $c_0 = \sqrt{P_0/\rho_0}$, we initialise the velocity by setting $u_0^{\hat{a}}(\theta) = U_0 = 10^{-5}$ in Eq. (3.24). Using the aforementioned reference velocity, the non-dimensional sound speed is $c_{s,0} = 1$ for the isothermal case and $c_{s,0} = \sqrt{2}$ for the thermal case when the adiabatic index is $\gamma = 2$. In addition, we also consider an isothermal multicomponent fluid for which the sound speed is given by

$$c_{s,0}^2 = \frac{k_B T_0}{m} - \frac{A\phi_0^2}{\rho_0}(1 - 3\phi_0^2). \quad (3.27)$$

We choose $A = 1$; and consider values of $\phi_0 = 1$ and $\phi_0 = 0.8$, which are outside the spinodal region, $-\frac{1}{\sqrt{3}} < \phi_0 < \frac{1}{\sqrt{3}}$. The resulting sound speeds are summarised in table 2.

For the four cases above with differing sound speeds, the system is evolved between $0 \leq t \leq 18$ on a grid with $N_\theta = 320$ equidistant nodes and a time step $\delta t = 5 \times 10^{-4}$. The velocity profile is projected onto the basis functions f_1 , f_2 and f_3 , as given in Eqs. (SM:3.3a), (SM:3.3c) and (SM:3.3e) of the supplementary material, respectively. The simulation results are shown using dashed lines and symbols in figure 4. For comparison, the corresponding analytical solutions in Eq. (3.25) are shown in solid lines in figure 4. The angular frequencies, $\omega_n = c_{s,0}\lambda_{c;n}/r$, for the first three harmonics are reported for convenience in table 2. The agreement between the analytical and numerical results is excellent. It is also worth noting that the angular frequencies on the torus differ from those for the flat geometry, and the deviations become more significant with increasing a .

3.3. Second benchmark test: Even and odd initial conditions

The purpose of the second test is to highlight the difference in the period corresponding to the propagation of even and odd perturbations. As highlighted in figure 2, the difference in the frequencies for the even and odd modes increases as a is increased. For this reason, in this example we consider $a = 0.8$. According to table 1, the ratio $\lambda_{s;1}/\lambda_{c;1} \simeq 1.25$, therefore the $n = 1$ odd mode should exhibit 5 periods for every 4 periods of the $n = 1$ even mode.

We consider two initial conditions, corresponding to even and odd initial velocity

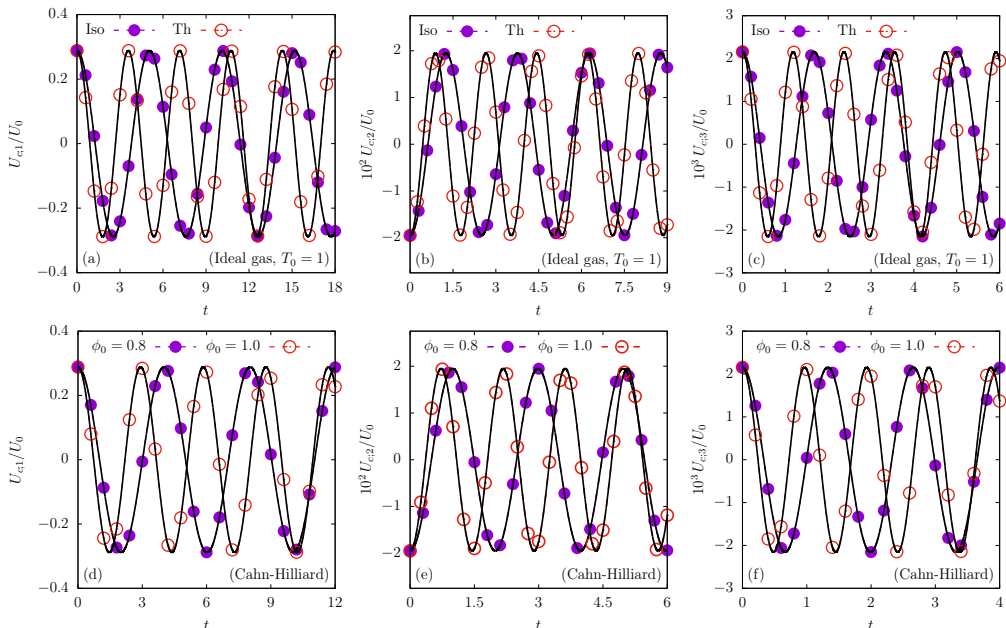


Figure 4. Comparison between the numerical results (symbols) and analytical predictions (solid lines) for the evolution of $U_{c;n}(t)/U_0$, as given in Eq. (3.25). The first row (a-c) is for isothermal (Iso) and thermal (Th) ideal fluids, while the second row (d-f) is for Cahn-Hilliard multicomponent fluid. The integrals $I_{c;0;n}$ given in Eq. (SM:3.3) have the values of $I_{c;0;1} \simeq 0.288$ (left); $I_{c;0;2} \simeq -0.0195$ (middle); and $I_{c;0;3} \simeq 0.00216$ (right).

n	$U_{c;n;0}^{\text{even}}/U_0$	$U_{s;n;0}^{\text{odd}}/U_0$
1	0.67162788	0.55445076
2	0.21755576	-0.09426691
3	-0.03806432	-0.01672761
4	0.01098141	-0.00461361

Table 3. Values of the normalised amplitudes $U_{c;n;0}^{\text{even}}/U_0$ and $U_{s;n;0}^{\text{odd}}/U_0$ defined in Eq. (3.30) for $a = 0.8$ and $1 \leq n \leq 4$.

profiles

$$u_{0;\text{even}}^{\hat{\theta}}(\theta) = U_0 \cos \theta, \quad u_{0;\text{odd}}^{\hat{\theta}}(\theta) = U_0 \sin \theta, \quad (3.28)$$

where U_0 is the (constant) initial amplitude. As before, the initial pressure perturbation is assumed to vanish, i.e. $\delta P_{0;\text{even}}(\theta) = \delta P_{0;\text{odd}}(\theta) = 0$. According to Eq. (3.22), this implies that the offset angles can be taken as $\vartheta_{c;n} = 0$ and $\vartheta_{s;n} = \pi/2$. Furthermore, since $\int_0^{2\pi} d\theta \cos \theta = 0$, the coefficient $U_{c;n;0}^{\text{even}}$ of the zeroth mode (corresponding to $n = 0$) vanishes. This allows the velocity to be expanded in the two cases as follows:

$$u_{\text{even}}^{\hat{\theta}}(t, \theta) = \sum_{n=1}^{\infty} \frac{U_{c;n;0}^{\text{even}} f_n(\theta)}{1 + a \cos \theta} \cos(\omega_{c;n;0} t), \quad u_{\text{odd}}^{\hat{\theta}}(t, \theta) = \sum_{n=1}^{\infty} \frac{U_{s;n;0}^{\text{odd}} g_n(\theta)}{1 + a \cos \theta} \cos(\omega_{s;n;0} t), \quad (3.29)$$

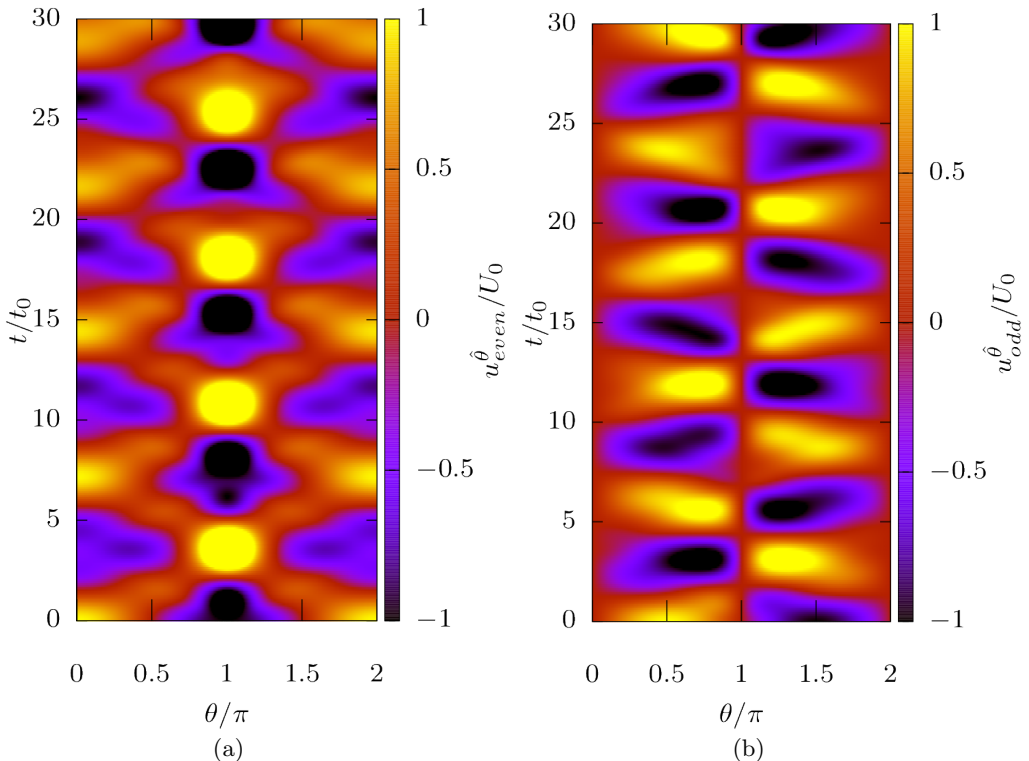


Figure 5. Time evolution of $u_{\text{even}}^{\hat{\theta}}/U_0$ (a) and $u_{\text{odd}}^{\hat{\theta}}/U_0$ (b), defined in Eq. (3.29) on the torus with $a = 0.8$. The horizontal axis represents the angular coordinate along the poloidal direction, normalised with respect to π . The vertical axis shows the time coordinate t , normalised with respect to $t_0 = R/2c_0$, where $c_0 = \sqrt{P_0/\rho_0}$ is the reference speed. The colour map represents the value of $u^{\hat{\theta}}/U_0$ and is truncated to the interval $[-1, 1]$.

where $U_{s;n;0}^{\text{even}} = U_{c;n;0}^{\text{odd}} = 0$, while

$$\begin{aligned}
 U_{c;n;0}^{\text{even}} &= U_0 \int_0^{2\pi} \frac{d\theta}{2\pi} f_n(\theta) \cos \theta = U_0 \frac{\lambda_{c;n}^2}{a(2 - \lambda_{c;n}^2)} I_{c;0;n}, \\
 U_{s;n;0}^{\text{odd}} &= U_0 \int_0^{2\pi} \frac{d\theta}{2\pi} g_n(\theta) \sin \theta = U_0 I_{s;0;n},
 \end{aligned} \tag{3.30}$$

where the first relation follows from noting that $\cos \theta = a^{-1}(1 + a \cos \theta) - a^{-1}$, while the integral $I_{c;-1;n}$ can be expressed in terms of $I_{c;0;n}$ by multiplying the first line of Eq. (3.15) with $(1 + a \cos \theta)/2\pi$ and integrating with respect to θ :

$$I_{c;-1;n} = \int_0^{2\pi} \frac{d\theta}{2\pi} (1 + a \cos \theta) f_n(\theta) = \frac{2}{2 - \lambda_{c;n}^2} I_{c;0;n}. \tag{3.31}$$

As can be seen from table 3, at $a = 0.8$, the coefficient of the $n = 1$ mode is dominant. For the even initial conditions, the amplitude of the $n = 2$ mode is almost a third of the amplitude of the $n = 1$ mode, thus it can be expected that a modulation due to this mode will show up in the solution. This is less important for the odd initial conditions, since $U_{s;2;0}^{\text{odd}}$ is almost 6 times smaller in magnitude than $U_{s;1;0}^{\text{odd}}$.

We now consider an ideal perfect thermal fluid with $\gamma = 2$ and employ the non-

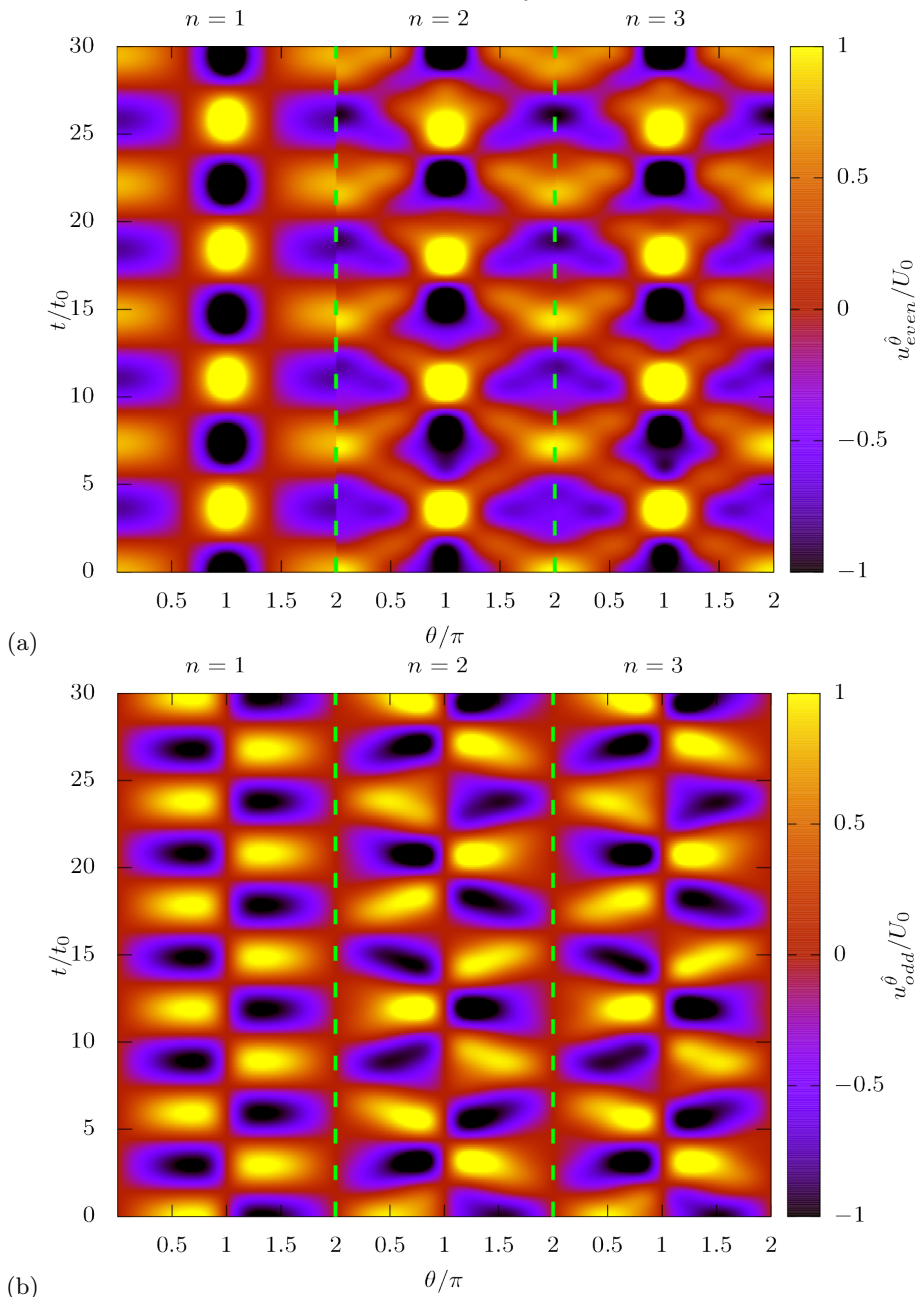


Figure 6. Analytic solutions for $u_{\text{even}}^{\hat{\theta}}(t, \theta)/U_0$ (a) and $u_{\text{odd}}^{\hat{\theta}}(t, \theta)/U_0$ (b), reconstituted via Eq. (3.29) using the harmonics up to $n = 1$ (left), 2 (middle) and 3 (right).

dimensionalisation according to which $\rho_0 = T_0 = P_0 = 1$, $R = 2$ ($r = 1.6$ such that $a = 0.8$), and $c_0 = \sqrt{P_0/\rho_0}$. The constant in Eq. (3.28) is set to $U_0 = 10^{-5}$. In this case, the angular frequency for the first even mode is $\omega_{c;1} = c_{s;0}\lambda_{c;1}/r \simeq 0.85$ and the time required for 4 periods for this mode is $8\pi/\omega_{c;1} \simeq 29.58$. The angular frequency for the first odd mode is $\omega_{s;1} = c_{s;0}\lambda_{s;1}/r \simeq 1.06$ and the time required for 5 periods for

this mode is $10\pi/\omega_{s;1} \simeq 29.69$. We thus perform simulations covering the time domain $0 \leq t \leq 30$, using $N_\theta = 320$ nodes distributed equidistantly along the θ direction and a time step $\delta t = 10^{-3}$. The velocity configuration is saved every 100 time steps, yielding a total of 300 snapshots, which are arranged in time lapses, as shown in figures 5(a) and 5(b). The ratio $u^{\hat{\theta}}/U_0$ is represented using a colour map, which is truncated to the values $[-1, 1]$ for better visibility. It can be seen that the number of (quasi-)periods for the even and odd initial conditions are 4 and 5, as predicted based on the values of $\lambda_{c;1}$ and $\lambda_{s;1}$, respectively.

Finally, we discuss the emergence of the apparent periodicity breakdown observed in figures 5(a) and 5(b) for the even and odd initial conditions considered in this section. Figure 6 shows the analytic solutions for $u_{\text{even}}^{\hat{\theta}}$ (a) and $u_{\text{odd}}^{\hat{\theta}}$ (b) derived in Eq. (3.29), truncated at $n = 1$ (left), 2 (middle) and 3 (right). We note that the amplitude of the zeroth-order harmonic vanishes when the initial state is prepared according to Eq. (3.28). The resulting configurations for different truncations are separated using dashed vertical green lines. It can be seen that the first-order harmonic exhibits the fundamental periodicity observed also in figure 5. Adding the second harmonic produces a visible disturbance since the amplitude ratios $U_{c;2;0}/U_{c;1;0} \simeq 0.324$ and $U_{s;2;0}/U_{s;1;0} \simeq -0.170$ are non-negligible. Because the ratios $\omega_{c;2}/\omega_{c;1} \simeq 2.099$ and $\omega_{s;2}/\omega_{s;1} \simeq 1.737$ are irrational numbers, the resulting configurations become pseudo-periodic. This is different from the flat geometry case where the ratios are integers, thereby conserving the periodicity of the solution. The addition of the third-order harmonic has a significantly milder effect, since the ratios $U_{c;3;0}/U_{c;1;0} \simeq -0.057$ and $U_{s;3;0}/U_{s;1;0} \simeq -0.030$ are small. Therefore, the middle configuration presented in figure 6 already provides a reasonable approximation of the configurations observed in figure 5.

4. Viscous fluid: shear wave damping

In this section, we address the equivalent on the torus of a standard benchmark problem for viscous flow solvers. On the flat geometry, the shear wave setup typically consists of a system which is homogeneous in two directions, say the y and z axes. However, the fluid velocity in one of the directions, say the y component, varies with respect to the x axis. Due to this dependence, layers which are adjacent with respect to the x direction travel at different velocities along the y direction. Due to friction, the velocity difference between two such adjacent layers experiences a damping which is controlled by the kinematic viscosity of the fluid and is induced via the viscous part of the stress tensor. In the present case of the torus geometry, we consider that the poloidal component $u^{\hat{\theta}}$ of the fluid velocity vanishes, while its azimuthal component $u^{\hat{\varphi}}$ varies in magnitude as a function of the poloidal angle θ .

This section is structured as follows. In Subsec. 4.1, the general solution for the shear wave damping problem on the torus is obtained. Subsections 4.2 and 4.3 discuss two benchmark problems proposed in this context.

4.1. General solution

For the torus geometry, we consider the axisymmetric flow of an ideal, single-component fluid with vanishing poloidal velocity ($u^{\hat{\theta}} = 0$). In this case, the linearised limit of the φ component of the Cauchy equation [Eq. (2.41a)] reads

$$\partial_t u^{\hat{\varphi}} = \frac{\nu}{r^2(1+a\cos\theta)^2} \frac{\partial}{\partial\theta} \left[(1+a\cos\theta)^3 \frac{\partial}{\partial\theta} \left(\frac{u^{\hat{\varphi}}}{1+a\cos\theta} \right) \right], \quad (4.1)$$

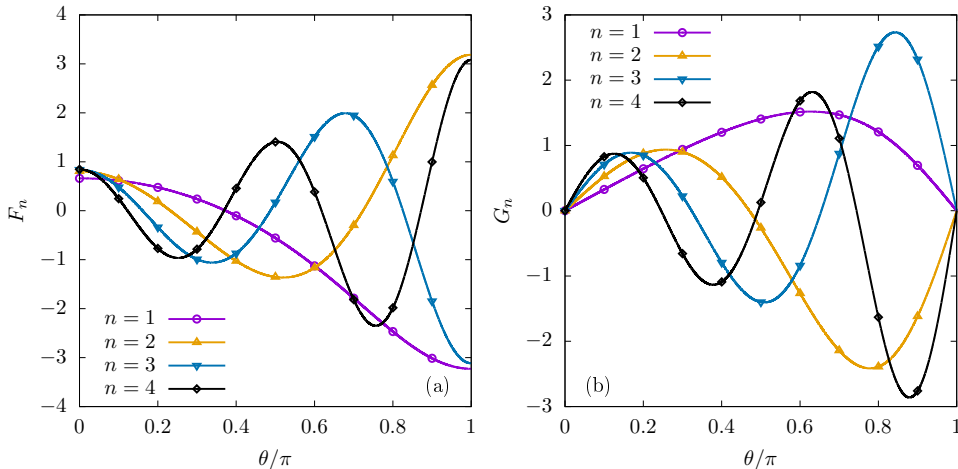


Figure 7. The even and odd eigenfunctions F_n (a) and G_n (b) of Eq. (4.5), summarised in Eq. (SM:3.4), with $a = 0.4$ for $n = 1, 2, 3$ and 4 . The eigenvalues corresponding to $n = 1, 2, 3$ and 4 are $\chi_{c;n} \simeq 1.185, 2.055, 3.035$ and 4.026 for the even modes, and $\chi_{s;n} \simeq 1.060, 2.054, 3.035$ and 4.026 for the odd modes.

with $\rho \simeq \rho_0 = \text{const}$ and $P \simeq P_0 = \text{const}$. In the above, ν represents the kinematic viscosity, which we assume to be constant. The above equation can be solved using separation of variables by letting

$$u^{\hat{\phi}}(t, \theta) \rightarrow u_n^{\hat{\phi}}(t, \theta) = V_n(t) \Lambda_n(\theta) (1 + a \cos \theta). \quad (4.2)$$

Under this separation, the time-dependent amplitude satisfies the equation

$$\partial_t V_n(t) = -\frac{\nu \chi_n^2}{r^2} V_n(t) \Rightarrow V_n(t) = V_{n,0} e^{-\nu \chi_n^2 t / r^2}, \quad (4.3)$$

where χ_n^2 is a constant. The spatial component in Eq. (4.2), $\Lambda_n(\theta)$, satisfies

$$\frac{1}{(1 + a \cos \theta)^3} \frac{\partial}{\partial \theta} \left[(1 + a \cos \theta)^3 \frac{\partial \Lambda_n}{\partial \theta} \right] + \chi_n^2 \Lambda_n = 0. \quad (4.4)$$

Similar to the problem discussed in the previous section, the above equation admits even and odd solutions, which we denote via $F_n(\theta)$ and $G_n(\theta)$, respectively. The index n labels the discrete eigenmodes of Eq. (4.4). We label the eigenvalues $\chi_{c;n}$ and $\chi_{s;n}$ for the even and odd modes, such that

$$\begin{aligned} \frac{1}{(1 + a \cos \theta)^3} \frac{\partial}{\partial \theta} \left[(1 + a \cos \theta)^3 \frac{\partial F_n}{\partial \theta} \right] + \chi_{c;n}^2 F_n &= 0, \\ \frac{1}{(1 + a \cos \theta)^3} \frac{\partial}{\partial \theta} \left[(1 + a \cos \theta)^3 \frac{\partial G_n}{\partial \theta} \right] + \chi_{s;n}^2 G_n &= 0. \end{aligned} \quad (4.5)$$

It can be shown that the modes corresponding to different indices n and n' are orthogonal. We choose the overall normalisation constants by imposing unit norm with respect to the inner product, $\langle F_n, F_{n'} \rangle = \langle G_n, G_{n'} \rangle = \delta_{n,n'}$. For two arbitrary functions Ψ and Φ , the inner product is defined as

$$\langle \Psi, \Phi \rangle = \frac{1}{2\pi} \int_0^{2\pi} d\theta (1 + a \cos \theta)^3 \Psi(\theta) \Phi(\theta). \quad (4.6)$$

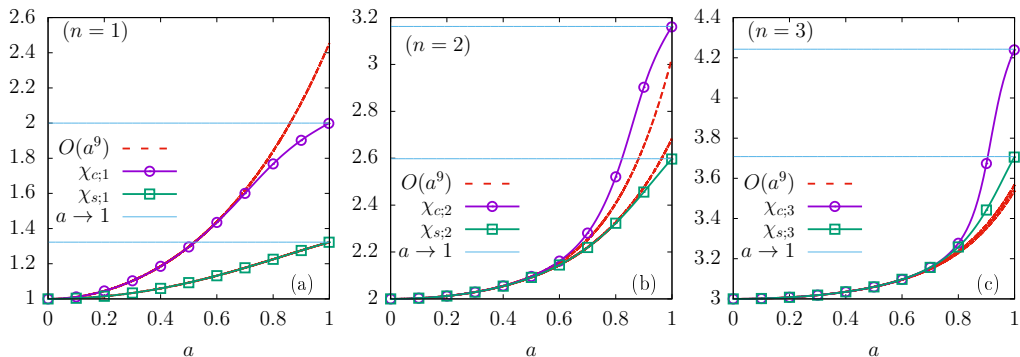


Figure 8. The dependence of $\chi_{c;n}$ and $\chi_{s;n}$ on a for (a) $n = 1$, (b) $n = 2$ and (c) $n = 3$. The dotted lines show the perturbative approximations in Eq. (SM:3.4) with terms up to $O(a^9)$.

The solution of Eq. (4.4) corresponding to $n = 0$ and $\chi = 0$ is even, being given by

$$F_0 = \left[1 + \frac{3a^2}{2} \right]^{-1/2}. \quad (4.7)$$

When $a = 0$, the eigenvalues are $\chi_{c;n}^2 = \chi_{s;n}^2 = n^2$, while the eigenmodes are given through

$$F_n(\theta) = \sqrt{2} \cos(n\theta), \quad G_n(\theta) = \sqrt{2} \sin(n\theta), \quad (4.8)$$

as was the case in Subsec. 3. When $a = 1$, the eigenvalues are derived in Eq. (SM:3.20) and are reproduced below, for convenience

$$\chi_{c;n} = \sqrt{n(n+3)}, \quad \chi_{s;n} = \sqrt{\left(n + \frac{5}{2}\right)\left(n - \frac{1}{2}\right)}. \quad (4.9)$$

The eigenfunctions and the detailed procedure used to obtain them are given in Sec. SM:3.2.2 of the supplementary material.

When $0 < a < 1$, the eigenmodes can be obtained as power series with respect to a , as detailed in Appendix B. The eigenfunctions F_n and G_n are depicted graphically in figure 7 for $a = 0.4$ and $1 \leq n \leq 4$. The eigenvalues χ_n^2 can be obtained following the same perturbative procedure as described in the previous section. As in the inviscid case, the difference between the eigenvalues corresponding to the n 'th odd and even modes appear at $O(a^{2n})$, as further discussed in Appendix B. The dependence of $\chi_{*,n}$ ($* \in \{c, s\}$, $1 \leq n \leq 3$) on a is shown in figure 8, obtained using high precision numerical integration. It can be seen that all eigenvalues exhibit a monotonic increase with respect to a and the eigenvalues $\chi_{c;n}$ corresponding to the even modes become significantly larger than those corresponding to the odd modes as $a \rightarrow 1$, as indicated in Eq. (4.9). The dotted lines correspond to the perturbative approximations up to $O(a^9)$. This behaviour is contrary to that of the eigenvalues seen in the inviscid case, shown in figure 2. In the inviscid case, the eigenvalues corresponding to the odd modes, $\lambda_{s;n}$, are generally larger than those corresponding to the even modes. Moreover, $\lambda_{c;n}$ has a non-monotonic behaviour, increasing with a at small a (for $n > 1$) and decreasing as $a \rightarrow 1$.

Combining the solutions for the time and angular dependences, the general solution

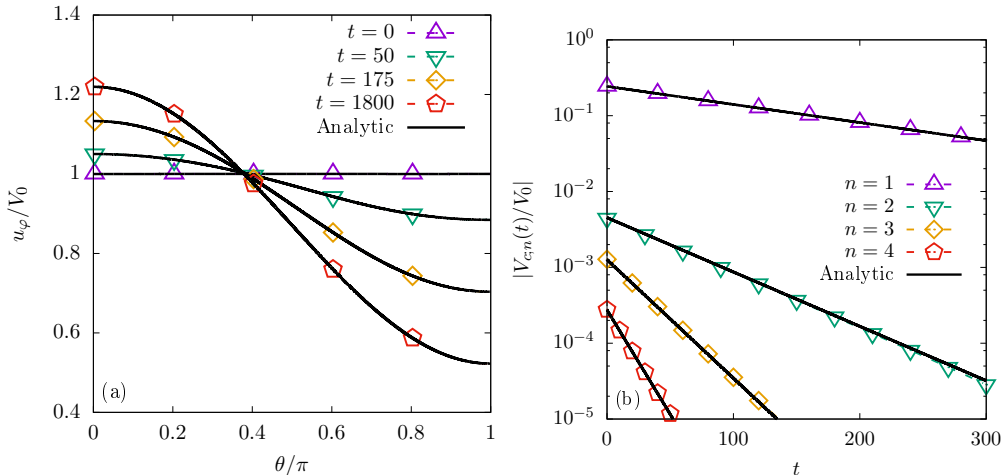


Figure 9. (a) Time evolution of the ratio $u^{\hat{\varphi}}/V_0$ of the azimuthal velocity $u^{\hat{\varphi}}$ initialised according to Eq. (4.12), where V_0 is the initial amplitude. (b) Time evolution of the amplitudes $V_{c;n}(t)$ ($1 \leq n \leq 4$). The numerical results are shown with dotted lines and points, while the analytic prediction is summing only the terms with $0 \leq n \leq 4$ in Eq. (4.10). The torus radii ratio is $a = 0.4$.

can be written as

$$u^{\hat{\varphi}}(t, \theta) = (1 + a \cos \theta) \sum_{n=0}^{\infty} [V_{c;n}(t)F_n(\theta) + V_{s;n}(t)G_n(\theta)],$$

$$V_{c;n}(t) = V_{c;n;0}e^{-\nu\chi_{c;n}^2 t/r^2}, \quad V_{s;n}(t) = V_{s;n;0}e^{-\nu\chi_{s;n}^2 t/r^2}. \quad (4.10)$$

The amplitudes $V_{c;n;0}$ and $V_{s;n;0}$ can be computed by integrating over the velocity profile at initial time, $u_0^{\hat{\varphi}}(\theta) \equiv u^{\hat{\varphi}}(0, \theta)$:

$$\begin{pmatrix} V_{c;n;0} \\ V_{s;n;0} \end{pmatrix} = \int_0^{2\pi} \frac{d\theta}{2\pi} (1 + a \cos \theta)^2 u_0^{\hat{\varphi}}(\theta) \begin{pmatrix} F_n(\theta) \\ G_n(\theta) \end{pmatrix}. \quad (4.11)$$

4.2. First benchmark: Constant initial flow

To verify the analytical theory developed in this section and to allow comparisons against our numerical solutions, we consider a specific example where the fluid on the torus has an initially constant velocity profile

$$u_0^{\hat{\varphi}}(\theta) = V_0. \quad (4.12)$$

In this case, it can be seen that the odd coefficients $V_{s;n;0}$ vanish, while the even coefficients can be computed as follows:

$$\begin{aligned} V_{c;n;0} &= V_0 \int_0^{2\pi} \frac{d\theta}{2\pi} (1 + a \cos \theta)^2 F_n(\theta) \\ &= V_0 \left[\frac{6}{(2 + \chi_{c;n}^2)^2} - \frac{1 - a^2}{2 + \chi_{c;n}^2} \right] \mathcal{I}_{c;n}. \end{aligned} \quad (4.13)$$

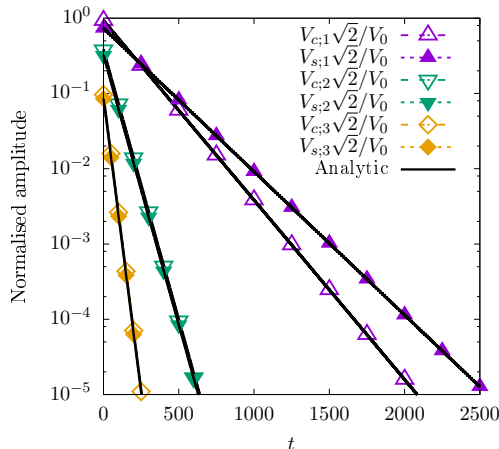


Figure 10. Time evolution of the amplitudes $V_{c;n}(t)$ (dashed lines and empty symbols) and $V_{s;n}(t)$ (dotted lines and filled symbols) for $n = 1$ (upper purple triangles), 2 (lower green triangles) and 3 (orange rhombi) on the torus with $a = 0.4$. The analytic prediction, Eq. (4.17), is shown with solid lines.

The second line in Eq. (4.13) is obtained by multiplying the first line in Eq. (4.5) with $(1 + a \cos \theta)^2/2\pi$ and integrating with respect to θ . For convenience, we also introduced

$$\mathcal{I}_{c;n} = \int_0^{2\pi} \frac{d\theta}{2\pi} F_n(\theta), \quad \mathcal{I}_{s;n} = \int_0^{2\pi} \frac{d\theta}{2\pi} \sin \theta G_n(\theta). \quad (4.14)$$

The result for $n = 0$ is exact: $\mathcal{I}_{c;0} = (1 + 3a^2/2)^{-1/2}$ and $V_{c;0;0} = V_0(1 + a^2/2)/\sqrt{1 + 3a^2/2}$. For $1 \leq n \leq 4$, the power series approximations of the $\mathcal{I}_{c;n}$ integrals can be found in Eq. (SM:3.4) of the supplementary material.

Figure 9(a) shows the numerical solution (dotted lines and points) and the analytic results obtained above (solid lines) for the fluid velocity in the azimuthal direction at four different values of the time coordinate. The agreement is excellent. We used an ideal, isothermal fluid with initial constant density $\rho_0 = 1$ and constant temperature $T_0 = 1$, on a grid with $N_\theta = 320$ equidistant points and a time step of $\delta t = 5 \times 10^{-3}$. The reference speed is taken as $c_0 = \sqrt{P_0/\rho_0}$, where $P_0 = \rho_0 k_B T_0/m$ is the reference pressure and m is the particle mass. The kinematic viscosity is taken to be $\nu = 2.5 \times 10^{-3}$ with respect to the reference value $\nu_0 = c_0 L_0$, where $L_0 = R/2$ is the reference length. With this convention, the non-dimensional torus parameters are $R = 2$ and $r = 0.8$, while the initial velocity amplitude in Eq. (4.12) is $V_0 = 10^{-5}$. Since the damping in Eq. (4.3) depends only on the fluid viscosity, the same results can be obtained when considering the thermal or the Cahn-Hilliard non-ideal fluids.

The amplitudes of the harmonics are extracted from the numerical solution by means of the orthogonality relation, Eq. (4.6), using the expansions of $F_n(\theta)$ given in Eq. (SM:3.4) of the supplementary material. The analytic solution is that in Eq. (4.10), with $V_{s;n;0} = 0$ and $V_{c;n;0}$ given in Eq. (4.13). The eigenvalues $\chi_{c;n}$ controlling the damping of the amplitude $V_{c;n}(t)$, as well as the integrals $\mathcal{I}_{c;n}$ ($1 \leq n \leq 4$) required to compute the initial amplitudes $V_{c;n;0}$ via Eq. (4.13), are constructed using the mode expansions also found in Eq. (SM:3.4) of the supplementary material.

4.3. Second benchmark test: Even and odd harmonics

In this second benchmark test, we aim to highlight the difference between the rates of decay for the even and odd harmonics corresponding to the same order n . To this end, we consider initial conditions which are neither even nor odd, defined as a combination of harmonic functions

$$u_0^{\hat{\varphi}}(\theta) = \frac{V_0}{(1 + a \cos \theta)^2 \sqrt{2}} (\cos \theta + \sin \theta), \quad (4.15)$$

where the overall $(1 + a \cos \theta)^{-2}$ was added to inhibit the development of the $n = 0$ harmonic. The initial amplitudes for the modes $V_{c;n}(t)$ and $V_{s;n}(t)$ are

$$V_{c;n;0} = -\frac{V_0 \chi_{c;n}^2}{a \sqrt{2} (2 + \chi_{c;n}^2)} \mathcal{I}_{c;n}, \quad V_{s;n;0} = \frac{V_0}{\sqrt{2}} \mathcal{I}_{s;n}, \quad (4.16)$$

where the notation $\mathcal{I}_{*;n}$ ($* \in \{c, s\}$) was introduced in Eq. (4.14). The amplitudes $V_{c;n}(t)$ and $V_{s;n}(t)$ undergo exponential damping with their respective damping coefficients, $\nu \chi_{c;n}^2 / r^2$ and $\nu \chi_{s;n}^2 / r^2$, respectively. The general solution can be written as

$$u^{\hat{\varphi}}(t, \theta) = \frac{V_0}{\sqrt{2}} (1 + a \cos \theta) \sum_{n=1}^{\infty} \left[-\frac{\chi_{c;n}^2}{a(2 + \chi_{c;n}^2)} \mathcal{I}_{c;n} e^{-\nu \chi_{c;n}^2 t / r^2} F_n(\theta) + \mathcal{I}_{s;n} e^{-\nu \chi_{s;n}^2 t / r^2} G_n(\theta) \right]. \quad (4.17)$$

Figure 10 shows the time dependence of the amplitudes $V_{c;n}(t)$ (dashed lines and empty symbols) and $V_{s;n}(t)$ (dotted lines and filled symbols) for $n = 1$ (purple upper triangles), 2 (green lower triangles) and 3 (orange rhombi). As expected from figure 8, $V_{c;1}(t)$ decays at a faster rate than $V_{s;1}(t)$. However, at $a = 0.4$, the eigenvalues $\chi_{c;n}$ and $\chi_{s;n}$ have roughly the same values when $n \geq 2$. Therefore, the decay rates of $V_{c;2}(t)$ and $V_{c;3}(t)$ are very similar to those of $V_{s;2}(t)$ and $V_{s;3}(t)$, respectively. In this benchmark test, the fluid and simulation parameters are the same as those employed in Subsec. 4.2.

5. Viscous fluid: sound wave damping

In the previous sections, we considered the propagation of sound waves in the perfect fluid and the equivalent of shear wave damping in a viscous fluid. This section presents an analysis of the damping of longitudinal waves propagating along the poloidal direction through a viscous fluid. For simplicity, we assume that the fluid velocity along the azimuthal direction vanishes.

This section is structured as follows. The general solution for the damping of longitudinal waves propagating along the poloidal direction is presented in Subsec. 5.1. Then, a benchmark test is proposed in Subsec. 5.2.

5.1. General solution

The starting point of the analysis in this section is the Cauchy equation in the poloidal direction, [Eq. (2.41b)], which can be linearised as follows:

$$\begin{aligned} \frac{\partial u^{\hat{\theta}}}{\partial t} + \frac{P_0}{\rho_0 r} \frac{\partial \delta P}{\partial \theta} &= \frac{\kappa \phi_0}{\rho_0 r^3} \frac{\partial}{\partial \theta} \left\{ \frac{\partial_{\theta} [(1 + a \cos \theta) \partial_{\theta} \delta \phi]}{1 + a \cos \theta} \right\} \\ + \frac{\nu}{r^2 (1 + a \cos \theta)^2} \frac{\partial}{\partial \theta} &\left[(1 + a \cos \theta)^3 \frac{\partial}{\partial \theta} \left(\frac{u^{\hat{\theta}}}{1 + a \cos \theta} \right) \right] + \frac{\nu_v}{r^2} \frac{\partial}{\partial \theta} \left\{ \frac{\partial_{\theta} [u^{\hat{\theta}} (1 + a \cos \theta)]}{1 + a \cos \theta} \right\}. \end{aligned} \quad (5.1)$$

The left hand side of the above equation is similar to that encountered in the inviscid case, in Eq. (3.4). On the right hand side, one can see that the differential operator with respect to θ acting on $(1 + a \cos \theta) \partial_{\theta} \delta \phi$ and in the term proportional to ν_v is the one encountered in the inviscid case, defined in Eq. (3.10). In the term proportional to ν , one can recognise the operator encountered in the damping of the shear wave problem, presented in Eq. (4.4). In principle, the normal modes analysis must be made with respect to the complete set of eigenfunctions and eigenvalues of only one operator. The set of eigenfunctions $\{f_n, g_n\}$ of the inviscid operator differs in general from the set $\{F_n, G_n\}$ corresponding to the viscous operator (they coincide only in the limit when $a \rightarrow 0$). Since the dominant phenomenon in the present setup is the wave propagation, it is natural to work with the basis given by the inviscid operator and to treat the viscous operator as a perturbative effect. To this end, we take advantage of the identity

$$\begin{aligned} \frac{1}{(1 + a \cos \theta)^2} \frac{\partial}{\partial \theta} \left[(1 + a \cos \theta)^3 \frac{\partial}{\partial \theta} \left(\frac{u^{\hat{\theta}}}{1 + a \cos \theta} \right) \right] \\ = \frac{\partial}{\partial \theta} \left\{ \frac{\partial_{\theta} [u^{\hat{\theta}} (1 + a \cos \theta)]}{1 + a \cos \theta} \right\} + \frac{2a \cos \theta}{1 + a \cos \theta} u^{\hat{\theta}}, \end{aligned} \quad (5.2)$$

which allows Eq. (5.1) to be written as

$$\begin{aligned} \frac{\partial u^{\hat{\theta}}}{\partial t} + \frac{P_0}{\rho_0 r} \partial_{\theta} \delta P &= \frac{\kappa \phi_0}{\rho_0 r^3} \frac{\partial}{\partial \theta} \left\{ \frac{\partial_{\theta} [(1 + a \cos \theta) \partial_{\theta} \delta \phi]}{1 + a \cos \theta} \right\} \\ + \frac{\nu + \nu_v}{r^2} \partial_{\theta} &\left\{ \frac{\partial_{\theta} [u^{\hat{\theta}} (1 + a \cos \theta)]}{1 + a \cos \theta} \right\} + \frac{\nu}{r^2} \frac{2a \cos \theta}{1 + a \cos \theta} u^{\hat{\theta}}. \end{aligned} \quad (5.3)$$

In principle, as was the case for the inviscid fluid, the sound wave equation can be obtained by taking the time derivative of Eq. (5.3). However, this approach is not insightful. Instead, starting from Eq. (3.2), the time derivative of the pressure deviation can be replaced using the continuity, energy and Cahn-Hilliard equations, reproduced below in the linearised limit

$$\begin{aligned} \frac{\partial \delta \rho}{\partial t} + \frac{\partial_{\theta} \mathcal{U}}{r(1 + a \cos \theta)} &= 0, \\ \frac{\partial \delta e}{\partial t} + \frac{P_0}{\rho_0 e_0} \frac{\partial_{\theta} \mathcal{U}}{r(1 + a \cos \theta)} &= \frac{k_0}{\rho_0 c_v} \frac{\partial_{\theta} [(1 + a \cos \theta) \partial_{\theta} \delta e]}{r^2 (1 + a \cos \theta)}, \\ \frac{\partial \delta \phi}{\partial t} + \phi_0 \frac{\partial_{\theta} \mathcal{U}}{r(1 + a \cos \theta)} &= \frac{M}{r^2} \frac{\partial_{\theta} [(1 + a \cos \theta) \partial_{\theta} \delta \mu]}{1 + a \cos \theta}. \end{aligned} \quad (5.4)$$

We remind the readers that we consider small perturbations around a stationary, back-

ground state, which we denote by the subscript 0. We also introduced the notation $\mathcal{U} = u^{\hat{\theta}}(1 + a \cos \theta)$ and the deviation of the chemical potential from the background state $\delta\mu = \mu(\phi) - \mu(\phi_0)$ is given by

$$\delta\mu = -A(1 - 3\phi_0^2)\delta\phi - \frac{\kappa}{r^2} \frac{\partial_{\theta}[(1 + a \cos \theta)\partial_{\theta}\delta\phi]}{1 + a \cos \theta}. \quad (5.5)$$

To solve the partial differential equations in Eq. (5.4), we seek normal solutions defined with respect to the complete set of modes $\{f_n, g_n\}$ introduced in Sec. 3. We introduce the following expansions:

$$\begin{pmatrix} u^{\hat{\theta}} & \partial_{\theta}\delta\rho & \partial_{\theta}\delta e \\ \partial_{\theta}\delta\phi & \partial_{\theta}\delta\mu & \partial_{\theta}\delta P \end{pmatrix} = \sum_{n=0}^{\infty} \frac{f_n(\theta)}{1 + a \cos \theta} \begin{pmatrix} U_{c;n} & R_{c;n} & E_{c;n} \\ \Phi_{c;n} & M_{c;n} & P_{c;n} \end{pmatrix}, \quad (5.6)$$

where for simplicity we assume that the flow parameters are even with respect to θ , such that the coefficients of the odd eigenfunctions $g_n(\theta)$ vanish. The amplitudes $\mathcal{A}_{c;n}(t)$ ($\mathcal{A} \in \{U, R, E, \Phi, M, P\}$) have the following time dependence:

$$\mathcal{A}_{c;n}(t) = \mathcal{A}_{c;n;0} e^{-\alpha_{c;n} t}. \quad (5.7)$$

The real part of $\alpha_{c;n}$ controls the damping of the corresponding mode, while its imaginary part is responsible for its propagation. The extension to the case of odd or general flow configurations is straightforward, but will not be discussed here for brevity.

In order to find the normal frequencies $\alpha_{c;n}$, we multiply Eq. (5.3) by $f_n(\theta)$ and integrate it with respect to θ between 0 and 2π . We obtain

$$-\alpha_{c;n} U_{c;n;0} + \frac{P_0}{\rho_0 r} P_{c;n;0} = -\frac{\kappa\phi_0\lambda_{c;n}^2}{\rho_0 r^3} \Phi_{c;n;0} - \frac{\nu + \nu_v}{r^2} \lambda_{c;n}^2 U_{c;n;0} - \frac{2\nu}{r^2} \sum_{\ell=0}^{\infty} \mathbf{M}_{n,\ell} U_{c;\ell;0}, \quad (5.8)$$

where $\lambda_{c;n}^2$ is defined in Eq. (3.15). The infinite matrix \mathbf{M} mixes the normal modes due to the last term in Eq. (5.3). Its components can be obtained as

$$\begin{aligned} \mathbf{M}_{n,\ell} &= - \int \frac{d\theta}{2\pi} \frac{a \cos \theta}{(1 + a \cos \theta)^2} f_n(\theta) f_{\ell}(\theta) \\ &= \int \frac{d\theta}{2\pi} \left[\frac{1}{(1 + a \cos \theta)^2} - \frac{1}{1 + a \cos \theta} \right] f_n(\theta) f_{\ell}(\theta). \end{aligned} \quad (5.9)$$

In the case $n = \ell = 0$, we find an analytic result

$$\mathbf{M}_{0,0} = \frac{a^2}{1 - a^2}. \quad (5.10)$$

When $\ell = 0$ and $n > 0$, the second term in the square brackets in Eq. (5.9) does not contribute due to the orthogonality relation given in Eq. (3.11). Comparing the first term with the definition of $I_{m;n}$ in Eq. (3.26) for $m = 2$ and noting that $f_0(\theta) = (1 - a^2)^{1/4}$ is a constant, $\mathbf{M}_{n,0}$ can be written as:

$$\mathbf{M}_{n,0} = (1 - a^2)^{1/4} I_{c;2;n} - \delta_{n,0}. \quad (5.11)$$

The integral $I_{c;2;n}$ ($n > 0$) can be obtained in terms of $I_{c;0;n}$ by integrating Eq. (3.15) with respect to θ and using integration by parts

$$\begin{aligned} I_{c;0;n} &= - \frac{1}{\lambda_{c;n}^2} \int_0^{2\pi} \frac{d\theta}{2\pi} (1 + a \cos \theta) \frac{d}{d\theta} \left(\frac{df_n/d\theta}{1 + a \cos \theta} \right) \\ &= \frac{1}{\lambda_{c;n}^2} \int_0^{2\pi} \frac{d\theta}{2\pi} f_n(\theta) \left[\frac{1}{1 + a \cos \theta} - \frac{1 - a^2}{(1 + a \cos \theta)^2} \right]. \end{aligned} \quad (5.12)$$

The first term in the square brackets on the last line of the above equation vanishes for $n > 0$. Setting $m = 2$ in Eq. (3.26), it can be seen that the second term can be expressed in terms of $I_{c;2;n}$, such that the following relation can be established:

$$I_{c;2;n} = -\frac{\lambda_{c;n}^2}{1-a^2} I_{c;0;n}. \quad (5.13)$$

Putting together Eqs. (5.10), (5.11) and (5.13) allows $M_{n,0}$ to be expressed in the following form:

$$M_{n,0} = \frac{\delta_{n,0} a^2}{1-a^2} - \frac{\lambda_{c;n}^2}{(1-a^2)^{3/4}} I_{0;n}, \quad (5.14)$$

which is also valid at $n = 0$ since the second term does not contribute due to the fact that $\lambda_{c;0} = 0$. Later in this section, the diagonal elements $M_{n,n}$ with $1 \leq n \leq 3$, will be necessary for the computation of the acoustic damping coefficient. Their analytic approximations up to $O(a^9)$ are given in Eq. (SM:3.3*i*) of the supplementary material.

The next step is to find expressions for the quantities $P_{c;n;0}$ and $\Phi_{c;n;0}$ in Eq. (5.8). To this end, we insert the decompositions in Eq. (5.6) into Eq. (5.4) and find

$$\begin{aligned} R_{c;n;0} &= -\frac{\lambda_{c;n}^2}{\alpha_{c;n} r} U_{c;n;0}, \\ E_{c;n;0} &= -\frac{P_0}{\rho_0 e_0} \frac{\lambda_{c;n}^2}{\alpha_{c;n} r} \frac{U_{c;n;0}}{\tilde{E}_{c;n;0}}, \\ M_{c;n;0} &= \left[\frac{\lambda_{c;n}^2 \kappa}{r^2} - A(1-3\phi_0^2) \right] \Phi_{c;n;0}, \\ \Phi_{c;n;0} &= -\phi_0 \frac{\lambda_{c;n}^2}{\alpha_{c;n} r} \frac{U_{c;n;0}}{\tilde{\Phi}_{c;n;0}}, \end{aligned} \quad (5.15)$$

where we introduced the following dimensionless quantities:

$$\tilde{E}_{c;n;0} = 1 - \frac{\gamma \nu \lambda_{c;n}^2}{P_{\Gamma} r^2 \alpha_{c;n}}, \quad \tilde{\Phi}_{c;n;0} = 1 + \frac{M \lambda_{c;n}^2}{r^2 \alpha_{c;n}} \left[A(1-3\phi_0^2) - \frac{\kappa \lambda_{c;n}^2}{r^2} \right]. \quad (5.16)$$

The pressure amplitude $P_{c;n;0}$ can be obtained by combining the above results in conjunction with Eq. (3.2) via:

$$\begin{aligned} P_{c;n;0} &= \frac{\rho_0 P_{\rho,0}}{P_0} R_{c;n;0} + \frac{e_0 P_{e,0}}{P_0} E_{c;n;0} + \frac{P_{\phi,0}}{P_0} \Phi_{c;n;0} \\ &= -\frac{\lambda_{c;n}^2 U_{c;n;0}}{\alpha_{c;n} r} \tilde{P}_{c;n;0}. \end{aligned} \quad (5.17)$$

The dimensionless quantity $\tilde{P}_{c;n;0}$ was introduced for notational brevity, being given by

$$\tilde{P}_{c;n;0} = \frac{\rho_0 P_{\rho,0}}{P_0} + \frac{P_{e,0}}{\rho_0 \tilde{E}_{c;n;0}} + \frac{\phi_0 P_{\phi,0}}{P_0 \tilde{\Phi}_{c;n;0}}. \quad (5.18)$$

Using the expression for $P_{c;n;0}$ given in Eq. (5.17), Eq. (5.8) can be rearranged as a matrix equation

$$\mathbf{A}\mathbf{U} = 0, \quad (5.19)$$

where the column vector \mathbf{U} has elements $U_n = U_{c;n;0}$, while the (infinite-dimensional)

matrix \mathbf{A} has the following components:

$$\mathbf{A}_{n,m} = -\frac{\delta_{n,m}}{\alpha_{c;n}} \left[\alpha_{c;n}^2 + \frac{\lambda_{c;n}^2 P_0}{r^2 \rho_0} \tilde{P}_{c;n;0} + \frac{\kappa \lambda_{c;n}^4 \phi_0^2}{\rho_0 r^4 \tilde{\mathcal{D}}_{c;n;0}} - \frac{\alpha_{c;n} \lambda_{c;n}^2}{r^2} (\nu + \nu_v) \right] + \frac{2\nu}{r^2} \mathbf{M}_{n,m}. \quad (5.20)$$

Eq. (5.19) has non-trivial solutions when the determinant of the matrix \mathbf{A} vanishes. This condition selects a discrete set of values for the coefficients $\alpha_{c;n}$. In order to find these values, we make the assumption that the dissipative terms are small on their respective dimensional scale, i.e.: $\nu, \nu_v \ll c_{s,0}/r$, $\kappa \ll r^2$, $M \ll rc_{s,0}$. To this end, we introduce the small parameter ε , which allows us to write:

$$\nu = \varepsilon \bar{\nu}, \quad \nu_v = \varepsilon \bar{\nu}_v, \quad \kappa = \varepsilon \bar{\kappa}, \quad M = \varepsilon \bar{M}. \quad (5.21)$$

We keep terms up to first order in ε for the rest of the section. We further assume that $\alpha_{c;n}$ can be written as

$$\alpha_{c;n} = \pm i \omega_{c;n} + \varepsilon \bar{\alpha}_{c;n;d}, \quad (5.22)$$

where $\omega_{c;n}$ is the angular velocity and $\alpha_{c;n;d} = \varepsilon \bar{\alpha}_{c;n;d}$ is the damping factor.

It can be seen that the off-diagonal elements of the matrix \mathbf{A} are at least one order higher with respect to ε than the diagonal elements, being proportional to $\varepsilon \bar{\nu}$. When computing the determinant, the leading order contribution comes from the diagonal elements, while any off-diagonal contribution comes with an $O(\varepsilon^2)$ penalty, such that

$$\det \mathbf{A} = \mathbf{A}_{11} \times \mathbf{A}_{22} \times \mathbf{A}_{33} \times \dots + O(\varepsilon^2). \quad (5.23)$$

Thus, up to first order in ε , the eigenvalues $\alpha_{c;n}$ can be found by requiring that each diagonal element \mathbf{A}_{nn} vanishes. We further note that there are typically multiple solutions stemming from $\mathbf{A}_{nn} = 0$. The acoustic modes correspond to complex solutions for $\alpha_{c;n}$, allowing the corresponding modes to propagate. There are also real solutions for $\alpha_{c;n}$, such that the respective modes decay exponentially. In the case of the ideal thermal fluid, there is only one such solution, corresponding to the thermal mode. There is also one such mode corresponding to the Cahn-Hilliard equation, which we will refer to as the Cahn-Hilliard mode. For simplicity, when we use the Cahn-Hilliard equation, we assume that the fluid is isothermal.

We now discuss the $n = 0$ mode, corresponding to the incompressible velocity profile. Since $\lambda_{c;0} = 0$, the case $n = 0$ is degenerate. There is only one eigenvalue corresponding to this case, which is given by

$$\alpha_{c;0} = \frac{2\nu}{R^2 - r^2}, \quad (5.24)$$

where the relation $\mathbf{M}_{0,0} = a^2/(1 - a^2) = r^2/(R^2 - r^2)$ was employed. There is no imaginary part to $\alpha_{c;0}$, showing that the mode corresponding to the incompressible velocity profile does not propagate. Furthermore, since $\alpha_{c;0} > 0$, the amplitude of this mode decays exponentially through viscous damping. On the flat geometry, the incompressible one-dimensional flow corresponds to a constant velocity, which cannot suffer viscous damping due to the Galilean invariance of the theory. In contrast, on the torus, Galilean invariance is no longer valid. While the inviscid fluid supports (in the linearised regime) the incompressible flow profile as an exact, time-independent solution, this zeroth-order mode with respect to the set $\{f_n, g_n\}$ is no longer preserved in the case of the viscous fluid, since $f_0(1 + a \cos \theta)$ does not provide an eigenfunction of the viscous operator in Eq. (4.4). The damping of the zeroth-order mode, given in Eq. (5.24), depends only on the kinematic viscosity and seems to be independent of the type of fluid

considered. Thus, $\alpha_{c;0}^{-1}$ provides a fundamental time scale on which, in the absence of external forcing, the flow on the poloidal direction becomes quiescent.

For $n > 0$, the angular frequency $\omega_{c;n}$ for the acoustic mode is given by

$$\omega_{c;n} = \frac{\lambda_{c;n} c_{s;\kappa;c;n}}{r}, \quad c_{s;\kappa;c;n}^2 = c_{s;0}^2 + \frac{\kappa \lambda_{c;n}^2}{\rho_0 r^2} \phi_0. \quad (5.25)$$

The acoustic damping coefficient $\alpha_{c;n;a} = \varepsilon \bar{\alpha}_{c;n;a}$ (as a shorthand, we remove the subscript d and add a subscript a to describe the acoustic damping coefficient) receives contributions from the viscous terms, as well as from the energy and Cahn-Hilliard terms

$$\alpha_{c;n;a} = \frac{\nu}{r^2} \mathbf{M}_{n,n} + \frac{\lambda_{c;n}^2}{2r^2} \left[\nu \left(1 + \frac{\gamma P_0 P_{e,0}}{\rho_0^2 c_{s;\kappa;c;n}^2 \text{Pr}} \right) + \nu_v - \frac{M \phi_0 P_{\phi,0}}{\rho_0 c_{s;\kappa;c;n}^2} \mathbf{A} (1 - 3\phi_0^2) \right]. \quad (5.26)$$

We remind the reader that $\alpha_{c;n;a}$ together with the angular frequency $\omega_{c;n}$ make up the acoustic mode, $\alpha_{c;n} \rightarrow \alpha_{c;n;a} \pm i\omega_{c;n}$. We note that Eqs. (5.25) and (5.26) are valid for all types of fluids considered in this paper, namely: the ideal isothermal fluid, the ideal thermal fluid and the isothermal fluid coupled with the Cahn-Hilliard equation.

The thermal and Cahn-Hilliard modes can be obtained by setting, in Eq. (5.20), $\alpha_{c;n}$ to $\varepsilon \bar{\alpha}_{c;n;t}$ or $\varepsilon \bar{\alpha}_{c;n;\phi}$, respectively, while setting the angular frequency $\omega_{c;n} = 0$. The values of $\alpha_{c;n}$ satisfying the above ansatz are found by solving the following equation:

$$\tilde{P}_{c;n;0} = 0, \quad (5.27)$$

which is quadratic in $\alpha_{c;n}$. In the general case of the thermal flow of a non-ideal (Cahn-Hilliard) fluid, the solution of this equation is too lengthy to be reproduced here. In the next section we will specialise the equation to the fluid types introduced in Sec. 3, namely an ideal isothermal fluid, an ideal fluid with variable temperature and an isothermal multicomponent fluid coupled with the Cahn-Hilliard equation, allowing for simple expressions to be obtained. These solutions are presented in Eqs. (5.36), (5.37) and (5.37), respectively.

5.2. Benchmark test

We now focus on a specific example. At initial time, $t = 0$, we assume that the density, internal energy and order parameter fields are unperturbed, while the velocity profile is that of the incompressible fluid

$$\delta\rho_0 = 0, \quad \delta e_0 = 0, \quad \delta\phi_0 = 0, \quad u_0^\theta = \frac{U_0}{1 + a \cos\theta}. \quad (5.28)$$

The analysis of the normal modes was performed in the limit where the modes become fully decoupled (the non-diagonal elements of the matrix \mathbf{M} were ignored). For the particular case considered here, we are also interested in finding the time dependence of the amplitudes $U_{c;n}(t)$, defined through Eq. (5.6). To do this, it is sufficient to employ the initial conditions in Eq. (5.28) in order to find the full solution. From Eq. (5.28) and (5.3), it can be seen that

$$U_{c;n}(0) = \frac{U_0 \delta_{n,0}}{(1 - a^2)^{1/4}}, \quad \dot{U}_{c;n}(0) = -\frac{2\nu U_0}{r^2 (1 - a^2)^{1/4}} \mathbf{M}_{n,0}. \quad (5.29)$$

The time dependence of the amplitude of the $n = 0$ mode is

$$U_{c;0}(t) = \frac{U_0}{(1 - a^2)^{1/4}} e^{-2\alpha_\nu t}, \quad \alpha_\nu \equiv \frac{1}{2} \alpha_{c;0} = \frac{\nu}{R^2 - r^2}, \quad (5.30)$$

where α_ν is the principal damping coefficient which will be fundamental for discussing the dynamics of the stripe configurations in Sec. 7.

For the higher-order harmonics, and when the temperature or Cahn-Hilliard equation is taken into account, a third equation is required to fix the integration constant for the thermal or Cahn-Hilliard mode. This can be obtained by taking the time derivative of Eq. (5.3), yielding

$$\ddot{U}_{c;n} + \frac{P_0}{\rho_0 r} \dot{P}_{c;n} + \frac{\kappa \lambda_{c;n}^2 \phi_0}{r^3} \dot{\Phi}_{c;n} + \frac{\nu + \nu_v}{r^2} \lambda_{c;n}^2 \dot{U}_{c;n} + \frac{2\nu}{r^2} \sum_{m=0}^{\infty} M_{n,m} \dot{U}_{c;m} = 0. \quad (5.31)$$

The time derivative $\dot{P}_{c;n}$ can be obtained in analogy to Eq. (5.17), by differentiating Eq. (3.2) with respect to θ and t , multiplying it by $f_n(\theta)$ and then integrating it with respect to θ :

$$\dot{P}_{c;n} = \frac{\rho_0 P_{\rho,0}}{P_0} \dot{R}_{c;n} + \frac{e_0 P_{e,0}}{P_0} \dot{E}_{c;n} + \frac{P_{\phi,0}}{P_0} \dot{\Phi}_{c;n}. \quad (5.32)$$

The time derivatives $\dot{R}_{c;n}$, $\dot{E}_{c;n}$ and $\dot{\Phi}_{c;n}$ can be obtained by differentiating all three relations in Eq. (5.4) with respect to θ , multiplying them by $f_n(\theta)$ and integrating them with respect to θ . Noting that, at initial time, the perturbations δe , $\delta \rho$ and $\delta \phi$ vanish, the right hand sides of the relations in Eq. (5.4) cancel, such that the following results are obtained:

$$\begin{pmatrix} \dot{R}_{c;n}(0) \\ \dot{E}_{c;n}(0) \\ \dot{\Phi}_{c;n}(0) \end{pmatrix} = \frac{\lambda_{c;n}^2}{r} \frac{\delta_{n,0} U_0}{(1-a^2)^{1/4}} \begin{pmatrix} 1 \\ P_0/\rho_0 e_0 \\ \phi_0 \end{pmatrix} = \begin{pmatrix} 0 \\ 0 \\ 0 \end{pmatrix}. \quad (5.33)$$

The latter equality follows after taking into account that $\lambda_{c;0} = 0$. Substituting the above results in Eq. (5.32), it can be seen that $\dot{P}_{c;n}(0) = 0$. Since $\dot{\Phi}_{c;n}(0)$ also cancels by virtue of Eq. (5.33), the second and third terms in Eq. (5.31) can be dropped.

The fourth and fifth terms in (5.31) are of second order with respect to the damping coefficients ν and ν_v , and thus of order $O(\varepsilon^2)$ in the language of Eq. (5.21). For consistency, we approximate $\dot{U}_{c;n}(0) = O(\varepsilon^2) \simeq 0$. Thus, the solution which is accurate to first order in ε is

$$U_{c;n}(t) = \frac{2\nu U_0 \lambda_{c;n}^2}{\omega_{c;n} r^2} \frac{I_{c;0;n}}{1-a^2} \sin(\omega_{c;n} t) e^{-\alpha_{c;n;a} t}, \quad \forall n > 0. \quad (5.34)$$

The above solution was obtained under general considerations and therefore it applies to all types of fluids studied in this paper. The full solution can be constructed via the expansion in Eq. (5.6):

$$u^{\hat{\theta}}(t, \theta) = \frac{1}{1+a \cos \theta} \sum_{n=0}^{\infty} U_{c;n}(t) f_n(\theta). \quad (5.35)$$

Below we give a set of tests for the ideal isothermal fluid, the ideal fluid with variable temperature and the isothermal multicomponent fluid. The initial velocity amplitude is set to $U_0 = 10^{-5}$.

For the isothermal ideal fluid, Eqs. (5.25) and (5.26) reduce to:

$$\begin{aligned} c_{s,\kappa;c;n}^2 &= c_{s,0}^2 = \frac{k_B T_0}{m}, \\ \alpha_{c;n;a} &= \frac{\nu}{r^2} M_{n,n} + \frac{\lambda_{c;n}^2 (\nu + \nu_v)}{2r^2}. \end{aligned} \quad (5.36)$$

We set the background density and temperature to $\rho_0 = 1$ and $T_0 = 1$, respectively, and

	T	$\nu[\times 10^{-3}]$	$\alpha_\nu[\times 10^{-3}]$
Iso	1	10	2.976
Th	0.5	4	1.190
CH	0.4112	6.486	1.930

Table 4. Values for the background temperature T , kinematic viscosity ν and principal damping coefficient α_ν defined in Eq. (5.30), for the isothermal ideal fluid (Iso), variable temperature ideal fluid (Th) and isothermal multicomponent fluid (CH) on the torus with $a = 0.4$. The background density is in all cases $\rho = 1$. The heat conductivity and adiabatic index for the thermal model are $k = 0.012$ and $\gamma = 2$, corresponding to $\text{Pr} = 2/3$. The parameters for the multicomponent fluid are $M = \nu \simeq 6.486 \times 10^{-3}$, $A = 1$ and $\kappa = 5 \times 10^{-4}$. The parameters are chosen such that $c_s^2 = 1$.

n	$I_{c;0;n}$	$M_{n;n}[\times 10^{-2}]$	$U_{c;n;0;a}/U_0[\times 10^{-3}]$	$\alpha_{c;n;a}(\nu_v = 0)$	$\alpha_{c;n;a}(\nu_v = 0.02)$
1	0.2883	6.015	8.158	8.64×10^{-3}	0.02404
2	-0.01949	8.261	-1.163	3.27×10^{-2}	0.09554
3	2.156×10^{-3}	8.808	0.1926	0.2128	0.2128

Table 5. Values of various parameters required to build the solution in Eq. (5.34) when $a = 0.4$. The bulk kinematic viscosity ν_v required to compute the coefficient $\alpha_{c;n;a}$ in the last column is set to $\nu_v = 0.02$. The amplitudes are computed by dividing the prefactors in Eq. (5.34) by the initial velocity amplitude $U_0 = 10^{-5}$.

take units such that $c_{s,0} = 1$. The kinematic viscosity is set to $\nu = 0.01$ and we consider two test cases, corresponding to $\nu_v = 0$ and 0.02 .

In the case of the variable temperature ideal fluid, Eqs. (5.25) and (5.26) reduce to:

$$\begin{aligned}
 c_{s,\kappa;c;n}^2 &= c_{s,0}^2 = \frac{\gamma K_B T_0}{m}, \\
 \alpha_{c;n;a} &= \frac{\nu}{r^2} M_{n,n} + \frac{\lambda_{c;n}^2}{2r^2} \left[\nu \left(1 + \frac{\gamma - 1}{\text{Pr}} \right) + \nu_v \right], \\
 \alpha_{c;n;t} &= \frac{\lambda_{c;n}^2 \nu}{r^2 \text{Pr}}.
 \end{aligned} \tag{5.37}$$

We consider the case when $c_v = k_B/m$, such that $\gamma = 2$. In order to match the sound speed of the isothermal fluid ($c_{s,0} = 1$), the background temperature is set to $T_0 = 0.5$. The background density is also kept at $\rho_0 = 1$. We further consider the case when the Prandtl number is $\text{Pr} = 2/3$, such that $k_0 = 3\nu$. In order to ensure that $\alpha_{c;n;a}$ matches the value corresponding to the isothermal case, the kinematic viscosity is set to $\nu = 0.004$, such that $k_0 = 0.012$. As before, we consider two values for the bulk kinematic viscosity, namely $\nu_v = 0$ and 0.02 .

In the case of the isothermal multicomponent fluid, Eqs. (5.25) and (5.26) reduce to:

$$\begin{aligned} c_{s,\kappa;c;n}^2 &= c_s^2 + \frac{\kappa\lambda_{c;n}^2}{\rho_0 r^2} \phi_0^2 = \frac{k_B T_0}{m} - \frac{\phi_0^2}{\rho_0} \left[A(1 - 3\phi_0^2) - \frac{\kappa\lambda_{c;n}^2}{r^2} \right], \\ \alpha_{c;n;a} &= \frac{\nu}{r^2} \mathbf{M}_{n,n} + \frac{\lambda_{c;n}^2}{2r^2} \left[\nu + \nu_v + \frac{MA^2}{\rho_0 c_{s,\kappa;c;n}^2} \phi_0^2 (1 - 3\phi_0^2)^2 \right], \\ \alpha_{c;n;\phi} &= \frac{MP_{\rho,0} \lambda_{c;n}^2}{r^2 c_{s,0}^2} A(3\phi_0^2 - 1) = \frac{M\lambda_{c;n}^2}{r^2} \frac{k_B T_0}{m c_{s,0}^2} A(3\phi_0^2 - 1). \end{aligned} \quad (5.38)$$

It can be seen that within the spinodal region, where $-\frac{1}{\sqrt{3}} < \phi_0 < \frac{1}{\sqrt{3}}$, $\alpha_{c;n;\phi} < 0$ and spontaneous domain decomposition can occur through an exponential growth of fluctuations. We thus conduct the simulations outside this region, namely for the background value $\phi_0 = 0.8$ of the order parameter. Keeping the density at $\rho_0 = 1$, the interaction strength $A = 1$ and the surface tension parameter $\kappa = 5 \times 10^{-4}$, the temperature required to match the isothermal sound speed $c_{s,\kappa;c;n} = 1$ is $T_0 \simeq 0.4112$ (this is true only for the zeroth-order mode, when $\lambda_{c;0} = 0$). We consider the case when the mobility parameter M is equal to the kinematic viscosity. In order to obtain the same acoustic damping coefficients as in the isothermal case, we set $M = \nu \simeq 6.486 \times 10^{-3}$. As before, ν_v takes the values 0 and 0.02.

The parameter values discussed above are also summarised in table 4. The other quantities required to compute the solutions $U_{c;n}$ (for $n > 0$), given in Eq. (5.34), are summarised in table 5.

We now discuss the benchmark test results. In figure 11, we validate the analytic solution using numerical simulations for the 2×3 cases discussed above. The simulations were conducted using $N_\theta = 320$ nodes and a time step $\delta t = 5 \times 10^{-4}$ on the torus with $a = 0.4$. The amplitude of the $n = 0$ mode is shown in figure 11(a). As predicted by Eq. (5.30), the damping coefficient $2\alpha_\nu$ of $U_{c;0}$ depends only on the kinematic viscosity. This is natural since the bulk viscosity cannot affect the mode corresponding to the incompressible velocity profile. Thus, the results for $\nu_v = 0$ and $\nu_v = 0.02$ are overlapped and only three distinct curves can be seen in figure 11(a), corresponding to the differing values of the background kinematic viscosity ν employed in the three fluids discussed above (these values are summarised in table 4). The careful choice of parameters discussed above and summarised in table 4 ensures that the acoustic damping coefficients $\alpha_{c;n;a}$ corresponding to the higher-order modes have the same values. Thus, only two distinct curves can be seen in figures 11(b)–11(d), corresponding to $\nu_v = 0$ (lesser damping, shown with dashed black lines and empty symbols) and to $\nu_v = 0.02$ (stronger damping, shown with dotted red lines and filled symbols). The results for the isothermal (Iso), variable temperature (Th) and multicomponent fluids (CH), shown with squares, circles and rhombi, are overlapped at fixed values of ν_v . In all cases, the analytic predictions are shown with a continuous blue line and the agreement with the numerical results is excellent.

6. Stripe configurations in equilibrium: Laplace pressure test

This section starts the series of benchmark problems concerning an isothermal multicomponent fluid in axisymmetric ring-type configurations. We begin this section by discussing the properties of the equilibrium position in Subsec. 6.1. The stability of these equilibria with respect to non-axisymmetric configurations, as well as with respect to azimuthal perturbations, is addressed in Subsec. 6.2. The benchmark test proposed

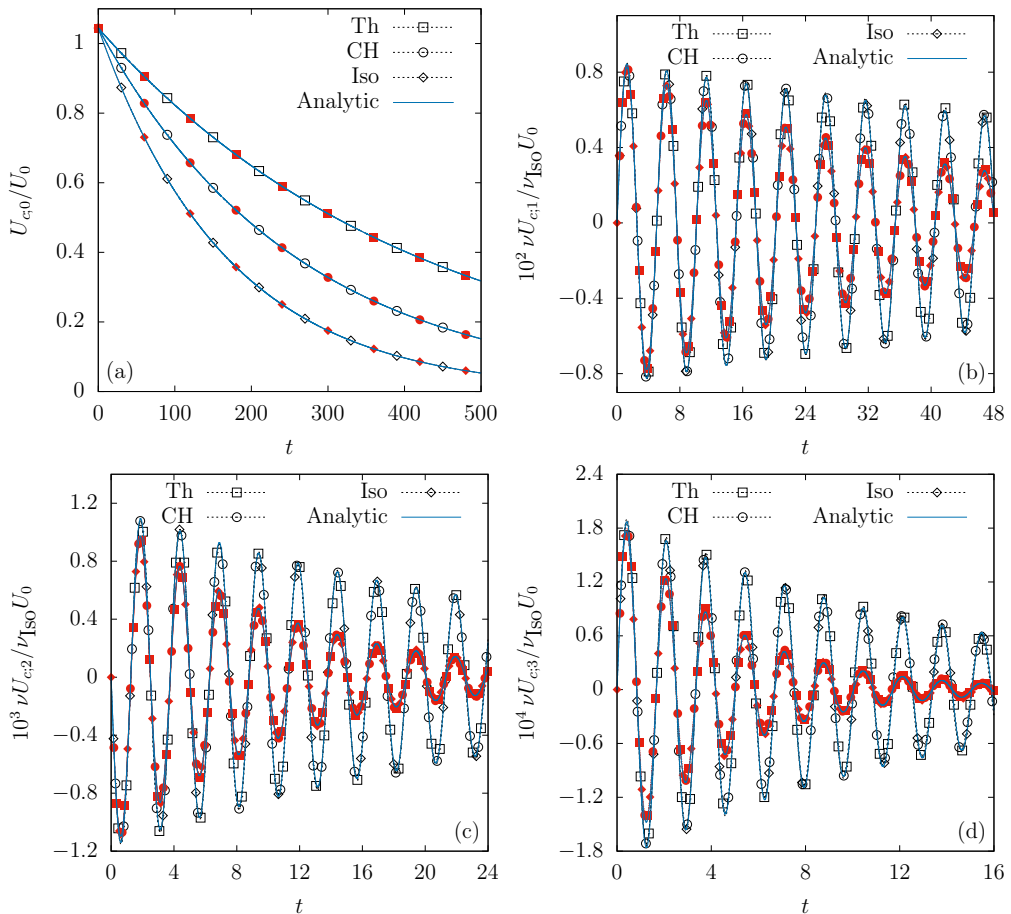


Figure 11. Time evolution of the ratio $U_{c;n}(t)/U_0$ for the initial velocity profile given in Eq. (5.28), for (a) $n = 0$, (b) $n = 1$, (c) $n = 2$ and (d) $n = 3$, on the torus with $a = 0.4$. The simulation results for $\nu_v = 0$ are shown with dashed black lines and empty symbols, while those for $\nu_v = 0.02$ are shown with dotted red lines and filled symbols. The analytic predictions for $U_{c;0}$ (5.30) and $U_{c;n>0}$ (5.34) are shown with solid blue lines. The results corresponding to the variable temperature (Th), multicomponent (CH) and isothermal (Iso) fluids are shown using squares, circles and rhombi, respectively.

in Subsec. 6.3 concerns a generalisation of the Laplace-Young pressure law, giving the difference between the pressures measured inside and outside of the considered stripe configuration.

6.1. Equilibrium position

Let the stripe interfaces be located at

$$\theta_- = \theta_c - \Delta\theta/2, \quad \theta_+ = \theta_c + \Delta\theta/2, \quad (6.1)$$

where $\Delta\theta$ is the angular span of the stripe and θ_c is its centre. The remaining part of the fluid domain consists of a stripe of width $2\pi - \Delta\theta$, centred on $\theta_c + \pi$, which is conjugate to the main stripe. For consistency, we only refer to the domain for which $0 < \Delta\theta < \pi$ as ‘the stripe’ in what follows. A snapshot of a typical stripe configuration on the torus

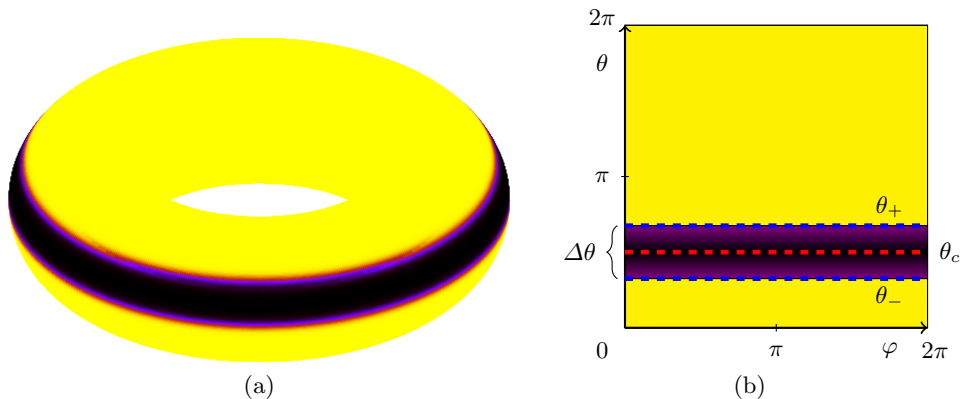


Figure 12. The axisymmetric ring-type configurations: (a) torus view and (b) unwrapped view, with the color mapping the value of the order parameter.

is shown figure 12(a). The notation introduced above is highlighted in a (φ, θ) plot in figure 12(b).

Since the torus is not geometrically homogeneous with respect to the θ direction, there will be preferred locations where the stripe can be in static equilibrium. These locations are found by imposing the minimisation of the total interface length subject to fixed stripe area ΔA , which is a universal requirement for all fluids where interfaces are present. The stripe area can be found by integrating over the domain spanned by the stripe

$$\Delta A = 2\pi r R \int_{\theta_-}^{\theta_+} d\theta (1 + a \cos \theta) = 2\pi r R [\Delta\theta + 2a \sin(\Delta\theta/2) \cos \theta_c]. \quad (6.2)$$

On the other hand, the total interface length ℓ_{total} can be found by adding the circumferences ℓ_+ and ℓ_- corresponding to $\theta = \theta_+$ and $\theta = \theta_-$, respectively

$$\begin{aligned} \ell_{\text{total}} &= \ell_+ + \ell_- = 2\pi R(1 + a \cos \theta_+) + 2\pi R(1 + a \cos \theta_-) \\ &= 4\pi R \left(1 + a \cos \frac{\Delta\theta}{2} \cos \theta_c \right). \end{aligned} \quad (6.3)$$

It can be expected that the minimisation of the interface length is required in order for the free energy, Eq. (2.6), to reach a minimum. In Sec. SM:2.3 of the supplementary material, we show that this is indeed the case to leading order with respect to ξ_0 . The correction is due to the fact that the interface shape profile, and hence the line tension, in principle have a weak dependence on the curvature of the surface.

In order to derive the equilibrium positions, we impose a fixed area ΔA . Taking the differential of Eq. (6.2) gives

$$d\Delta A = 4\pi r R \left[\left(1 + a \cos \frac{\Delta\theta}{2} \cos \theta_c \right) d\frac{\Delta\theta}{2} - a \sin \frac{\Delta\theta}{2} \sin \theta_c d\theta_c \right]. \quad (6.4)$$

Setting $d\Delta A = 0$ allows infinitesimal changes $d(\Delta\theta)$ in the stripe width to be expressed in terms of changes in the position of the stripe centre through

$$d\frac{\Delta\theta}{2} = \frac{a \sin \frac{\Delta\theta}{2} \sin \theta_c}{1 + a \cos \frac{\Delta\theta}{2} \cos \theta_c} d\theta_c. \quad (6.5)$$

At equilibrium, the interface length ℓ_{total} [Eq. (6.3)] is minimised. Mathematically, this

implies

$$d\ell_{\text{total}} = -4\pi r \left(\sin \frac{\Delta\theta}{2} \cos \theta_c d\frac{\Delta\theta}{2} + \cos \frac{\Delta\theta}{2} \sin \theta_c d\theta_c \right) = 0. \quad (6.6)$$

Substituting Eq. (6.5) into Eq. (6.6) yields

$$\left(a \cos \theta_c + \cos \frac{\Delta\theta}{2} \right) \sin \theta_c = 0, \quad (6.7)$$

where it is understood that $\Delta\theta$ and θ_c are measured when the stripe is already at its equilibrium position.

One possibility for Eq. (6.7) to be satisfied is when $\sin \theta_c = 0$. This corresponds to two potential solutions, $\theta_c = 0$ and $\theta_c = \pi$. From Eq. (6.3), it can be seen that $\theta_c = 0$ corresponds to an unstable equilibrium for stripes with $\Delta\theta < \pi$. Conversely, $\theta_c = \pi$ is unstable for the conjugate stripes, having $\Delta\theta > \pi$. Thus, for stripes with small areas, the minimum energy configuration is attained for

$$\theta_c^{eq} = \pi. \quad (6.8)$$

We now argue that the above solution is not universally valid for all stripe widths. Since the conjugate stripe, having width $2\pi - \Delta\theta$, does not equilibrate at $\theta_c^{eq} = \pi$, it is clear that increasing the stripe area must change the equilibrium position from $\theta_c^{eq} = \pi$ towards $\theta_c^{eq} = 0$ (or 2π). To illustrate this point, let us consider the case of a maximally wide stripe with $\Delta\theta = \pi$. In this case, the conjugate stripe also has width $2\pi - \Delta\theta = \pi$, and should thus be obtained via a symmetry transformation from the initial stripe. The only symmetry of the torus geometry is $z \rightarrow -z$. Thus, it is clear that the stripe can sit either on the upper half of the torus (centred on $\theta_c^{eq} = \pi/2$), or on its bottom half (where $\theta_c^{eq} = 3\pi/2$). Both configurations are equally stable and it can be seen that Eq. (6.7) is satisfied because the expression between the parentheses vanishes, while the term $\sin \theta_c^{eq} = 1$ is non-vanishing.

We expect that the equilibrium positions at $\theta_c^{eq} = \pi$ for small stripes and at $\theta_c^{eq} = \pi \pm \pi/2$ are connected smoothly as the area is increased. Thus, θ_c^{eq} must detach from π when the equilibrium stripe width exceeds a critical value, $\Delta\theta_{\text{crit}}$. We can deduce that this critical stripe width $\Delta\theta_{\text{crit}}$ corresponds to the case where both terms in Eq. (6.7) vanish simultaneously, leading to

$$\Delta\theta_{\text{crit}} = 2 \arccos(a). \quad (6.9)$$

Substituting the above value into Eq. (6.2) yields a critical area,

$$\Delta A_{\text{crit}} = 4\pi r R (\arccos a - a\sqrt{1-a^2}). \quad (6.10)$$

When $\Delta A > \Delta A_{\text{crit}}$, the point $\theta_c = \pi$ corresponds to a local maximum value for ℓ_{total} . Instead the global minima correspond to the case where only the parenthesis in Eq. (6.7) goes to zero

$$\theta_c^{eq} = \pi \pm \arccos \left[\frac{1}{a} \cos \frac{\Delta\theta_{eq}}{2} \right], \quad (6.11)$$

where $\Delta\theta_{eq} \equiv \Delta\theta(\theta_c^{eq})$ is the stripe width when it is located at the equilibrium position. We can further show that the total interface length when $\theta_c = \theta_c^{eq}$ is

$$\ell_{\text{total};\text{min}} = 4\pi R \sin^2 \frac{\Delta\theta_{eq}}{2}, \quad (6.12)$$

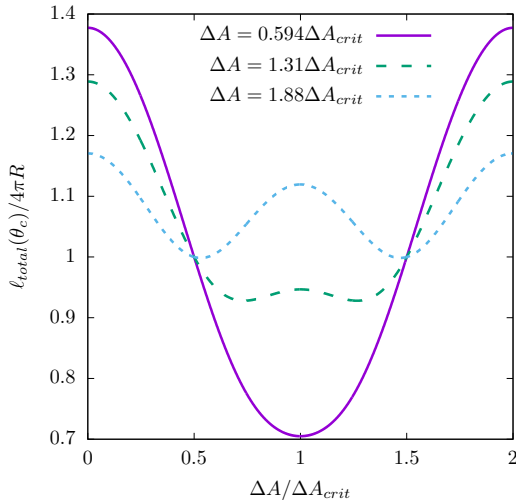


Figure 13. Interface length ℓ_{total} on a torus with $a = 0.4$ for various ratios of $\Delta A/\Delta A_{\text{crit}}$. For $\Delta A/\Delta A_{\text{crit}} < 1$ the global minimum is located at $\theta_c = \pi$, while for $\Delta A/\Delta A_{\text{crit}} > 1$ there are two equivalent minima, as given by Eq. (6.11).

with $\Delta\theta_{eq}$ satisfying

$$\Delta\theta_{eq} - a \sin \Delta\theta_{eq} = \frac{\Delta A}{2\pi r R} = \frac{2\Delta A}{\Delta A_{\text{crit}}} (\arccos a - a\sqrt{1-a^2}). \quad (6.13)$$

To better understand the nature of the solutions of Eq. (6.7), figure 13 shows the total interface length ℓ_{total} for various ratios of $\Delta A/\Delta A_{\text{crit}}$. For $\Delta A/\Delta A_{\text{crit}} < 1$, the global minimum configuration is unique and corresponds to $\theta_c^{eq} = \pi$. Then, as we increase $\Delta A/\Delta A_{\text{crit}}$ beyond 1, there is a second-order phase transition. The minimum energy configurations become bistable, as given in Eq. (6.11).

6.2. Stability of stripe configurations

In this section, we consider a relaxation of the axial symmetry constraint in order to explore the viability of the stripe configurations discussed in the previous subsection in the context of $2D$ flows. We first discuss the stability of the stripe configurations with respect to small perturbations. The main idea is to see the effects of increasing the amplitude of azimuthal interface perturbations at the level of orthogonal modes. Those modes whose growth causes the interface length to decrease lead to instability. Our analysis is limited to the linear growth regime.

Since the upper (θ_+) and lower (θ_-) interfaces are separated by the stripe domain, it is reasonable to neglect the back reaction caused by perturbing one interface on the shape of the other. For definiteness, we focus on the lower interface θ_- and assume that it is perturbed according to

$$\theta_-(\varphi) = \theta_{-,0} + \delta\theta_-(\varphi), \quad (6.14)$$

where $\theta_{-,0}$ is the average value of $\theta_-(\varphi)$, while $\delta\theta_-(\varphi)$ is a small position-dependent fluctuation, which admits the following Fourier decomposition:

$$\delta\theta_-(\varphi) = \frac{\delta}{\pi} \sum_{n=1}^{\infty} A_n \cos(n\varphi + \varphi_{n;0}), \quad (6.15)$$

where $\delta > 0$ is an overall positive infinitesimal factor, while the coefficients $A_n = O(1)$

are not necessarily small. We assume that $\theta_{-,0}$ changes under the perturbation such that the domain area,

$$\begin{aligned} \Delta A &= rR \int_0^{2\pi} d\varphi \int_{\theta_-(\varphi)}^{\theta_+} d\theta (1 + a \cos \theta) \\ &= 2\pi rR \left[\theta_+ - \theta_{-,0} + a \sin \theta_+ - a \sin \theta_{-,0} \left(1 - \frac{\delta^2}{4\pi^2} \sum_{n=1}^{\infty} A_n^2 \right) + O(\delta^3) \right], \end{aligned} \quad (6.16)$$

remains constant. Keeping in mind that the back reaction on θ_+ is negligible, imposing $d\Delta A/d\delta = 0$ implies that

$$\frac{d\theta_{-,0}}{d\delta} = \frac{\delta}{2\pi^2} \frac{a \sin \theta_{-,0}}{1 + a \cos \theta_{-,0}} \sum_{n=1}^{\infty} A_n^2. \quad (6.17)$$

Let us now compute the length ℓ_- of the lower interface

$$\begin{aligned} \ell_- &= \int_0^{2\pi} d\varphi \sqrt{R^2 [1 + a \cos \theta(\varphi)]^2 + r^2 \left(\frac{d\theta_-}{d\varphi} \right)^2} \\ &= 2\pi R (1 + a \cos \theta_{-,0}) + \frac{r\delta^2}{2\pi} \sum_{n=1}^{\infty} \left(\frac{an^2}{1 + a \cos \theta_{-,0}} - \cos \theta_{-,0} \right) A_n^2 + O(\delta^3). \end{aligned} \quad (6.18)$$

Taking the differential of ℓ_- with respect to δ while imposing Eq. (6.17) yields

$$\frac{d\ell_-}{d\delta} = \frac{r\delta}{\pi} \sum_{n=1}^{\infty} \frac{a(n^2 - 1) - \cos \theta_{-,0}}{1 + a \cos \theta_{-,0}} A_n^2. \quad (6.19)$$

The first term in the numerator has a stabilising effect, acting only on the Fourier modes with $n > 1$. The second term can be related to the Gaussian curvature K , given by

$$K \equiv K(\theta) = \frac{\cos \theta}{rR(1 + a \cos \theta)}, \quad (6.20)$$

The $n = 1$ mode becomes unstable when $K > 0$ and ℓ_- decreases when δ is increased, i.e. in the region of the torus given by $-\frac{\pi}{2} < \theta_{-,0} < \frac{\pi}{2}$. The higher-order modes become unstable deeper in the region of positive K , i.e. when $\cos \theta_{-,0}$ exceeds $a(n^2 - 1)$. An equivalent analysis can be performed for the upper interface, located at $\theta_+ = \theta_c + \Delta\theta/2$. Focussing now only on the onset of instability due to the first mode, Eq. (6.19) can be written as

$$\left(\frac{d\ell_{\pm}}{d\delta} \right)_{n=1} = -\frac{r^2 R A_1^2 \delta}{\pi} K(\theta_{\pm,0}). \quad (6.21)$$

Eq. (6.21) indicates that the upper and lower interfaces can become unstable simultaneously only when the stripe is completely contained in the region where $K > 0$ (i.e. on the outer side of the torus).

We now discuss the stability of stripes with equilibrium position characterised by Eq. (6.7), as derived in the previous subsection. Essentially, instability occurs when $\theta_-^{eq} = \theta_c^{eq} - \frac{\Delta\theta_{eq}}{2} < \frac{\pi}{2}$ or $\theta_+^{eq} = \theta_c^{eq} + \frac{\Delta\theta_{eq}}{2} > \frac{3\pi}{2}$. The subcritical stripes (having $\Delta A < \Delta A_{\text{crit}}$, which stabilise at π) do not suffer from the instability described by Eq. (6.21). For the critical stripe, as described by Eq. (6.9), it can be seen that the instability condition on both the upper and lower interfaces reduces to $\arccos a > \frac{\pi}{2}$, which is marginally satisfied only in the case $a \rightarrow 0$. Next, supercritical stripes (having $\Delta A > \Delta A_{\text{crit}}$, which stabilise

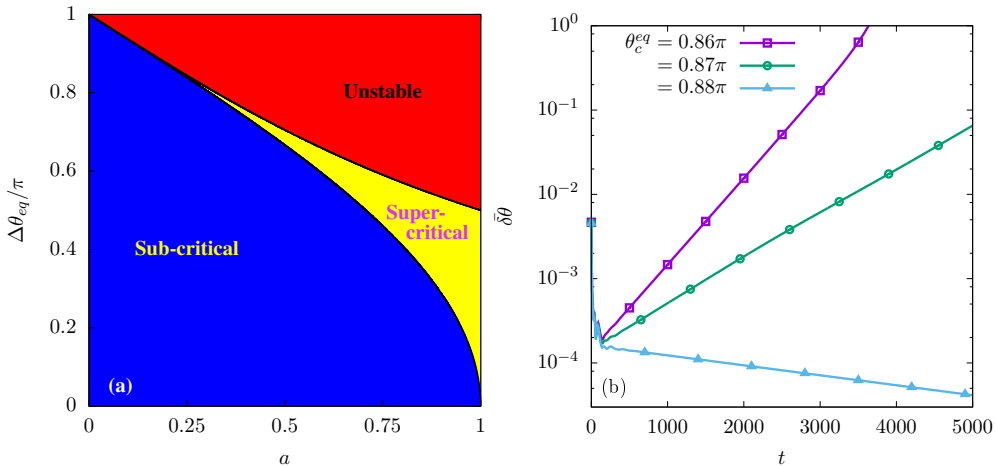


Figure 14. (a) Phase diagram showing the regions where the stripe is unstable (top right), as given by Eq. (6.22), and where it is stable (or at least metastable). The latter region is further divided into two subregions, where the stripes are subcritical ($\Delta A < \Delta A_{\text{crit}}$, bottom left) and supercritical ($\Delta A > \Delta A_{\text{crit}}$, central right). (b) Time evolution of the root mean square of the perturbations on the lower interfaces ($\theta_- = \theta_c - \Delta\theta/2$), as given by Eq. (6.24), for stripes centred on $\theta_c^{eq} = 0.86\pi, 0.87\pi$ and 0.88π , on the torus with $a = 0.4$.

away from π) are stable only when

$$\theta_{c,t}^{\text{inst}} < \theta_c^{eq} < \theta_{c,b}^{\text{inst}}, \quad \Delta\theta_{eq} < \Delta\theta_{\text{inst}},$$

$$\theta_{c,t}^{\text{inst}} = \pi - \arctan a, \quad \theta_{c,b}^{\text{inst}} = \pi + \arctan a, \quad \Delta\theta_{\text{inst}} = 2 \arctan \frac{1}{a}. \quad (6.22)$$

The interface length and area of the stripe, corresponding to the instability condition in Eq. (6.22), are given by

$$\ell_{\text{inst}} = \frac{4\pi R}{1+a^2}, \quad \Delta A_{\text{inst}} = 4\pi r R \left(\arctan \frac{1}{a} - \frac{a}{1+a^2} \right). \quad (6.23)$$

Figure 14(a) shows a separation of the $(a, \Delta\theta_{eq})$ plane into 3 regions: The subcritical region (where the stripes stabilise at π), shown in blue in the bottom left part of the plot; the super-critical region (where the stripes stabilise away from π), shown with yellow; and the unstable region (where stripes destabilise under small perturbations), shown with red in the top right part of the plot. The line separating the red and yellow regions is defined by Eq. (6.22), while the line between the yellow and blue regions is given by Eq. (6.9).

To verify the validity of Eq. (6.22), we perform some numerical experiments on the torus with $R = 1$ and $r = 0.4$ ($a = 0.4$). The stripes become unstable when $\theta_c < \theta_c^{\text{inst}} \simeq 0.8788\pi$, therefore we consider three stripes initialised at $\theta_c^{eq} = 0.86\pi, 0.87\pi$ and 0.88π , with their corresponding equilibrium widths $\Delta\theta_{eq} = \{0.764, 0.761, 0.757\}\pi$. The order parameter is initialised with the hyperbolic tangent profile given in Eq. (6.30), but the stripe width $\Delta\theta(\varphi) = \Delta\theta_0 + \varepsilon(\varphi)$ is allowed to vary with respect to the φ coordinate. The perturbation $\varepsilon(\varphi)$ is taken as a random distribution with amplitude 0.001π . The system is discretised using $N_\theta = 192$ and $N_\varphi = 288$ equidistant values for the θ and φ coordinates. After generating the values $\varepsilon_q = \varepsilon(\varphi_q)$, where $1 \leq q \leq N_\varphi$, the base width $\Delta\theta_0$ is computed such that the perturbed stripe has the area ΔA corresponding to the axisymmetric stripe with the given values for θ_c^{eq} and $\Delta\theta_{eq}$. The numerical simulations

indicate that the perturbations on the upper interface, located at $\theta_+ = \theta_c$, are quickly suppressed for all stripes, confirming the prediction of the analysis presented above. On the lower interface (θ_-), we quantify the growth of the perturbation at the level of the root-mean-square deviation, computed via

$$(\delta\bar{\theta}^2)^{1/2} = \sqrt{\frac{1}{N_\varphi} \sum_{q=1}^{N_\varphi} |\theta_-^q - \theta_-^{\text{avg}}|^2}, \quad (6.24)$$

where θ_-^{avg} is the average position of the lower interface. The results are presented in figure 14(b). It can be seen that, in the case of the stripes located at 0.86π and 0.87π , the perturbations grow exponentially with time, while in the case of the stripe centred on 0.88π , the perturbations are suppressed, confirming that the onset of the instability is given by Eq. (6.22).

The instability invariably causes the stripe to break. The final configuration must correspond to a smaller value of the total free energy. Figure 15 presents snapshots of the evolution of two unstable fluid stripes, initialised at (a) $\theta_c = 0.86\pi$ and (b) $\theta_c = 0.65\pi$, on the torus with $a = 0.4$. For convenience, the order parameter ϕ is shown using a colour map in a two-dimensional representation (top rows) and in the three-dimensional representation, on the torus (bottom rows). The stripe widths are set to the equilibrium values, $\Delta\theta = 0.764236\pi$ and 0.883748π , respectively, while the interfaces are perturbed as described in the previous paragraphs, with initial perturbation amplitude $\varepsilon = 0.02\pi$. The initial states are shown in panels (ai,bi). Panels (aii,bii) and (aiii,biii) show intermediate stages in the development of the perturbations. From figure 15 (aii,bii), it can be seen that the perturbations are dominated by the first Fourier mode, corresponding to $\cos(\varphi + \varphi_{1;0})$, thus confirming that the higher-order modes are suppressed compared to the first order one. Panels (aiii,biii) depict the configurations just before the stripes break. Finally, column (iv) shows the equilibrium configurations, which are a drop for the smaller stripe and a band, wrapping around the torus along the θ coordinate, for the larger one. Animations of the time development of the instability for the 2 cases shown in figure 15 are available as Movie 1 and Movie 2 on the publisher's website (Busuicic *et al.* 2020b).

The fact that the stripe configurations lead to droplets or bands indicates that these latter configurations correspond to lower values of the free energy. Under the assumption that the free energy is related to the interface length[†], we note that, according to Eq. (6.3), the interface length for the stripe configuration can vary as the stripe area grows between $\ell_{\text{stripe}}^{\min} = 4\pi(R - r)$ for infinitesimally small stripes (the two interfaces are at $\theta = \pi$) and $\ell_{\text{stripe}}^{\max} = 4\pi R$ for the largest stripe, covering half of the torus and having the interfaces at $\theta = 0$ and π .

For sufficiently small domain areas, the interface length of a droplet configuration grows with the domain area roughly as $\ell_{\text{droplet}} \sim \sqrt{\Delta A}$, vanishing as $\Delta A \rightarrow 0$. Thus, at sufficiently small domain areas, the droplet is energetically preferred.

The band configuration has a domain area-independent interface length, given by the two boundary circles located at constant φ , $\ell_{\text{band}} = 4\pi r$. For sufficiently large domain areas, ℓ_{band} will be smaller than ℓ_{stripe} , since $\ell_{\text{stripe}}^{\max} = 4\pi R > 4\pi r$. In fact, the band configuration can be energetically preferable to the stripe configurations for any domain size when $\ell_{\text{band}} < \ell_{\text{stripe}}^{\min}$, which is always satisfied when $a < \frac{1}{2}$.

A more comprehensive analysis of the energy landscape, indicating which configura-

[†] We note that, as revealed in Sec. SM:2.3, the free energy for the stripe configurations is just $\Psi = \sigma\ell_{\text{total}} + O(\xi^2)$. This simple relation may not hold for more general domain shapes.

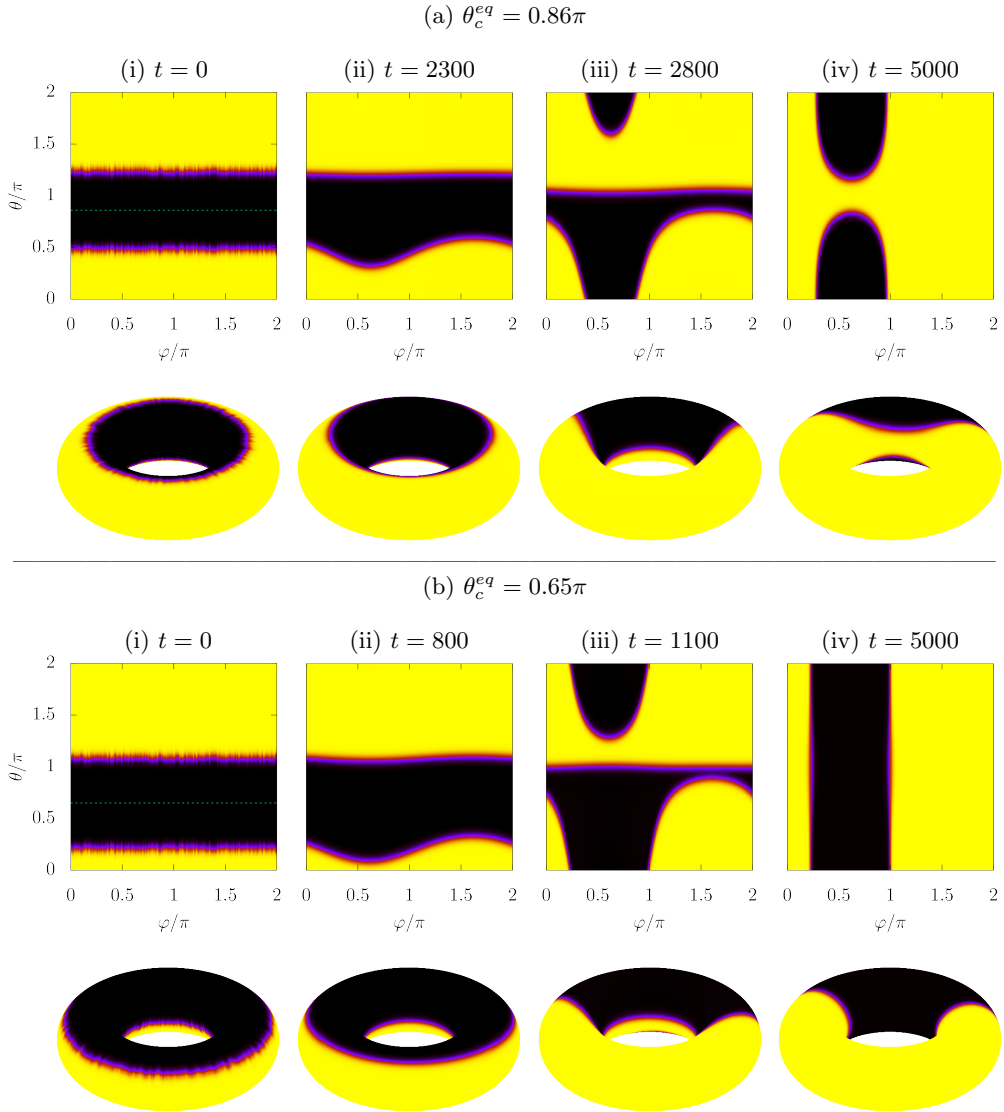


Figure 15. Time evolution of two unstable stripes on the torus with $a = 0.4$. (a) The stripe is initialised at $\theta_c^{e_q} = 0.86\pi$ and leads after breaking to a droplet configuration equilibrated on the outer side of the torus (animation available as Movie 1 on the publisher's website). (b) The stripe is initialised at $\theta_c^{e_q} = 0.65\pi$ and merges on the poloidal direction after breaking to form a band configuration (animation available as Movie 2 on the publisher's website). In (a-b), column (i) shows the initial conditions, with perturbations along the φ direction on both interfaces. Columns (ii) and (iii) contain intermediate snapshots of the configurations. Column (iv) shows the final equilibrium configurations.

tions correspond to the minimum of the free energy, would require a detailed study of the droplet and band configurations, which is beyond the scope of this work. However, based on the discussion in the previous paragraph, it is safe to conclude that there are domains of the subcritical and supercritical regions shown in figure 14(a) where the stripe configurations are actually only metastable.

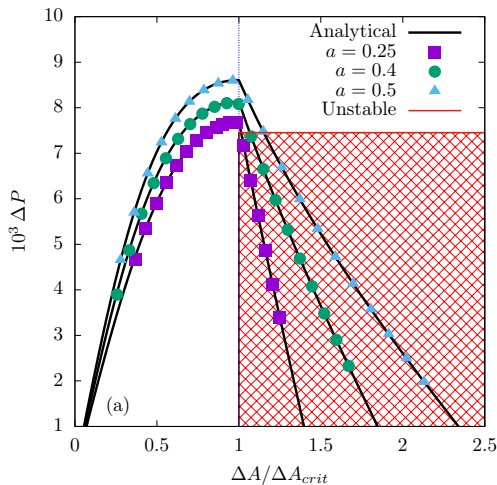


Figure 16. Comparison of numerical results obtained for $a = 0.25$ (solid squares), $a = 0.4$ (solid circles) and $a = 0.5$ (solid triangles) against the analytic formula (6.28). The system parameters are $A = 0.5$, $\kappa = 5 \times 10^{-4}$ and $M = \tau = 2.5 \times 10^{-3}$. The simulations are performed using $N_\theta = \{200, 320, 400\}$ nodes along the θ direction for $r = \{0.5, 0.8, 1.0\}$, while the time step was set to $\delta t = 2 \times 10^{-3}$. The shaded region corresponds to the stripes which are unstable when the axisymmetric assumption is lifted.

6.3. Laplace pressure

We now seek for an expression for the pressure difference ΔP between the two fluid components. For a small increase $\delta\Delta A$ of the stripe area, let $\delta\ell_{\text{total}}$ be the increase in the interface length. These two quantities can be related through the equation

$$\Delta P \delta\Delta A = \sigma \delta\ell_{\text{total}}. \quad (6.25)$$

The variations $\delta\Delta A$ and $\delta\ell_{\text{total}}$ can be computed using Eqs. (6.2) and (6.3):

$$\delta\Delta A = 4\pi r R \left(1 + a \cos\theta_c \cos\frac{\Delta\theta}{2}\right) \delta\frac{\Delta\theta}{2}, \quad \delta\ell_{\text{total}} = -4\pi r \cos\theta_c \sin\frac{\Delta\theta}{2} \delta\frac{\Delta\theta}{2}. \quad (6.26)$$

Thus, the pressure difference ΔP can be written as

$$\Delta P = -\frac{\sigma}{R} \frac{\cos\theta_c \sin(\Delta\theta/2)}{1 + a \cos\theta_c \cos(\Delta\theta/2)}. \quad (6.27)$$

The above expression is valid regardless of where the stripe is positioned.

Assuming that the stripe is already in its equilibrium position, Eq. (6.27) reduces to

$$\Delta P = \begin{cases} \frac{\sigma}{R} \frac{\sin(\Delta\theta_{eq}/2)}{1 - a \cos(\Delta\theta_{eq}/2)}, & \Delta A < \Delta A_{\text{crit}} \text{ and } \theta_c^{eq} = \pi, \\ \frac{\sigma}{r} \cot\frac{\Delta\theta_{eq}}{2}, & \Delta A > \Delta A_{\text{crit}} \text{ and } a \cos\theta_c^{eq} + \cos\frac{\Delta\theta_{eq}}{2} = 0. \end{cases} \quad (6.28)$$

Equation (6.28) loses relevance in the domain of stripe instability discussed in Subsec. 6.2, unless strict axisymmetry is enforced. On the instability line, where Eqs. (6.22) and (6.23) hold, we find

$$\Delta P_{\text{inst}} = \frac{\sigma}{R}, \quad (6.29)$$

which, remarkably, is independent of a .

We now propose the benchmark test concerning stripe configurations, consisting of the

generalisation of the Laplace-Young pressure test. An alternative derivation of Eq. (6.27) in the context of the Cahn-Hilliard model considered in this paper is provided in Sec. SM:2.1 of the supplementary material. It is interesting to note that the Laplace pressure is related to a non-vanishing value of the chemical potential when the stripe is in equilibrium. This in turn induces an offset in the order parameter, denoted using ϕ_0 and computed in Eq. (SM:2.21) of the supplementary material.

We perform a series of numerical simulations in the absence of hydrodynamics at three values of a , namely $a = 0.25, 0.4$ and 0.5 , by fixing the outer radius to $R = 2$ and setting the inner radius to $r = \{0.5, 0.8, 1.0\}$, while keeping $M = 2.5 \times 10^{-3}$, $\kappa = 5 \times 10^{-4}$ and $A = 0.5$ unchanged. We consider stripes of various areas ΔA . For each value of ΔA , the equilibrium position θ_c^{eq} is computed and the stripe is initialised using a hyperbolic tangent profile,

$$\phi = \phi_0 + \tanh \zeta, \quad \zeta = \frac{r}{\xi_0 \sqrt{2}} \left(\widetilde{|\theta - \theta_c|} - \frac{\Delta\theta}{2} \right), \quad (6.30)$$

and centred on $\theta_c = \theta_c^{eq} - \delta\theta$, with $\delta\theta = 0.05\pi$. The notation $\widetilde{|\theta - \theta_c|}$ indicates that the angular difference $\theta - \theta_c$ takes values between $-\pi$ and π . The initial width $\Delta\theta$ is obtained by numerically solving Eq. (6.2) for fixed ΔA and θ_c . The value of ϕ_0 corresponding to the initial stripe centre θ_c and initial width $\Delta\theta$ is derived in Sec. (SM:2.1) of the supplementary material. It is given by

$$\phi_0 = \frac{\xi_0}{3R\sqrt{2}} \frac{\cos \theta_c \sin(\Delta\theta/2)}{1 + a \cos \theta_c \cos(\Delta\theta/2)}. \quad (6.31)$$

After initialisation, the stripes slowly migrate towards the equilibrium positions, as discussed in the Sec. SM:2.4 of the supplementary material. In order to reach the stationary state, we performed 4×10^9 iterations at $\delta t = 0.002$. After the stationary state was reached, we measured the pressure $P_{\text{binary}} = A(-\frac{1}{2}\phi^2 + \frac{3}{4}\phi^4)$ in the interior and exterior of the stripe and computed the difference ΔP between these two values. The results are shown using dotted lines and symbols in figure 16. The shaded region indicates the region where the stripes become unstable once the axisymmetric assumption is removed in the model. It is bounded from above by the pressure difference value ΔP_{inst} on the instability line, given in Eq. (6.29). We observe an excellent agreement with the analytic result, Eq. (6.28), which is shown using solid lines.

It is worth noting that the second-order phase transition observed in the stripe equilibrium positions when $\Delta A = \Delta A_{\text{crit}}$ is also visible in the dependence of ΔP on ΔA in figure 16. Its non-monotonic behaviour can be understood as follows. For infinitesimally small stripes, the torus curvature is negligible and no pressure difference can be seen across the interface, as is also the case for the Cartesian (flat space) geometry. As the stripe width $\Delta\theta$ increases, ΔP also increases. In general, a turning point in the Laplace pressure can be expected. This is because the pressure difference vanishes for infinitesimal stripes ($\Delta\theta \rightarrow 0$), as well as in the opposite case, when the stripe occupies the top or bottom halves of the torus ($\Delta\theta \rightarrow \pi$). In the latter case, the conjugate domain can be obtained from the stripe by employing a symmetry transformation, $z \leftrightarrow -z$, which also changes the torus into itself. Thus, the configurations corresponding to the stripe and its conjugate are perfectly equivalent and one can expect there to be no pressure difference across the interface. When the equilibrium position of the stripe is always centred on $\theta_c^{eq} = \pi$, a smooth dependence of ΔP on $\Delta\theta$ can be expected. However, the phase transition at $\Delta A = \Delta A_{\text{crit}}$ which causes the stripe to detach from $\theta_c = \pi$ leads to the sharp change observed in figure 16.

7. Evolution of fluid stripes in a Cahn-Hilliard multicomponent fluid

In this section we consider the dynamics of the axisymmetric fluid stripes discussed in Sec. 6. Here, we focus on the case where the Cahn-Hilliard equation is fully coupled with hydrodynamics, when the stripes undergo underdamped oscillatory motion towards their equilibrium positions. The relaxation dynamics in the absence of hydrodynamics is discussed in detail in Sec. SM:2.4 of the supplementary material, where we are able to obtain a semi-analytical description of how the stripes relax exponentially to their equilibrium positions. From the perspective of benchmarking Navier-Stokes solver on non-uniform curved surfaces, this section is a culmination of the various ingredients developed in Sec. 3, 5 and 6. In particular, we find that the dynamics is governed to leading order by the zeroth-order mode of the velocity derived in Eq. (3.23), which corresponds to incompressible flow. This section is structured as follows. The general solution for the underdamped oscillatory motion is presented in Subsec. 7.1. A benchmark test is proposed in Subsec. 7.2.

7.1. General solution

To derive the stripe dynamics, our starting point is the Cauchy equation in the linearised regime

$$\frac{\partial u^{\hat{\theta}}}{\partial t} = -\frac{k_B T}{mr} \frac{\partial \delta \rho}{\partial \theta} + \frac{\nu}{r^2(1+a \cos \theta)^2} \frac{\partial}{\partial \theta} \left[(1+a \cos \theta)^3 \frac{\partial}{\partial \theta} \left(\frac{u^{\hat{\theta}}}{1+a \cos \theta} \right) \right] + \frac{\nu_v}{r^2} \frac{\partial}{\partial \theta} \left\{ \frac{\partial_{\theta}[u^{\hat{\theta}}(1+a \cos \theta)]}{1+a \cos \theta} \right\} - \frac{\phi}{\rho_0 r} \frac{\partial \mu}{\partial \theta}. \quad (7.1)$$

As in Sec. 3 and 5, we will employ the decomposition written in Eq. (3.18) for $u^{\hat{\theta}}$. Moreover, we will also take advantage of the fact that the higher-order terms $U_{c,n}$ and $U_{s,n}$ ($n > 0$) are damped at a significantly higher rate than the fundamental term U_0 . Then, in order to track the evolution of U_0 , we multiply Eq. (7.1) with $f_0/2\pi = (1-a^2)^{1/4}/2\pi$, and integrate it over θ between 0 and 2π , to obtain

$$\dot{U}_0 + \frac{2\nu a^2}{r^2(1-a^2)} U_0 + \frac{(1-a^2)^{1/4}}{2\pi \rho_0 r} I_{\mu} \simeq 0, \quad I_{\mu} = \int_0^{2\pi} d\theta \phi \frac{\partial \mu}{\partial \theta}, \quad (7.2)$$

where the \simeq sign indicates that the nonlinear terms, as well as the components of $u^{\hat{\theta}}$ with $n > 0$, have been neglected. Employing integration by parts, I_{μ} can be written as

$$I_{\mu} = \int_0^{2\pi} d\theta \left[A \frac{\partial}{\partial \theta} \left(\frac{\phi^2}{2} - \frac{\phi^4}{4} \right) + \frac{\kappa}{r^2} \frac{\partial \phi}{\partial \theta} \frac{\partial^2 \phi}{\partial \theta^2} - \frac{\kappa}{r^2} \frac{a \sin \theta}{1+a \cos \theta} \left(\frac{\partial \phi}{\partial \theta} \right)^2 \right]. \quad (7.3)$$

The first and second terms above do not contribute to the integral. To evaluate the integral of the third term, we assume that ϕ is approximately given by the hyperbolic tangent profile in Eq. (6.30) and employ the procedure introduced in Sec. SM:2.1 of the supplementary material, which we briefly review here. First, the integration variable is changed to $\vartheta = \theta - \theta_c$ and the integration domain is shifted to $-\pi < \vartheta < \pi$. Then, the flip $\vartheta \rightarrow -\vartheta$ is performed on the negative ($\vartheta < 0$) branch, yielding

$$I_{\mu} = -\pi a A \int_0^{\pi} \frac{d\vartheta}{2\pi} \left[\frac{\sin(\theta_c + \vartheta)}{1+a \cos(\theta_c + \vartheta)} + \frac{\sin(\theta_c - \vartheta)}{1+a \cos(\theta_c - \vartheta)} \right] \frac{1}{\cosh^4 \zeta}. \quad (7.4)$$

Next, the integration variable is changed to $\zeta = r\vartheta/\xi_0\sqrt{2}$, where $\zeta = \vartheta - \Delta\theta/2$, such that the integration domain is $-r\Delta\theta/\xi_0\sqrt{8} < \zeta < r(2\pi - \Delta\theta)/\xi_0\sqrt{8}$. Noting that $\xi_0 \ll r\Delta\theta$,

the integration domain can be extended to $(-\infty, \infty)$ and I_μ becomes

$$I_\mu = -\frac{3\sigma}{4R} \int_{-\infty}^{\infty} \frac{d\zeta}{\cosh^4 \zeta} \left[\frac{\sin\left(\theta_+ + \frac{\xi_0 \zeta \sqrt{2}}{r}\right)}{1 + a \cos\left(\theta_+ + \frac{\xi_0 \zeta \sqrt{2}}{r}\right)} + \frac{\sin\left(\theta_- - \frac{\xi_0 \zeta \sqrt{2}}{r}\right)}{1 + a \cos\left(\theta_- - \frac{\xi_0 \zeta \sqrt{2}}{r}\right)} \right], \quad (7.5)$$

where $\sigma = \sqrt{8\kappa\Lambda/9}$ is the line tension and $\theta_\pm = \theta_c \pm \Delta\theta/2$. We now consider an expansion of the integrand with respect to $\xi_0\zeta/r$. The dominant contribution comes from the zeroth-order term. Since the integration domain is even with respect to ζ , the first-order term of the expansion does not contribute. Considering that $\xi_0/r \ll 1$, the higher-order terms can be discarded and I_μ can be approximated through

$$I_\mu \simeq -\frac{2\sigma \sin\theta_c [a \cos\theta_c + \cos(\Delta\theta/2)]}{R (1 + a \cos\theta_-)(1 + a \cos\theta_+)}. \quad (7.6)$$

Substituting Eq. (7.6) into Eq. (7.2), we obtain

$$\dot{U}_0 + 2\alpha_\nu U_0 - \frac{\sigma(1-a^2)^{1/4} \sin\theta_c [\cos(\Delta\theta/2) + a \cos\theta_c]}{\pi r R \rho_0 (1 + a \cos\theta_-)(1 + a \cos\theta_+)} = 0, \quad (7.7)$$

where the viscous damping coefficient $\alpha_\nu = \nu/(R^2 - r^2)$ is introduced in Eq. (5.30).

The relation between $U_0(t)$ and $\theta_c(t)$ can be established by evaluating the Cahn-Hilliard equation on the top and bottom interfaces $\theta = \theta_\pm$:

$$\frac{r}{\xi_0 \sqrt{2}} \left[-\dot{\theta}_+ + \frac{u_+^{\hat{\theta}}}{r} \right] = M(\Delta\mu)_+, \quad \frac{r}{\xi_0 \sqrt{2}} \left[\dot{\theta}_- - \frac{u_-^{\hat{\theta}}}{r} \right] = M(\Delta\mu)_-, \quad (7.8)$$

where we have kept the leading-order term of the time derivative of ϕ , assuming it takes the hyperbolic tangent profile in Eq. (6.30) and evaluating it on the two interfaces

$$\left. \frac{\partial\phi}{\partial t} \right|_{\theta_\pm} \simeq \mp \frac{r\dot{\theta}_\pm}{\xi_0 \sqrt{2}}. \quad (7.9)$$

Subtracting the two equations in Eq. (7.8), we obtain

$$\frac{u_+^{\hat{\theta}} + u_-^{\hat{\theta}}}{2r} = \dot{\theta}_c + \frac{\xi_0 M}{r\sqrt{2}} [(\Delta\mu)_+ - (\Delta\mu)_-]. \quad (7.10)$$

On the left hand side, the velocity profile can be approximated through its zeroth-order term, corresponding to the velocity profile of an incompressible flow

$$u_+^{\hat{\theta}} \simeq \frac{U_0(t) f_0(\theta)}{1 + a \cos\theta_+}, \quad u_-^{\hat{\theta}} \simeq \frac{U_0(t) f_0(\theta)}{1 + a \cos\theta_-}, \quad (7.11)$$

as discussed in Eq. (3.23). The function $f_0(\theta) = (1 - a^2)^{1/4}$ is introduced in Eq. (3.14). Thus, the left hand side of Eq. (7.10) can be written as

$$\frac{u_+^{\hat{\theta}} + u_-^{\hat{\theta}}}{2r} \simeq \frac{U_0(t)(1 - a^2)^{1/4} [1 + a \cos\theta_c \cos(\Delta\theta/2)]}{r(1 + a \cos\theta_+)(1 + a \cos\theta_-)}. \quad (7.12)$$

The right hand side of Eq. (7.10) is identical to the equation for the stripe relaxation dynamics in the absence of hydrodynamics, as discussed in Sec. SM:2.4 of the supplementary material. When hydrodynamics is present, which is the case in this section, the term on the left hand side dominates over the second term on the right hand side of Eq. (7.10). We will also now consider the linearised limit when $\delta\theta = \theta_c - \theta_c^{eq}$ is a small

quantity. In this case, Eq. (7.10) yields

$$U_0(t) = \frac{r(1 + a \cos \theta_+^{eq})(1 + a \cos \theta_-^{eq})}{(1 - a^2)^{1/4}[1 + a \cos \theta_c^{eq} \cos(\Delta\theta_{eq}/2)]} \dot{\delta\theta}. \quad (7.13)$$

Taking the derivative of Eq. (7.13) allows \dot{U}_0 to be expressed in the linearised limit as

$$\dot{U}_0(t) = \frac{r(1 + a \cos \theta_+^{eq})(1 + a \cos \theta_-^{eq})}{(1 - a^2)^{1/4}[1 + a \cos \theta_c^{eq} \cos(\Delta\theta_{eq}/2)]} \ddot{\delta\theta}. \quad (7.14)$$

Eqs. (7.13) and (7.14) can be inserted into Eq. (7.7) to obtain an equation governing the evolution of $\delta\theta$. The last term in Eq. (7.7) can be linearised using Eqs. (7.15) and (7.16), as follows:

$$\sin \theta_c \left(a \cos \theta_c + \cos \frac{\Delta\theta}{2} \right) \simeq -\delta\theta \times \begin{cases} \cos(\Delta\theta_{eq}/2) - a, & \Delta A < \Delta A_{\text{crit}}, \\ 2a \sin^2 \theta_c^{eq}, & \Delta A > \Delta A_{\text{crit}}. \end{cases}, \quad (7.15)$$

$$(1 + a \cos \theta_+)(1 + a \cos \theta_-) \simeq \begin{cases} [1 - a \cos(\Delta\theta_{eq}/2)]^2, & \Delta A < \Delta A_{\text{crit}}, \\ (1 - a^2) \sin^2(\Delta\theta_{eq}/2), & \Delta A > \Delta A_{\text{crit}}. \end{cases} \quad (7.16)$$

After some rearrangements, the following equation is obtained for $\delta\theta$:

$$\ddot{\delta\theta} + 2\alpha_\nu \dot{\delta\theta} + \omega_0^2 \delta\theta = 0. \quad (7.17)$$

When $\Delta A < \Delta A_{\text{crit}}$, $\theta_c^{eq} = \pi$ and ω_0^2 is given by

$$\omega_0^2 = \frac{\sigma \sqrt{1 - a^2}}{\pi r^2 R \rho_0} \frac{\cos(\Delta\theta_{eq}/2) - a}{[1 - a \cos(\Delta\theta_{eq}/2)]^3}. \quad (7.18)$$

For $\Delta A > \Delta A_{\text{crit}}$, the equilibrium position is at $\cos(\Delta\theta_{eq}/2) + a \cos \theta_c^{eq} = 0$ and ω_0^2 is given by:

$$\omega_0^2 = \frac{2\sigma}{\pi r^3 \rho_0 (1 - a^2)^{3/2}} \frac{a^2 - \cos^2(\Delta\theta_{eq}/2)}{\sin^2(\Delta\theta_{eq}/2)}. \quad (7.19)$$

On the instability line, characterised by Eqs. (6.22) and (6.23), we find

$$\omega_0^2 = \frac{2\sigma a}{\pi R^3 \rho_0 (1 - a^2)^{3/2}}. \quad (7.20)$$

The general solution of Eq. (7.17) is

$$\delta\theta = \delta\theta_0 \cos(\omega_0 t + \vartheta) e^{-\alpha_\nu t}, \quad (7.21)$$

where $\delta\theta_0$ and ϑ are integration constants. It is understood that, in the unstable region given by $\theta_c < \pi - \arctan a$ or $\theta_c > \pi + \arctan a$, the above solution is valid only for strictly axisymmetric flows. In principle, there is a correction to the exponential decay term due to the second term on the right hand side of Eq. (7.10). However, we find that this correction is approximately one or two orders of magnitude smaller than α_ν , (a more detailed analysis of the dynamics of stripes in the absence of hydrodynamics can be found in Subsec. SM:2.4 of the supplementary material).

7.2. Benchmark test

The solution derived in Eq. (7.21) can serve as a benchmark for solvers involving interface dynamics. This benchmark test is particularly difficult since the dynamics of the interface can be significantly altered by numerical artefacts, such as the spurious velocity at the interface, which are known to plague numerical solutions (Sofonea *et al.* 2004; Shan 2006).

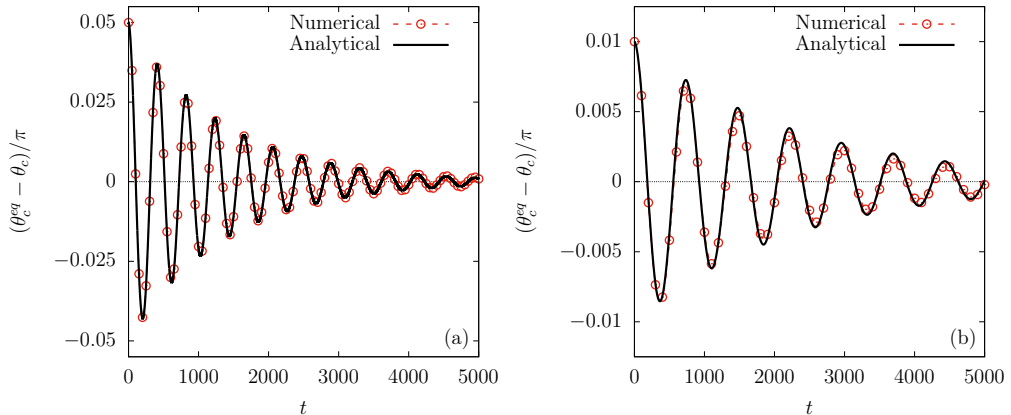


Figure 17. Time evolution of the stripe center θ_c for stripes initialised at (a) $\theta_0 = 0.95\pi$ with $\Delta\theta_0 = 0.280\pi$ (equilibrating at $\theta_c^{eq} = \pi$, on the torus with $a = 0.4$); and (b) $\theta_0 = 0.79\pi$ with $\Delta\theta_0 = 0.552\pi$ (equilibrating at $\theta_c^{eq} = 4\pi/5$, on the torus with $a = 0.8$). The numerical results are shown using dotted lines and symbols, while the analytic solution Eq. (7.21) is shown with solid lines.

In the numerical tests discussed below, the velocity field is initialised with $u^{\hat{\varphi}} = 0$ and $u^{\hat{\theta}} = U_0 f_0(\theta)/(1 + a \cos \theta)$, where $f_0(\theta) = (1 - a^2)^{1/4}$ is the zeroth-order harmonic derived in Eq. (3.14) and U_0 is computed based on Eq. (7.13) using the solution in Eq. (7.21) with $\vartheta = 0$ and $\delta\dot{\theta} = -\alpha_\nu \delta\theta_0$. The order parameter is initialised with the hyperbolic tangent profile in Eq. (6.30).

In the first test, we consider a stripe equilibrating at $\theta_c^{eq} = \pi$, on the torus with $R = 2$ and $r = 0.8$ ($a = 0.4$). The stability region for this torus is $0.8789\pi < \theta_c^{eq} < 1.1211\pi$. We choose an initial amplitude of $\delta\theta_0 = -0.05\pi$ (the initial position is $\theta_0 = 0.95\pi$). The initial stripe width is set to $\Delta\theta_0 = 0.280406\pi$ (at equilibrium, $\Delta\theta_{eq} \simeq 0.282296\pi \simeq 0.38\Delta\theta_{crit}$). The simulation parameters are $\kappa = 2.5 \times 10^{-4}$, $A = 0.5$, $\nu = M = 2.5 \times 10^{-3}$, $\nu_v = 0$ and $\rho_0 = 20$, resulting in $\omega_0 \simeq 0.0152$ and $\alpha_\nu = 7.44 \times 10^{-4}$. The number of nodes and time step are $N_\theta = 480$ and $\delta t = 5 \times 10^{-4}$. The numerical results, shown with red dashed lines and empty circles, are shown alongside the analytical curve corresponding to Eq. (7.21) with $\vartheta = 0$ and angular velocity ω_0 computed using Eq. (7.18) in figure 17(a). Without resorting to any fitting routines, it can be seen that the analytic expression provides an excellent match to the simulation results.

For the second test, we choose a stripe equilibrating away from π . In order for this test to be meaningful also when axisymmetry is not strictly imposed, we seek to ensure that the stripe evolution occurs exclusively in the region of stability. For this reason, we increase a to 0.8 ($R = 2$ remains the same as before and r is increased to 1.6), such that the stability region is now $0.7853\pi \leq \theta_c^{eq} \leq 1.2147\pi$. Taking $\theta_c^{eq} = 0.8\pi$ (corresponding to the equilibrium width $\Delta\theta_{eq} \simeq 0.551868\pi \simeq 1.98\Delta\theta_{crit}$), we choose an initial amplitude of $\delta\theta_0 = -0.01\pi$, such that $\theta_0 = 0.79\pi$ and $\Delta\theta_0 = 0.539376\pi$. At larger initial amplitudes, the evolution of the stripe becomes visibly asymmetric, due to the inequivalence between the left and right sides of the equilibrium position. The fluid parameters are set to $\kappa = 1.25 \times 10^{-4}$, $A = 0.25$, $\nu = M = 6.25 \times 10^{-4}$, $\nu_v = 0$ and $\rho_0 = 20$, resulting in $\omega_0 \simeq 8.49 \times 10^{-3}$ and $\alpha_\nu \simeq 4.34 \times 10^{-4}$. The number of nodes and time step are set to $N_\theta = 960$ and $\delta t = 5 \times 10^{-3}$. The simulation results, shown using a red dashed line with empty circles, are shown alongside the analytic result, given by Eq. (7.21) with ω_0 computed using Eq. (7.19), are in good agreement, as can be seen from figure 17(b).

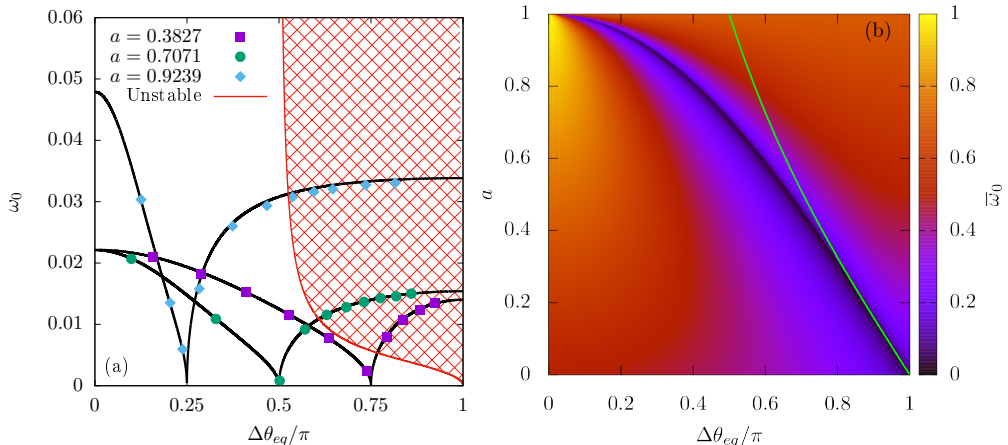


Figure 18. (a) Comparison between the values of ω_0 obtained by fitting Eq. (7.21) to the numerical results, shown with points, and the analytic expressions, Eq. (7.18) for $\Delta\theta < \Delta\theta_{\text{crit}}$ (on the descending branch) and Eq. (7.19) for $\Delta\theta > \Delta\theta_{\text{crit}}$ (on the ascending branch). The radii ratios where chosen such that $\Delta\theta_{\text{crit}} = \{0.25\pi, 0.5\pi, 0.75\pi\}$. The shaded area indicates the region where the stripe configurations are unstable. (b) Colour plot representation of the regularised angular velocity, $\bar{\omega}_0$, defined in Eq. (7.22), with respect to $\Delta\theta_{eq}/\pi$ (horizontal axis) and $a = r/R$ (vertical axis). The green dashed line separates the stability (bottom left) from the instability (top right) regions of the parameter space.

We now discuss some of the properties of the oscillation frequency, ω_0 . As can be seen from Eqs. (7.18) and (7.19), ω_0^2 is proportional to the line tension, σ , and inversely proportional to the fluid density, ρ_0 . No explicit dependence can be seen on the viscosities ν and ν_v . This is to be expected, since the line tension is responsible for the driving force, while the local mass density is a measure of the fluid inertia.

Keeping ρ_0 and σ fixed and considering fixed values of the torus radii, r and R , ω_0 exhibits a non-monotonic dependence on the stripe width at equilibrium, $\Delta\theta_{eq}$. Considering that the stripes of negligible width are always subcritical, we have $\lim_{\Delta\theta_{eq} \rightarrow 0} \omega_0 = \sigma\sqrt{1-a^2}/\pi r^2 R \rho_0 (1-a)^2$. At the other end of the spectrum, stripes with $\Delta\theta_{eq} = \pi$ have $\lim_{\Delta\theta_{eq} \rightarrow \pi} \omega_0 = 2\sigma/\pi r R^2 \rho_0 (1-a^2)^{3/2}$. In between, it can be seen that ω_0 vanishes for critical stripes on both the subcritical [Eq. (7.18)] and supercritical [Eq. (7.19)] branches. This is highlighted in figure 18(a), where ω_0 is represented as a function of $\Delta\theta_{eq}$ for three values of $a = r/R$, namely 0.3827 (purple squares), 0.7071 (green circles) and 0.9239 (blue rhombi). These values are chosen such that the critical stripe width is $\Delta\theta_{eq} = 3\pi/4$, $\pi/2$ and $\pi/4$, respectively. The shaded region marks the instability region, being bounded from below by Eq. (7.20). The numerical values of ω_0 are obtained by performing a two-parameter fit of Eq. (7.21) with respect to α_ν and ω_0 (the offset is set to $\varsigma = 0$) on the numerical data. The other fluid parameters are $\rho_0 = 20$, $\nu = 2.5 \times 10^{-3}$, $\nu_v = 0$, $\kappa = 5 \times 10^{-4}$ and $A = 0.5$, while $R = 2$ is kept fixed. The corresponding analytic results are shown with solid black lines. An excellent agreement can be seen, even for the nearly critical stripe, for which ω_0 is greatly decreased.

In order to further explore the properties of ω_0 , we focus on its dependence on the stripe width at equilibrium, $\Delta\theta_{eq}$, and on the torus aspect ratio $a = r/R$. From Eq. (7.18), it is clear that ω_0 diverges as $r^{-1} = (aR)^{-1}$ when $a \rightarrow 0$. This is to be expected, since ω_0 is proportional to the number of oscillations per unit time, which increases as r is decreased. Furthermore, Eq. (7.19) shows that when $a \rightarrow 1$, ω_0 diverges as $(1-a^2)^{-3/4}$. From the above discussion, it is instructive to introduce the dimensionless, regularised

oscillation frequency, $\bar{\omega}_0$, through

$$\bar{\omega}_0^2 \equiv \frac{\pi\rho_0}{4\sigma} r^2 R (1-a^2)^{3/2} \omega_0^2 = \begin{cases} \frac{[\cos(\Delta\theta_{eq}/2) - a](1-a^2)^2}{4[1 - a \cos(\Delta\theta_{eq}/2)]^3}, & \Delta\theta_{eq} < \Delta\theta_{crit}, \\ \frac{[a^2 - \cos^2(\Delta\theta_{eq}/2)]}{2a \sin^2(\Delta\theta_{eq}/2)}, & \Delta\theta_{eq} > \Delta\theta_{crit}, \end{cases} \quad (7.22)$$

where the factor $\pi/4$ was introduced for normalisation purposes. It can be seen that $\bar{\omega}_0$ attains the maximum value with respect to $\Delta\theta_{eq}$ when $\Delta\theta_{eq} \rightarrow 0$. This value is

$$\lim_{\Delta\theta_{eq} \rightarrow 0} \bar{\omega}_0 = \frac{1+a}{2}. \quad (7.23)$$

The regularised angular velocity $\bar{\omega}_0$ is represented in figure 18(b) as a function of the stripe width $\Delta\theta_{eq}/\pi$ (on the horizontal axis) and the radii ratio $a = r/R$ (on the vertical axis). Due to the chosen normalisation, the colour map spans $[0, 1]$. The dark line joining the bottom right and top left corners corresponds to the parameters of the critical stripe. The green dashed line delimits the regions of stability (bottom left) and instability (top right).

8. Conclusions

In this work, we focussed on a series of axisymmetric flows on the torus geometry which are solvable analytically. The analytical results are also directly and systematically compared against numerical results obtained using a finite-difference Navier-Stokes solver.

Starting with perfect fluids, we first investigated the propagation of sound waves, identifying the discrete set of frequencies allowed on the torus geometry. In contrast to the planar geometry, the even and odd modes are no longer degenerate. Moreover, since the ratios of the eigenfrequencies are not integers, the periodicity in the fluid flows is lost. We also showed that the sound speed can be altered when changing the equation of state by considering isothermal and thermal ideal fluids, as well as multicomponent flows described via the Cahn-Hilliard equation.

We next looked at the equivalent of the popular shear wave damping problem in Cartesian coordinates. Here, we considered a fluid flowing along the azimuthal direction, with vanishing poloidal velocity. Under the assumption of axial symmetry, we showed that the velocity can be expanded with respect to a discrete set of basis functions which are the eigenfunctions of a second-order differential operator with respect to the poloidal coordinate θ . The eigenvalues corresponding to these eigenfunctions control the damping rate of the associated velocity components. In particular, we highlighted the relaxation of an initially constant velocity profile towards the zeroth order eigenfunction, corresponding to a vanishing eigenvalue, which corresponds to a non-dissipative flow.

The third problem concerns the damping of sound waves. Here, we discussed the effect of the various dissipative terms appearing in the Navier-Stokes, energy and Cahn-Hilliard equations. Generally, the fluid flow can be decomposed into acoustic modes, which propagate, and thermal/Cahn-Hilliard modes, which simply decay exponentially. The extension of the methodology to other types of fluids is straightforward.

The fourth and fifth phenomena we have studied concern multicomponent flows governed by the Cahn-Hilliard equation. The typical multicomponent axisymmetric configuration that we considered is the stripe, centred on poloidal coordinate θ_c and having angular span $\Delta\theta$.

We showed that, for a general class of multiphase and multicomponent models, the requirement of minimisation of interface length while preserving the stripe area determines the equilibrium position of the stripe. For stripes having a total area less than a critical area ΔA_{crit} , the equilibrium position is on the inside of the torus ($\theta_c^{eq} = \pi$). As the stripe area is increased above ΔA_{crit} , two equilibrium positions become possible, highlighting a second-order phase transition in this class of systems. We also generalise the Laplace pressure law. Our analysis gives an exact expression for the difference between the pressure inside of the (minority phase) stripe and the pressure outside of the stripe (i.e. in the majority phase), for both subcritical ($\Delta A < \Delta A_{\text{crit}}$) and supercritical ($\Delta A > \Delta A_{\text{crit}}$) stripes.

We have also shown that the stripe configurations are not always stable, or even metastable, when axisymmetry is not strictly enforced. For example, the droplet configuration is energetically favoured at small domain areas, while the band configurations, which wrap around the torus along the θ direction, are favoured at large domain areas. Moreover, we highlighted that the stripe configurations become unstable to small perturbations when either one of their interfaces crosses the boundary from the region of negative Gaussian curvature ($\frac{\pi}{2} < \theta < \frac{3\pi}{2}$) towards the region of positive Gaussian curvature ($-\frac{\pi}{2} < \theta < \frac{\pi}{2}$).

Finally, we considered the dynamics of stripes in the presence of hydrodynamics, when the approach to equilibrium of the stripes is achieved through underdamped harmonic oscillations. Using analytical techniques, we find expressions for both the angular velocity and damping coefficient. This is in contrast to the case in the absence of hydrodynamics (detailed in Sec. SM:2.4 of the supplementary material), where the approach to equilibrium is an exponential relaxation.

We believe that the results presented here provide non-trivial problems for developing computational methods for flows on curved surfaces (including the torus), and for benchmarking their accuracy and performance. For instance, the first three flow phenomena in this paper can be used for convergence testing of numerical codes implementing hydrodynamics on curved surfaces. To this end, we present a recipe for performing such tests in Appendix A, where we perform a convergence analysis for the numerical scheme employed in this paper. The multicomponent flow phenomena also provide a good example for cases where the Navier-Stokes equation is coupled to other equations capturing more complex physics. For instance, this approach can be adapted to study complex flows on lipid membranes, or to investigate passive and active liquid crystal flows on curved surfaces. Here, the analytical results are limited to the torus geometry and primarily for axisymmetric flows. In the future, it would be interesting to apply and extend the methodology employed here to non-symmetric flow configurations, as well as to other manifolds.

Declaration of Interests: The authors report no conflict of interest.

Acknowledgements: HK acknowledges funding from EPSRC (EP/J017566/1 and EP/P007139/1). HK and VEA also thank the EU COST action MP1305 Flowing Matter (VEA and HK; Short Term Scientific Mission 38607). VEA expresses gratitude towards Professor L.-S. Luo (Old Dominion University, Norfolk, VA, USA) for useful discussions and hospitality during the partial completion of this work, as well as towards the Romanian-U.S. Fulbright Commission for generous support through The Fulbright Senior Postdoctoral Program for Visiting Scholars, Grant number 678/2018. SB acknowledges funding from EPSRC, grant number EP/R007438/1. VEA and SB thank Professor Victor Sofonea (Romanian Academy, Timișoara Branch) for encouragement, as well as for sharing with us the computational infrastructure available at the Timișoara Branch of the Romanian Academy. This research was supported by the Research Computing

clusters at Old Dominion University. The authors thank Professor A. J. Wagner (North Dakota State University, Fargo, ND, USA) for useful discussions. We thank an anonymous referee for suggesting the stability analysis for the stripe configurations.

Appendix A. Convergence test

This section of the Appendix illustrates a procedure for using the benchmark problems introduced in Sections 3, 4 and 5 for convergence tests of numerical codes designed for hydrodynamics on curved surfaces. The validation is done against the analytic solutions derived in the aforementioned sections, which are constructed using expansions of the mode functions $\{f_\ell, g_\ell\}$ (for longitudinal waves) and $\{F_\ell, G_\ell\}$ (for the shear waves) including terms up to order n ($3 \leq n \leq 8$) with respect to the torus radii ratio, $a = r/R$. For definiteness, we restrict our convergence study to the amplitudes of the first even harmonic, $U_{c;1}(t)$ and $V_{c;1}(t)$.

In the first part of this section, we present the validation of our numerical scheme with respect to the spatial resolution. We consider the three benchmark tests described in Sections 3.2, 4.2 and 5.2. Unless otherwise stated, the fluid parameters and initial state are identical to those described in these sections. The numerical values of the amplitudes $U_{c;1}(t)$ and $V_{c;1}(t)$ are obtained as follows. The total simulation time, t_{\max} , is divided into S intervals $\Delta t = t_{\max}/S$, numbered using $0 \leq s \leq S$. At each time $t_s = s\Delta t$, the numerical solution for the profile of $u^{\hat{\theta}}$ or $u^{\hat{\varphi}}$ (for the longitudinal or shear wave benchmarks) are projected onto the basis functions $f_1(\theta)$ and $F_1(\theta)$ using rectangle integration

$$U_{c;1}^{\text{num}}(t_s) = \frac{1}{N_\theta} \sum_{i=1}^{N_\theta} \frac{u_{\text{num}}^{\hat{\theta}}(t_s, \theta_i) f_1(\theta_i)}{1 + a \cos \theta_i}, \quad V_{c;1}^{\text{num}}(t_s) = \frac{1}{N_\theta} \sum_{i=1}^{N_\theta} \frac{u_{\text{num}}^{\hat{\varphi}}(t_s, \theta_i) F_1(\theta_i)}{(1 + a \cos \theta_i)^{-2}}, \quad (\text{A } 1)$$

where ‘num’ indicates that the amplitudes are determined numerically. The mode functions $f_1(\theta)$ and $F_1(\theta)$ are computed via the eighth-order expansions with respect to a given in Eqs. (SM:3.3a) and (SM:3.4a).

In the context of the propagation of longitudinal waves along the poloidal (θ) direction through a perfect fluid, figure 19(a) shows the relative error of the angular frequency $|\omega_{c;1}^{\text{num}}/\omega_{c;1}^{\text{an}} - 1|$, where $\omega_{c;1}^{\text{an}} = c_s \lambda_{c;1}/r$ is computed using the eighth-order expansion of $\lambda_{c;1}$ in Eq. (SM:3.3b), while the numerical value $\omega_{c;1}^{\text{num}}$ is obtained using a two-parameter fit of the numerical amplitudes $U_{c;1}^{\text{num}}(t_s)$ to the analytic prediction in Eq. (3.25), i.e.:

$$U_{c;1}(t) = \mathcal{A} \cos(\omega_{c;1}^{\text{num}} t), \quad (\text{A } 2)$$

where \mathcal{A} and $\omega_{c;1}^{\text{num}}$ are free parameters. The time interval and total simulation time are taken as $\Delta t = 0.05$ (corresponding to 100 simulation steps at $\delta t = 5 \times 10^{-4}$) and $t_{\max} = 18$, such that the total number of intervals is $S = 360$. For completeness, we present the results for the isothermal and thermal ideal fluid cases, as well as for the isothermal Cahn-Hilliard multicomponent fluid with background order parameter $\phi_0 = 0.8$. The values of the parameters are identical to those considered in Sec. 3.2. It can be seen that all curves are parallel to the slope -5 dashed line, indicating that our numerical scheme has fifth order accuracy.

We now consider the benchmark problem presented in Sec. 4.2 concerning the damping of shear waves. figure 19(b) shows the decrease in the relative error of the damping coefficient $\nu(\chi_{c;1}^{\text{num}})^2/r^2$ for the amplitude of the first mode, $V_{c;1}(t)$, as a function of the number of grid points. The numerical values for the damping coefficient are obtained by

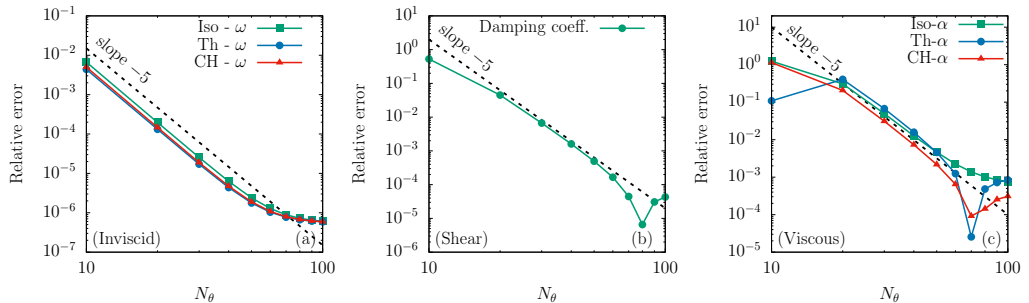


Figure 19. (a) The relative error of $\omega_{c;1}$ in the context of the inviscid propagation of longitudinal waves, for an isothermal ideal fluid (Iso), an ideal fluid with variable temperature (Th) and an isothermal Cahn-Hilliard multicomponent fluid (CH); (b) The relative error of the damping coefficient $\nu\chi_{c;1}^2/r^2$ in the context of shear waves damping; (c) The relative error of $\alpha_{c;1;a}$ in the context of the viscous damping of longitudinal waves, for the same 3 fluid described in (a). Each panel contains a dashed line indicating fifth order convergence.

fitting the numerical data using the analytic formula obtained by combining Eqs. (4.13) and (4.10), i.e.:

$$V_{c;1}(t) = \mathcal{A}e^{-\alpha t}, \quad (\text{A } 3)$$

where \mathcal{A} and α are free parameters. The time interval and total simulation time are taken as $\Delta t = 5$ (corresponding to 1000 simulation steps at $\delta t = 5 \times 10^{-3}$) and $t_{\max} = 1800$, such that the total number of intervals is $S = 360$. The analytic prediction for α is $\nu\chi_{c;1}^2/r^2$. In the log-log plot of figure 19(b), the relative error of the damping coefficient follows the slope -5 dashed line, also indicating the scheme is fifth-order accurate. The simulation parameters are identical to those considered in Sec. 4.2.

Finally, we consider the sound waves damping benchmark problem introduced in Sec. 5.2. figure 19(c) presents the relative error for the acoustic damping coefficient $|1 - \alpha_{c;1;a}^{\text{num}}/\alpha_{c;1;a}^{\text{an}}|$, where $\alpha_{c;1;a}^{\text{an}}$ is listed in Sec. 5.2 for the various fluid types considered. Considering the three types of fluids discussed in the first paragraph, these relative errors are plotted with respect to N_θ . The values $\alpha_{c;1;a}^{\text{num}}$ are obtained by fitting the numerical data using the analytic formula, given in Eqs. (5.34):

$$U_{c;1}(t) = \mathcal{A}e^{-\alpha_{c;1;a}^{\text{num}}t} \sin(\omega_{c;1}^{\text{num}}t), \quad (\text{A } 4)$$

where \mathcal{A} , $\alpha_{c;1;a}^{\text{num}}$ and $\omega_{c;1}^{\text{num}}$ are free parameters. The parameters used in this benchmark test are identical to those in Sec. 5.2 and for definiteness, we focus only on the case when the volumetric kinematic viscosity $\nu_v = 0.02$ (the other transport coefficients change from one type of fluid to the other, as described in Sec. 5.2). The time interval and total simulation time are taken as $\Delta t = 0.05$ (corresponding to 100 simulation steps at $\delta t = 5 \times 10^{-4}$) and $t_{\max} = 48$, such that the total number of intervals is $S = 960$. It can be seen that the relative error $|1 - \alpha_{c;1;a}^{\text{num}}/\alpha_{c;1;a}^{\text{an}}|$ in the acoustic damping coefficient generally follows the slope -5 dashed line.

In the second part of this section, we consider the effect of varying the expansion order n of the eigenfunctions, eigenfrequencies and all derived quantities. This study is performed at the level of the L_2 norms of the errors $[U_{c;1}^{\text{an}}(t) - U_{c;1}^{\text{num}}(t)]/U_0$ and $1 - V_{c;1}^{\text{num}}(t)/V_{c;1}^{\text{an}}(t)$ between the numerical values and analytic predictions for the amplitudes of the first even mode. These norms are computed by integrating over the simulation time using the

trapezoidal rule

$$\begin{aligned}
 L_2^{\text{long}} &= \left\{ \frac{1}{S} \sum_{s=0}^S \mathfrak{f}_s \left[\frac{U_{c;1}^{\text{num}}(t_s) - U_{c;1}^{\text{an}}(t_s)}{U_0} \right]^2 \right\}^{1/2}, \\
 L_2^{\text{shear}} &= \left\{ \frac{1}{S} \sum_{s=0}^S \mathfrak{f}_s \left[\frac{V_{c;1}^{\text{num}}(t_s)}{V_{c;1}^{\text{an}}(t_s)} - 1 \right]^2 \right\}^{1/2}, \tag{A 5}
 \end{aligned}$$

where $\mathfrak{f}_s = 1/2$ when $s = 0$ or $s = S$ and 1 otherwise. The reason why L_2^{long} is computed using absolute $[U_{c;1}^{\text{num}}(t_s) - U_{c;1}^{\text{an}}(t_s)]$ rather than relative $[U_{c;1}^{\text{num}}(t_s)/U_{c;1}^{\text{an}}(t_s) - 1]$ differences is that due to the oscillatory nature of $U_{c;1}^{\text{an}}(t_s)$, there are in principle values of t_s where $U_{c;1}^{\text{an}}(t_s)$ is arbitrarily close to 0. For such values of t_s , the relative error could be disproportionately large, producing meaningless results. Instead, the relative difference is preferred for $V_{c;1}(t_s)$ since $V_{c;1}^{\text{an}}(t_s)$ exhibits an exponential decay with respect to t_s . Thus, the absolute differences $V_{c;1}^{\text{num}}(t_s) - V_{c;1}^{\text{an}}(t_s)$ would contribute with an exponentially decreasing amplitude at large times and the result of an L_2 norm based on the absolute differences would therefore be biased towards the early time properties of $V_{c;1}(t)$. The analytical predictions $U_{c;1}^{\text{an}}(t)$ and $V_{c;1}^{\text{an}}(t)$ can be obtained from Eqs. (3.25) and (4.10). The numerical amplitudes $U_{c;1}^{\text{num}}(t_s)$ and $V_{c;1}^{\text{num}}(t_s)$ are obtained by projecting $u_{\text{num}}^{\hat{\theta}}(t_s, \theta)$ and $u_{\text{num}}^{\hat{\phi}}(t_s, \theta)$ onto the basis functions $f_1(\theta)$ and $F_1(\theta)$, as described in Eq. (A 1). Both the basis functions and the analytic solutions are obtained using the expansions in Eqs. (SM:3.3a) and (SM:3.4a), truncated at power n of the radii ratio a .

We begin with the benchmark problem introduced in Sec. 3.2, concerning the propagation of longitudinal waves through a perfect fluid. figure 20(a) shows the variation of L_2^{long} with respect to the truncation order of the expansion, which is varied between $3 \leq n \leq 8$, for the isothermal and thermal ideal fluid cases, as well as for the isothermal Cahn-Hilliard multicomponent fluid. The simulation parameters are identical to those presented in Sec. 3.2, as well as earlier in this section. In general, an exponential decay of L_2^{long} with respect to n can be observed for all fluid types considered. A sharper decrease in the L_2 error norm can be observed when n is increased from an odd value to an even one.

In the context of the shear wave damping benchmark introduced in Sec. 4.2, the analytical expression $V_{c;1}^{\text{an}}(t)$ is obtained by combining Eqs. (4.13) and (4.10). As before, $V_{c;1}^{\text{num}}(t)$ is obtained by projecting the velocity profile onto the basis functions F_1 , given in Eq. (SM:3.4a), truncated at order n . The same order n is used to evaluate the analytic prediction $V_{c;1}^{\text{an}}(t)$. The results are presented in figure 20(b), up to order $n = 8$. The L_2^{shear} decays exponentially and again sharper drops are seen when the expansion order is increased from an odd to an even value. The simulation parameters are identical to those employed in Sec. 4.2. A total of $S = 360$ time intervals of length $\Delta t = 1000\delta t = 5$ were saved ($t_{\text{max}} = 1800$).

Lastly, we investigate the convergence of the first harmonic in the context of viscous damping of longitudinal waves. The L_2^{visc} norm is computed using Eq. (A 5), where the analytical prediction for $U_{c;1}^{\text{an}}(t)$ is given in Eqs. (5.34). This prediction is evaluated using the values for ω_1^{an} and the integral $I_{c;0;1}$ truncated at n th order. The velocity profile is projected using Eq. (A 1) onto the basis function f_1 , computed using a truncation of Eq. (SM:3.3a) at the same order n , obtaining $U_{c;1}^{\text{num}}$. The results for the isothermal and thermal ideal fluid cases, as well as for the isothermal Cahn-Hilliard multicomponent fluid are summarised in figure 20(c). Since the linearised theory introduces errors of order

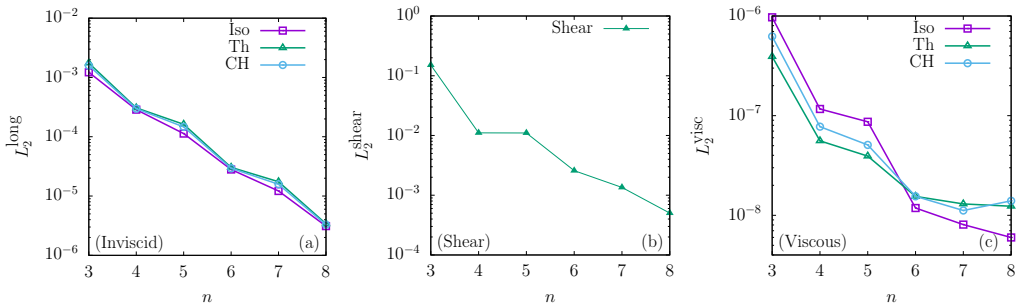


Figure 20. The L_2 norm computed using Eq. (A 5) in the context of (a) propagation of inviscid longitudinal waves; (b) damping of shear wave and (c) damping of longitudinal waves. In (a) and (c), we consider the cases of the isothermal ideal fluid (Iso), ideal fluid with variable temperature (Th) and isothermal Cahn-Hilliard multicomponent fluid (CH). In (b), only the isothermal fluid is considered.

$O(U_0, \varepsilon^2)$, in order to reveal the error induced by the expansion order, we decrease the kinematic viscosities employed in § 5.2 for each type of fluid by two orders of magnitude, namely $\nu_{\text{Iso}} = 10^{-4}$, $\nu_{\text{Th}} = 4 \times 10^{-5}$ and $\nu_{\text{CH}} = M \approx 6.486 \times 10^{-5}$, while the volumetric kinematic viscosity is set to $\nu_v = 2 \times 10^{-4}$ for all fluid types. The rest of the simulation parameters are: $N_\theta = 320$, $R = 2$ and $r = 0.8$ ($a = 0.4$), $U_0 = 10^{-5}$ and $\delta t = 5 \times 10^{-4}$. A total of $S = 500$ time intervals of length $\Delta t = 1$ were saved ($t_{\text{max}} = 500$). The exponential decay of the L_2^{visc} can be clearly seen, and again, a larger decrease can be seen when n is increased from an odd to an even value.

Appendix B. Eigenfunctions on the torus

This section of the Appendix presents a perturbative procedure for constructing solutions of Eqs. (3.10) and (4.4) in powers of $a = r/R$, where r and R are the inner and outer radii of the torus. Multiplying Eqs. (3.10) and (4.4) by $1 + a \cos \theta$ yields:

$$(1 + a \cos \theta) \left(\frac{\partial^2 \Psi_n}{\partial \theta^2} + \lambda_n^2 \Psi_n \right) + \alpha a \sin \theta \frac{\partial \Psi_n}{\partial \theta} = 0, \quad (\text{B } 1)$$

where $\alpha = 1$ and -3 for Eqs. (3.10) and (4.4), respectively. We seek solutions of the form

$$\begin{aligned} \Psi_n &= N_n (1 + a \cos \theta)^\alpha \psi_n, & \psi_n &= \psi_n^{(0)} + a \psi_n^{(1)} + a^2 \psi_n^{(2)} + \dots, \\ \lambda_n^2 &= \lambda_{n;0}^2 + a \lambda_{n;1}^2 + a^2 \lambda_{n;2}^2 + \dots, \end{aligned} \quad (\text{B } 2)$$

where the normalisation constant N_n ensures that Ψ_n retains unit norm. The prefactor $(1 + a \cos \theta)^\alpha$ ensures that all solutions Ψ_n with $n > 0$ are exactly orthogonal to the zeroth-order solution as long as they do not contain any free terms. Taking into account this prefactor, Eq. (B 1) becomes

$$(1 + a \cos \theta)^2 (\psi_n'' + \lambda_n^2 \psi_n) - \alpha a \sin \theta (1 + a \cos \theta) \psi_n' - \alpha a (a + \cos \theta) \psi_n = 0. \quad (\text{B } 3)$$

Demanding that the coefficient of each power of a vanishes, at zeroth order the harmonic equation is recovered

$$\psi_{n;0}'' + \lambda_{n;0}^2 \psi_{n;0} = 0. \quad (\text{B } 4)$$

Furthermore, demanding that the solution at each level of the perturbative analysis is periodic with respect to θ , the general solution of Eq. (B 4) can be written as

$$\psi_{n;0} = e^{in\theta}, \quad \lambda_{n;0}^2 = n^2. \quad (\text{B } 5)$$

where the real and imaginary parts correspond to the even and odd solutions, respectively.

Taking into account Eq. (B 4), the first-order contribution to Eq. (B 1) is

$$\psi''_{n;1} + n^2\psi_{n;1} + \lambda_{n;1}^2 e^{in\theta} - \frac{\alpha}{2} \left[(n+1)e^{i(n+1)\theta} - (n-1)e^{i(n-1)\theta} \right] = 0. \quad (\text{B } 6)$$

Since the solution of the homogeneous version of the above equation is proportional to $\psi_{n;0}$, it can be seen that $\lambda_{n;1}^2 = 0$, while $\psi_{n;1}$ can be found as

$$\psi_{n;1} = -\frac{\alpha}{2} \left[\frac{n+1}{2n+1} e^{i(n+1)\theta} + \frac{n-1}{2n-1} e^{i(n-1)\theta} \right]. \quad (\text{B } 7)$$

At second order, the following equation is obtained:

$$\begin{aligned} \psi''_{n;2} + n^2\psi_{n;2} + \left[\lambda_{n;2}^2 - \frac{\alpha^2 n^2}{2(4n^2-1)} \right] e^{in\theta} + \frac{\alpha(n+2)}{4} \left[1 + \frac{\alpha(n+1)}{2n+1} \right] e^{i(n+2)\theta} \\ - \frac{\alpha(n-2)}{4} \left[1 + \frac{\alpha(n-1)}{2n-1} \right] e^{i(n-2)\theta} = 0. \end{aligned} \quad (\text{B } 8)$$

As before, the coefficient of $e^{in\theta}$ must vanish. At this point, we note that in the case when $n = 1$, $e^{i(n-2)\theta} = e^{-i\theta}$ and is thus not independent of $\psi_{1;0} = e^{i\theta}$. Moreover, there is no value for $\lambda_{1;2}^2$ which ensures that the coefficients of $\cos \theta$ and $\sin \theta$ vanish simultaneously. Thus, at $n = 1$, the solution is

$$\psi_{1;2} = \frac{\alpha(3+2\alpha)}{32} e^{3i\theta}, \quad \lambda_{1;c/s;2}^2 = \frac{\alpha^2}{6} \mp \frac{\alpha}{4}, \quad (\text{B } 9)$$

where the upper and lower signs refer to the even and odd solutions, respectively. For $n > 1$, the solution is

$$\begin{aligned} \psi_{n;2} = \frac{\alpha}{16} \left[(n-2) \left(\frac{1}{n-1} + \frac{\alpha}{2n-1} \right) e^{i(n-2)\theta} + (n+2) \left(\frac{1}{n+1} + \frac{\alpha}{2n+1} \right) e^{i(n+2)\theta} \right], \\ \lambda_{n;2}^2 = \frac{\alpha^2 n^2}{2(4n^2-1)}. \end{aligned} \quad (\text{B } 10)$$

Keeping into account that at order $O(a^{n+1})$, the corrections to the eigenvectors of orders up to n must be computed as outlined above for $n = 1$, the above procedure can be continued to higher orders. Explicit expressions for the mode functions for $\alpha = 1$ (f_n and g_n) and for $\alpha = -3$ (F_n and G_n) are given in Sections SM:3.1.1 and SM:3.1.2 of the supplementary material (Busuioc *et al.* 2020b).

REFERENCES

- AL-IZZI, S. C., SENS, P. & TURNER, M. S. 2018 Shear-driven instabilities of membrane tubes and dynamin-induced scission. *arXiv* p. 1810.05862.
- AMBRUŞ, V. E., BUSUIOC, S., WAGNER, A. J., PAILLUSSON, F. & KUSUMAATMAJA, H. 2019 Multicomponent flow on curved surfaces: A vielbein lattice Boltzmann approach. *Phys. Rev. E* **100**, 063306.
- ARROYO, M. & DESIMONE, A. 2009 Relaxation dynamics of fluid membranes. *Phys. Rev. E* **79**, 039906.
- BERTALMIÓ, M., CHENG, L.-T., OSHER, S. & SAPIRO, G. 2001 Variational problems and partial differential equations on implicit surfaces. *J. Comput. Phys.* **174** (2), 759–780.
- BOOZER, A. H. 2005 Physics of magnetically confined plasmas. *Rev. Mod. Phys.* **76**, 1071–1141.
- BRIANT, A. J. & YEOMANS, J. M. 2004 Lattice Boltzmann simulations of contact line motion. II. Binary fluids. *Phys. Rev. E* **69**, 031603.

- BUSUIOC, S. & AMBRUŞ, V. E. 2019 Lattice Boltzmann models based on the vielbein formalism for the simulation of flows in curvilinear geometries. *Phys. Rev. E* **99**, 033304.
- BUSUIOC, S., AMBRUŞ, V. E., BICIUŞCĂ, T. & SOFONEA, V. 2020a Two-dimensional off-lattice Boltzmann model for van der Waals fluids with variable temperature. *Comput. Math. Appl.* **79**, 111–140.
- BUSUIOC, S., KUSUMAATMAJA, H. & AMBRUŞ, V. E. 2020b Supplementary material. URL to be made available by the publisher.
- COX, S., WEAIRE, D. & GLAZIER, J. A. 2004 The rheology of two-dimensional foams. *Rheologica Acta* **43**, 442–448.
- DZIUK, G. & ELLIOTT, C. M. 2007 Surface finite elements for parabolic equations. *J. Comput. Math.* **25**, 385–407.
- DZIUK, G. & ELLIOTT, C. M. 2013 Finite element methods for surface PDEs. *Acta Numerica* **22**, 289–396.
- FONDA, P., RINALDIN, M., KRAFT, D. J. & GIOMI, L. 2018 Interface geometry of binary mixtures on curved substrates. *Phys. Rev. E* **98**, 032801.
- GIORDANELLI, I., MENDOZA, M. & HERRMANN, H. J. 2018 Modelling electron-phonon interactions in graphene with curved space hydrodynamics. *Sci. Rep.* **8**, 12545.
- GROSS, B. J. & ATZBERGER, P. J. 2018 Hydrodynamic flows on curved surfaces: Spectral numerical methods for radial manifold shapes. *J. Comput. Phys.* **371**, 663–689.
- HENKES, S., MARCHETTI, M. C. & SKNEPNEK, R. 2018 Dynamical patterns in nematic active matter on a sphere. *Phys. Rev. E* **97**, 042605.
- HENLE, M. L. & LEVINE, A. J. 2010 Hydrodynamics in curved membranes: the effect of geometry on particulate mobility. *Phys. Rev. E* **81**, 011905.
- JANSSEN, L. M. C., KAISER, A. & LÖWEN, H. 2017 Aging and rejuvenation of active matter under topological constraints. *Sci. Rep.* **7**, 5667.
- KEBER, F. C., LOISEAU, E., SANCHEZ, T., DECAMP, S. J., GIOMI, L., BOWICK, M. J., MARCHETTI, M. C., DOGIC, Z. & BAUSCH, A. R. 2014 Topology and dynamics of active nematic vesicles. *Science* **345**, 1135–1138.
- KOBA, H. 2018 On derivation of compressible fluid systems on an evolving surface. *Quart. Appl. Math.* **76**, 303–359.
- KOBA, H., LIU, C. & GIGA, Y. 2017 Energetic variational approaches for incompressible fluid systems on an evolving surface. *Quart. Appl. Math.* **75**, 359–389.
- KRÜGER, T., KUSUMAATMAJA, H., KUZMIN, A., SHARDT, O., SILVA, G. & VIGGEN, E. M. 2017 *Lattice Boltzmann Method: Principles and Practice*. Springer.
- MACDONALD, C. & RUUTH, S. 2010 The implicit closest point method for the numerical solution of partial differential equations on surfaces. *SIAM Journal on Scientific Computing* **31** (6), 4330–4350.
- MARSDEN, J. E. & HUGHES, J. R. 1994 *Mathematical foundations of elasticity*. Dover publications.
- NITSCHKE, I., REUTHER, S. & VOIGT, A. 2017 Discrete exterior calculus (DEC) for the surface Navier-Stokes equation. In *Transport Processes at Fluidic Interfaces* (ed. D. Bothe & A. Reusken), pp. 125–263. Birkhäuser.
- NITSCHKE, I., REUTHER, S. & VOIGT, A. 2019 Hydrodynamic interactions in polar liquid crystals on evolving surfaces. *Phys. Rev. Fluids* **4**, 044002.
- NITSCHKE, I., VOIGT, A. & WENSCH, J. 2012 A finite element approach to incompressible two-phase flow on manifolds. *J. Fluid Mech.* **708**, 418–438.
- OLVER, F. W. J., LOZIER, D. W., BOISVERT, R. F. & CLARK, C. W. 2010 *NIST handbook of mathematical functions*. New York, NY: Cambridge University Press.
- PEARCE, D. J. G., ELLIS, PERRY W., FERNANDEZ-NIEVES, ALBERTO & GIOMI, L. 2019 Geometrical control of active turbulence in curved topographies. *Phys. Rev. Lett.* **122**, 168002.
- RÄTZ, A. & VOIGT, A. 2006 PDE's on surfaces—a diffuse interface approach. *Commun. Math. Sci.* **4**, 575 – 590.
- REMBIASZ, T., OBERGAULINGER, M., CERDÁ-DURÁN, PABLO, ALOY, M.-Á. & MÜLLER, E. 2017 On the measurements of numerical viscosity and resistivity in Eulerian MHD codes. *Astrophys. J. Suppl. S.* **230**, 18.

- REUTHER, S. & VOIGT, A. 2018 Solving the incompressible surface Navier-Stokes equation by surface finite elements. *Physics of Fluids* **30** (1), 012107.
- RIEUTORD, M. 2015 *Fluid Dynamics: An Introduction*. Springer.
- SASAKI, E., TAKEHIRO, S. & YAMADA, M. 2015 Bifurcation structure of two-dimensional viscous zonal flows on a rotating sphere. *Journal of Fluid Mechanics* **774**, 224–244.
- SERRIN, J. 1959 Mathematical principles of classical fluid mechanics. In *Encyclopedia of physics, Vol. VIII/1 (Fluid dynamics I)* (ed. S. Flügge & C. Truesdell), pp. 125–263. Springer-Verlag.
- SHAN, X. 2006 Analysis and reduction of the spurious current in a class of multiphase lattice Boltzmann models. *Phys. Rev. E* **73**, 047701.
- SOFONEA, V., BICIUȘCĂ, T., BUSUIOC, S., AMBRUȘ, V. E., GONNELLA, G. & LAMURA, A. 2018 Corner-transport-upwind lattice Boltzmann model for bubble cavitation. *Phys. Rev. E* **97**, 023309.
- SOFONEA, V., LAMURA, A., GONNELLA, G. & CRISTEA, A. 2004 Finite-difference lattice Boltzmann model with flux limiters for liquid-vapor systems. *Phys. Rev. E* **70**, 046702.
- SOFONEA, V. & SEKERKA, R. F. 2003 Viscosity of finite difference lattice Boltzmann models. *J. Comput. Phys.* **184**, 422–434.
- TAYLOR, M. E. 2011 *Partial Differential Equations III: Nonlinear Equations*, 2nd edn. Springer-Verlag.
- TORRES-SÁNCHEZ, A., MILLÁN, D. & ARROYO, M. 2019 Modelling fluid deformable surfaces with an emphasis on biological interfaces. *J. Fluid Mech.* **872**, 218–271.
- VOIGT, A. 2019 Fluid deformable surfaces. *J. Fluid Mech.* **878**, 1–4.